Propulsion Systems
Recent Advances, New Perspectives and Applications

Edited by Longbiao Li

Propulsion Systems - Recent Advances, New Perspectives and Applications

Edited by Longbiao Li

Contributors
Mark Pickrell, Andrew Youssef, Jie Pan, Andrew Guzzomi, David Matthews, Yang Ou, Yuqi Li, Yu Zhang, Jianjun Wu, Yuqiang Cheng, Bahram Nassersharif, Dale Thomas, Hosein Gorbani Dolama, Longbiao Li, Dmytro Tiniakov, Kunpeng Zhang, Bin Jiang, Fuyang Chen, Hui Yang

Notice

Statements and opinions expressed in the chapters are these of the individual contributors and not necessarily those of the editors or publisher. No responsibility is accepted for the accuracy of information contained in the published chapters. The publisher assumes no responsibility for any damage or injury to persons or property arising out of the use of any materials, instructions, methods or ideas contained in the book.

We are IntechOpen,
the world's leading publisher of
Open Access books
Built by scientists, for scientists

6,600+

Open access books available

178,000+

International authors and editors

195M+

Downloads

156

Countries delivered to

Our authors are among the

Top 1%

most cited scientists

12.2%

Contributors from top 500 universities

Interested in publishing with us?
Contact book.department@intechopen.com

Numbers displayed above are based on latest data collected.
For more information visit www.intechopen.com

Meet the editor

Dr. Longbiao Li is a lecturer in the College of Civil Aviation, Nanjing University of Aeronautics and Astronautics, China. Dr. Li's research focuses on the vibration, fatigue, damage, fracture, reliability, safety, and durability of aircraft and aero engines. He is the first author of 200 journal publications, 10 monographs, 4 edited books, 4 textbooks, 3 book chapters, 34 Chinese patents, 2 US patents, 2 Chinese software copyrights, and more than 30 refereed conference proceedings. He has been involved in different projects related to structural damage, reliability, and airworthiness design for aircraft and aero engines, supported by the Natural Science Foundation of China, COMAC Company, and AECC Commercial Aircraft Engine Company.

Contents

Preface

A propulsion system is an important subsystem that provides power for aerospace and marine vehicles as well as trains. The design of a propulsion system depends on the characteristics of the mission. New technologies have been applied to propulsion systems to improve efficiency and power and reduce energy consumption and pollution. This book focuses on technological advancements in propulsion systems in several areas. The field of aerospace research discusses impulse measurement methods for space micro-propulsion systems and matter/anti-matter propulsion. It also examines new measurement technology using polyvinylidene fluoride (PVDF) sensors for the vibration of components in propeller-shaft systems in marine propulsion. Furthermore, the book analyzes the reliability analysis for high-speed train traction systems and a new superstructure system for ballasted railways. Finally, the book discusses the application of nuclear propulsion in naval, aero, and space industries.

Longbiao Li
College of Civil Aviation,
Nanjing University of Aeronautics and Astronautics,
Nanjing, PR China

Section 1

Space Propulsion

Chapter 1

Review of the Aviation Power Units Development

Longbiao Li and Dmytro Tiniakov

Abstract

The development of the aviation industry depends on many factors. One of the most important factors is the development of power units. A power plant is a source of energy for an airplane. Without power units, flight is possible, but the transportation efficiency of such flights will be low. So, an in-depth analysis of the power unit structure is an actual task every time. The power unit is composed of several components. Obviously, the main structural element is the engine. However, the overall efficiency of the propulsion unit does not depend only on the engine. Subsystems and subcomponents of power units should have rational performance that can provide high overall efficiency. So, a detailed analysis of each of these structural members is also an actual task. To perform such an analysis, it is necessary to know the characteristics of these components and ways to increase their efficiency. In this chapter, all these features are briefly explained. In addition, some trends for the future development of civil aircraft power units are discussed.

Keywords: power unit, engine, aircraft structure, thrust, emission, noise

1. Introduction

The history of aviation is inextricably linked to the history of engine development. Throughout its existence, progress in aviation has been based primarily on progress in the development of aircraft engines. In turn, the ever-increasing demands for improving the efficiency of air transportation have been a powerful driver for the development of aircraft engines.

There have been many attempts to create a heavier-than-air, powered aircraft. One of the first aviation pioneers to create such an aircraft was the Russian researcher A.F. Mozhaisky [1]. Between 1881 and 1885, he created an airplane powered by a steam engine. The energy efficiency of the engine was not high, and this, along with other structural specifics, influenced the failure of this project. About 20 years later, American aviators, the Wright brothers, created the first successful airplane [1]. But this aircraft was already equipped with a piston engine. The piston engine provided sufficient energy efficiency for airplane flights at an early stage of aviation development.

In the 30s of the twentieth century, engine engineers developed engines with self-igniting fuel, also known as diesel engines. Thanks to it, an airplane achieved a speed

record of 756 km per hour [2]. But by that time, internal combustion engines had exhausted their energy efficiency reserves.

Problems with the power-to-weight ratio of aircraft required new approaches from engine designers. Since the beginning of the twentieth century, researchers had been developing the theory of gas turbine engines. Scientists from Russia, Great Britain, and Germany were active in this field and were awarded several patents on the principle of operation and design of such engines. The first aircraft to successfully fly with a turbojet engine was the He-178, developed in Germany in 1939. However, the first generation of turbojet engines provided high power but had a very high fuel consumption. This did not allow the use of these engines for commercial aviation. With the development of turboprop and bypass turbojet engines, it became possible to achieve sufficient energy efficiency.

The first aircraft with a turboprop engine was the British Trent-Meteor, which made its first flight in 1945 [3]. The first bypass turbojet engine was the Rolls-Royce Conway, developed in the late 40s of the twentieth century. It was installed on the first commercial airliners such as Boeing 707-420, Douglas DC-8-40, etc. [4]. From that moment on, gas turbine engines became the main engines for civil aviation.

Currently, commercial aviation has several developers of high-performance engines. However, as in the past, existing engines have reached their limits in the new operating conditions. Without the development of new approaches to propulsion, the new conditions proposed by ICAO in the field of environmental protection cannot be satisfied.

ICAO has stated that the amount of harmful emissions must be reduced by a factor of 2 by 2050 [5], and ICAO is also tightening the requirements for noise [6]. Stringent emission reduction requirements can be achieved in several ways. But the main direction that can ensure the reduction of emissions is, of course, the development of new engines with new operating principles. Such engines are: electric, hydrogen and, as an intermediate stage, hybrid. But a separate engine cannot provide the required own efficiency without related subsystems.

2. Definition of concept power unit

2.1 Purpose of aircraft power unit

The purpose of airplane power units is to generate thrust, supply energy to some onboard systems, and solve specific tasks. Power units are a set of engines and subsystems providing their operation on all possible modes of operation (Mach flight number M, altitude H, temperature T, etc.) for the aircraft.

2.2 Power units' subsystem content

As was said above, a power unit contains not only engines, which are the main object of it. However, depending on an aircraft type, some subsystems and auxiliary components can be present in it. Brief contents for more common cases are presented in **Figure 1**.

So, about the purposes of the power unit structural members and subsystems.

Engine is needed for thrust or power generation and supply some of auxiliary subsystem such as electrical, hydraulic, pneumatic, etc. Brief classification of the engine by type of thrust creation is presented in **Figure 2**.
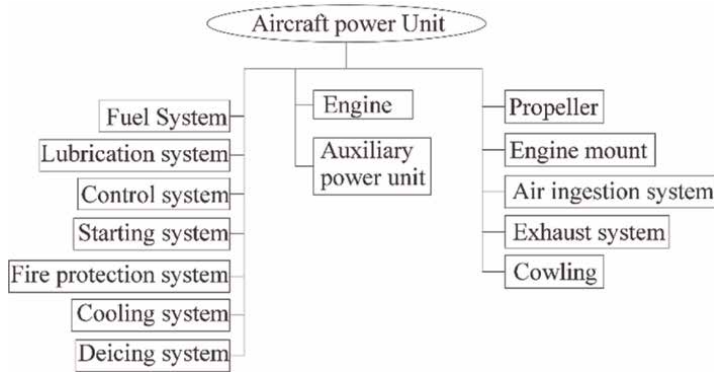
Figure 1.
Brief content of a typical power unit of an aircraft [7].
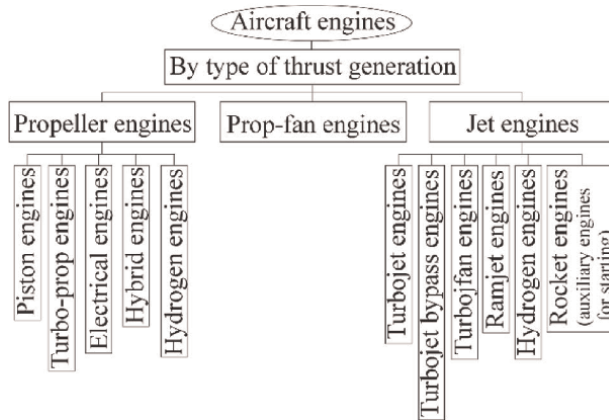
Figure 2.
Aviation engine classification by type of thrust creation [7].

A propeller creates thrust as it rotates by throwing air back with some additional velocity (on piston, turboprop, and prop-fan engines). It has a propeller spinner. An example of an aircraft propeller is shown in **Figure 3**.

The fuel system is a complex of interacting subsystems designed to supply the engine with fuel for all operating conditions permitted for that aircraft and may also perform a number of additional functions (e.g., oil cooling, maintaining a specified center of gravity position, etc.). A brief diagram of a typical fuel system is shown in **Figure 4**.

The lubrication system is a set of units designed to lubricate the engine, dissipate heat from the engine units, and remove solid particles formed between friction surfaces under all aircraft operating conditions (**Figure 5**).

The engine mount (**Figure 6**) is designed to attach an engine with its installed auxiliaries and other equipment to airframe attachments. This means that it must support all possible loads for all allowable operating conditions for that airplane.

The air ingestion system is designed to intake and deliver the required amount of air to the air consumer in all operating modes. Therefore, it is necessary to ensure the transformation of the kinetic energy of the flow into the potential energy of the pressure with minimum losses (**Figure 7**).
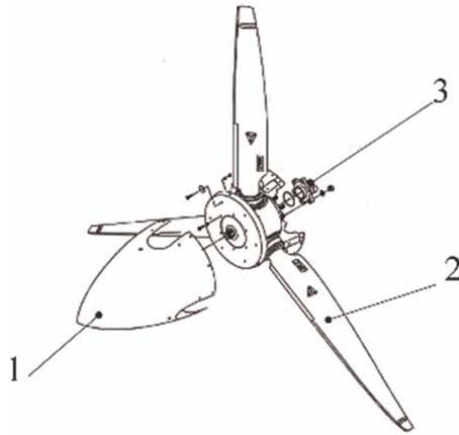
Figure 3.
Common an aircraft propeller structure [8]: 1—Spinner; 2—Multiposition blade; and 3—Engine fitting.
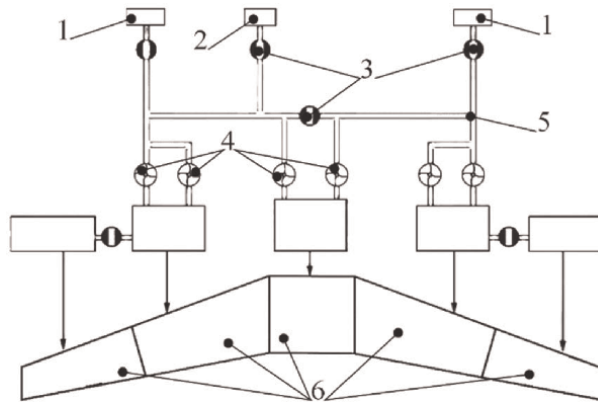
Figure 4.
Typical fuel system for modern transport category aircraft [9]: 1—Engines; 2—Auxiliary power unit; 3—Valves; 4—Pumps; 5—Pipelines; and 6—Fuel tanks.
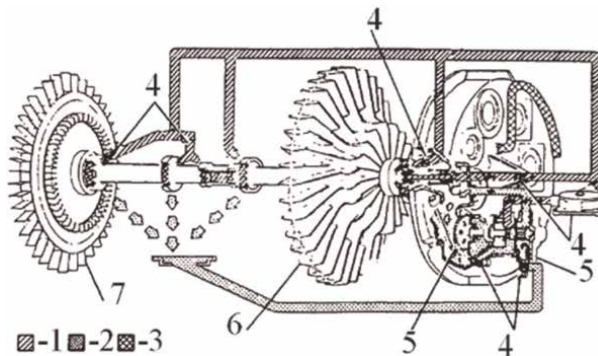
Figure 5.
Typical lubrication system for an engine [10]: 1—Pressure oil channel; 2—Scavenge oil channel; 3—Vent channel; 4—Filters; 5—Pumps; 6—Compressor; and 7—Turbine.
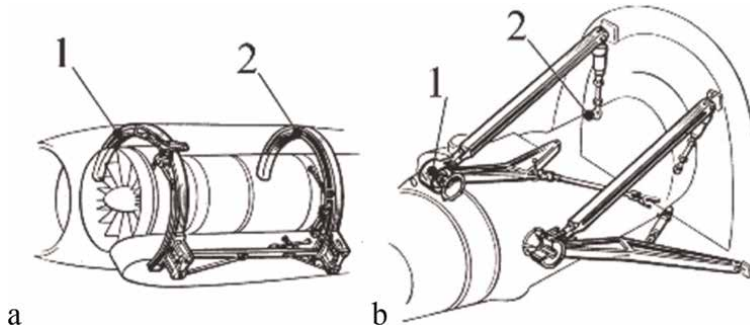
Figure 6.
Typical engine mounts for a turbojet bypass (a) and a turboprop engines (b) [7]: 1—Front attachment; and 2—Rear attachment.
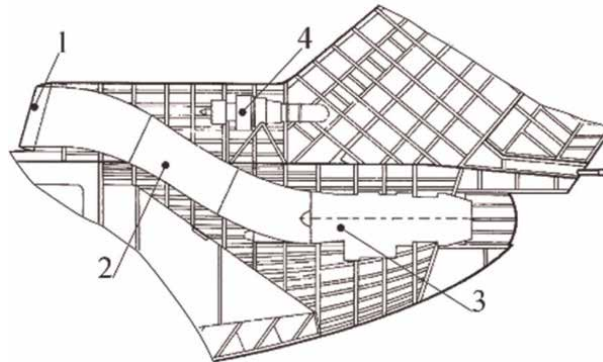
Figure 7.
Aft fuselage engine air ingestion system [11]: 1—Air-intake; 2—Duct channel; 3—Engine; and 4—APU.
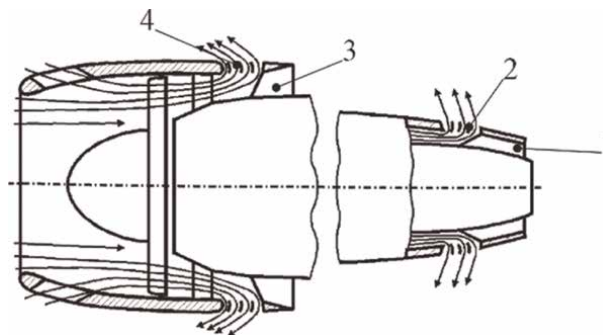
Figure 8.
Exhaust system for a typical turbojet bypass or turbofan engine with separate thrust reverse [7]: 1—Hot channel nozzle; 2—Hot channel thrust reverse; 3—Cold channel; and 4—Cold channel thrust reverse.

The exhaust units (**Figure 8**) of the engines are designed to convert the thermal and potential energy of the gases into kinetic energy of the outgoing flow. For modern airplanes of the heavy transport category, it is also necessary to provide thrust reversal for deceleration.
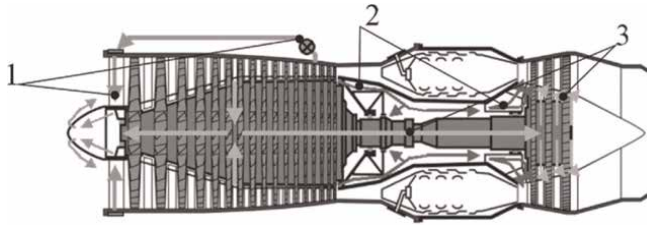
Figure 9.
Cooling and de-icing schemes for the typical turbojet bypass or turbofan engines [12]: 1—De-icing channels and components; 2—Cooling for the combustion chamber channel; and 3—Internal and turbine discs and blades cooling channels.
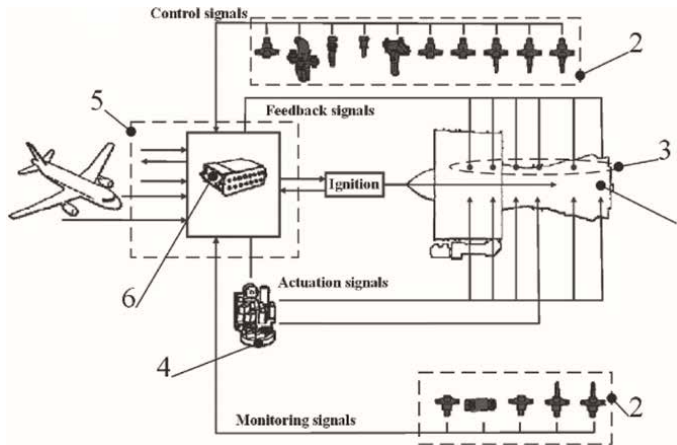
Figure 10.
Brief scheme for a typical engine control system [13]: 1—Engine; 2—Sensors; 3—Sensors location; 4—Hydromechanical components; 5—Electronic and electrical components; and 6—Full authority digital engine control.

The cooling system for engines and their subsystems is needed for the cooling of the whole engine directly or its some parts or subsystems (**Figure 9**).

Engine control (**Figure 10**) includes ground and in-flight engine start, false start, cold start, engine normal and emergency engine shutdown, engine operating mode control, and engine thrust revers control.

The starting system is used to transfer the aircraft engine from the non-operating condition to the low-gas steady state, which is characterized by the lowest turbine speed at which it can operate continuously for a long period of time.

The fire protection system (**Figure 11**) is designed to ensure flight safety by detecting and preventing the occurrence of fire in the power unit subsystems.

The de-icing system (**Figures 9** and **12**) is a set of units designed to: prevent ice build-up on engine structural elements or subsystems, remove ice build-up to provide all-weather conditions, and improve flight safety in icing conditions.

The nacelle or cowling (**Figure 13**) is designed to reduce drag, organize airflow for engine cooling, and reduce engine noise.

The Auxiliary Power Unit (APU) is designed to start the main engines under certain conditions and to supply power to systems not related to the generation of the main thrusts, such as electrical, hydraulic, pneumatic, etc. The APU is usually located in the aft section of the fuselage (**Figure 14**).
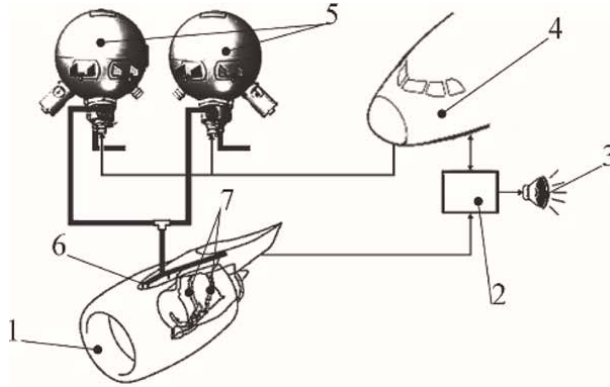
Figure 11.
Typical fire protection system for an engine [14]: 1—Engine; 2—Control unit; 3—Alarm signal; 4—Cockpit; 5—Antifire substance balloons; 6—Discharge nozzles; and 7—Engine fire loops.
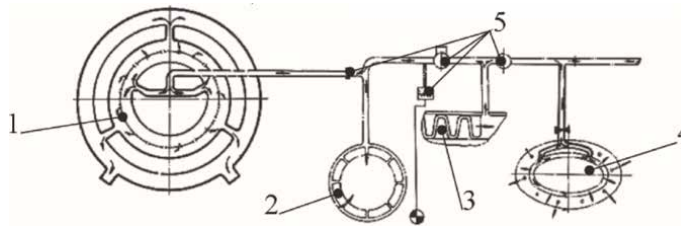
Figure 12.
Typical de-icing system for an engine [15]: 1—Air intake of the engine; 2—Inlet guide vane; 3—Compressor; 4—Air intake of the hit-exchanger of the lubrication subsystem; and 5—Components of the de-icing system (valves, gages, etc.)
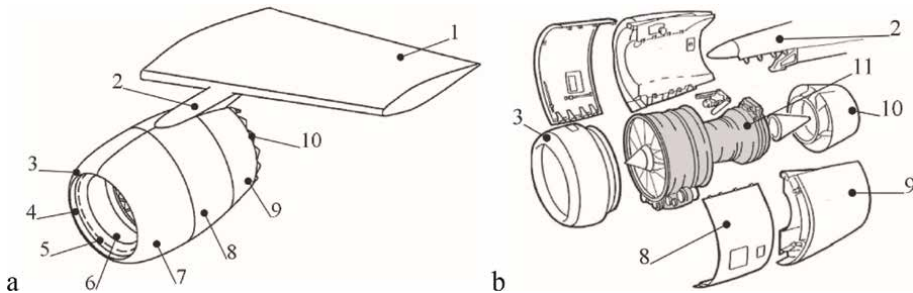
Figure 13.
Structure of a nacelle of a turbojet bypass or turbofan engine [7]. (a) Assembled; (b) disassembled: 1—Wing; 2—Pylon; 3—Air intake; 4—Lips of the air intake; 5—Inner surface of the air intake, 6—Duct channel; 7—External skin of the air intake; 8—Fan cowl; 9—Reverser cowl; 10—Nozzle assembly; and 11—Engine.

As shown above, the content of the power unit subsystem has a very wide range. Really, it is variable with which depends on an aircraft purpose and flight performance.

3. Analysis of the future trends for aviation power units improvement

Modern power units have a high level of performance, and for ordinary people, the question is why they need to be improved. There are several reasons that can answer
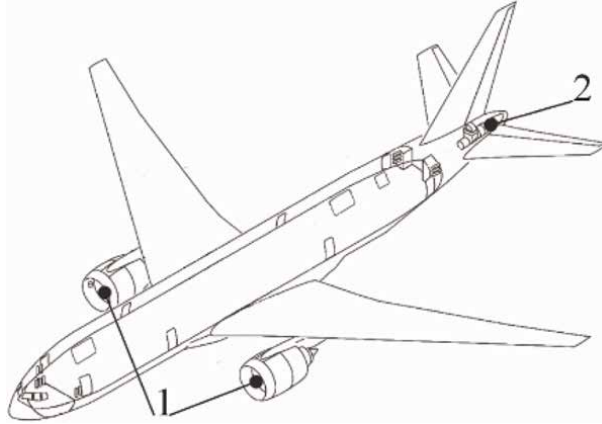
Figure 14.
APU location onboard of an aircraft [16]: 1—Main engines; and 2—APU.

this question. First of all, the aviation industry is the leader in engineering because it requires the highest possible performance, which can provide more higher efficiency of this transportation industry. The second reason is the environmental impact. In recent years, society demands a stronger approach to environmental safety. And the aviation industry has to make its own contribution. So, these two reasons push aviation engine engineers to improve the power units.

A number of ways are used to increase the range and altitude, speed, cargo capacity, also to improve the take-off and landing performance of aircraft and reduce the environmental impact.

3.1 Thrust and power improvement

Required thrust P, measured in [N] or [kg], and power N, measured in [W] or [h.p.] of the power unit.

Maximum airspeed is determined by the following equations:

- for (bypass) turbojets or turbofan engines

$$V_{\max} = \sqrt{\frac{2 \cdot P}{C_{Da} \cdot S \cdot \rho_H}}, \tag{1}$$

where C_{Da} is an aerodynamic drag coefficient; S is a wing area; ρ_H is the atmospheric density at a given altitude H;

- for piston and turboprop engines

$$V_{\max} = \sqrt{\frac{2 \cdot N \cdot \eta_p}{C_{Da} \cdot S \cdot \rho_H}}, \tag{2}$$

where η_p is propeller efficiency factor.

As an example of the efficiency of modern engines, it is possible to explain the maximum performance of different types of engines:

- The GE90-115B has a maximum thrust of 513,950 N (it showed a world record thrust of 569,000 N at the time of testing) for turbojet bypass or turbofan engines;

- The NK-12 has a maximum power of 11,000 kW (15,000 shp) for turboprop engines;

- The VD-4 K has a maximum power of 3200 kW (4300 shp) for piston engines;

- Cargo capacity, cruising altitude, runway length, ceiling and zoom altitude, and maneuverability are primarily determined by the available thrust of the aircraft's engines.

3.2 Specific weight of an engine

The specific weight of an engine indicates the weight efficiency of an engine, or in other words, how much engine weight is required to produce a given level of thrust or power. The equation for specific weight is

- for turbojet bypass or turbofan engines.

$$\gamma_{en} = m_{en} \, g/P, \tag{3}$$

where m_{en} is the engine weight; g is gravity acceleration;

- for piston and turboprop engines, [daN/kw] or [kg/h.p.]

$$\gamma_{en} = m_{en} \, g/N. \tag{4}$$

So, the minimum specific weight of the power unit is required.
Modern time, the lowest specific weight for different types of engines are

- for piston engines is γ_{en} = 0.67–1.3, [daN/kw];

- for turboprop engines is γ_{en} = 0.27–0.33, [daN/kw];

- for turbojets is γ_{en} = 0.2–0.25;

- for turbojets with afterburner is γ_{en} = 0.15–0.2;

- for bypass turbojets or turbofans is γ_{en} = 0.165–0.22;

- for bypass turbojets or turbofans with afterburner is γ_{en} = 0.1–0.15.

For an example, Prof. Mozhaisky airplane steam engines had γ_{en} = 10.7, Brothers Writes airplane with piston engine had γ_{en} = 8.4 and now, the most powerful turbojet in the world GE90-115B has γ_{en} = 0.167.

3.3 Specific weight of a power unit and fuel

The weight of a power unit is determined not only by the engines but also by all the subcomponents and subsystems, including the fuel. And here we can see the collision.

On one side as smaller weight then better, but on the other side as more higher weight of fuel than more longer range and duration of a flight. The required weight of fuel is determined not only by the required range and duration of a flight but also by fuel consumption, which will be discussed below.

The minimum specific weight of an engine and fuel is determined by the eqs. [7].

$$\overline{m}_{p.u} = \frac{m_{p.u}}{m_{t.o}} = n_{en}k_{p.u}\frac{m_{en}}{m_{t.o}} = n_{en}k_{p.u}\left(\frac{m_{en}g}{P_0}\right)\left(\frac{P_0}{m_{t.o}g}\right) = n_{en}k_{p.u}\gamma_{en}t_0, \tag{5}$$

$$\overline{m}_f = \frac{m_f}{m_{t.o}}, \tag{6}$$

where $m_{p.u}$ is the weight of a power unit; $m_{t.o}$ is the take-off weight of an aircraft; n_{en} is the number of engines; $k_{p.u}$ is an empirical factor for the additional weight of a power unit of subcomponents and subsystems for an engine, engines (approximately $k_{p.u} = 1.2$–2.2); t_0 is the specific weight to thrust ratio of an aircraft, $t_0 = P_0/m_{t.o}g$; m_f is weight of the fuel; $\overline{m}_f$ is the specific weight of the fuel.

Some values of $\overline{m}_{p.u}$ and $\overline{m}_f$ based on statistical data for different types of aircraft are presented in **Table 1**.

3.4 Specific fuel consumption

The specific fuel consumption indicates the efficiency of the engine because it shows how much fuel the engine needs under given flight conditions to produce 1 N of thrust (or 1 W of power) in 1 hour.

Minimal specific fuel consumption can be achieved in several ways: good aerodynamics of an airframe, rational choice of flight parameters (altitude, speed, etc.), rational operation of subsystems of a power unit, and, of course, it depends on the engine performance. **Table 2** shows some examples of the fuel consumption for the most powerful engines.

Specific cruise fuel consumption is the primary determinant of an aircraft's economics and has a significant impact on the amount of emission emitted into the atmosphere.

Type of aircraft	$\overline{m}_{p.u}$	$\overline{m}_f$
Subsonic passenger and transport	0.08–0.14	0.18–0.40
Maneuverable	0.18–0.22	0.25–0.30

Table 1.
Examples of $\overline{m}_{p.u}$ and $\overline{m}_f$ based on statistical data.

Engine	C_p [kg/N·hour]	C_p [kg/kw·hour]
GE90-115B	0.033	—
NK-12	—	0.224
VD-4K	—	0.251
D-36	0.0662	—

Table 2.
Examples of the fuel consumption for the most powerful engines.

3.5 Aerodynamic drag

The engine has very bad shape from the point of view of aerodynamics. This problem is usually solved by using nacelles. But subsystems of an engine have several external components such as air intakes of a ventilation system, access doors for maintenance operations, etc. All these structural features must be optimized by the next approaches:

- Reducing the aerodynamic drag generated by the engine and minimizing shock pressure losses by optimizing the design of engine air intakes, radiators, cooling systems;

- Propeller shape and control optimization;

- Nozzle shape and control optimization (the latter is for supersonic and thrust vectoring aircraft);

- Optimization of thrust rever device performance.

3.6 Environmental impact

The environmental impact of aviation has two parts: (1) emissions; (2) noise. Both are shown in the ICAO environmental impact forecast (**Figure 15**).

3.6.1 Emissions

First of all, the approaches to reduce emissions will be explained.

As it has been said above, fuel consumption has an important place in the reduction of environmental impact. It is especially actual for the engines with traditional oil-based fuel. So, how it is possible to improve the environmental performance of the traditional for the modern time engines. There are several approaches:

- Increase the bypass ratio. This ratio for the modern aircraft can reach 12.5 (for example, Pratt & Whitney PW1000G [17]). But, for the improvement of the
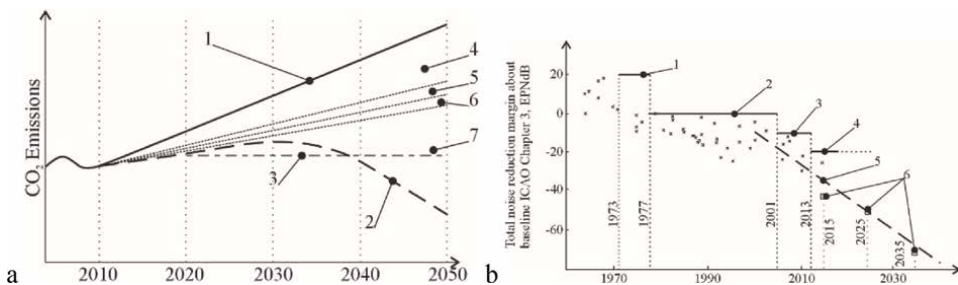
Figure 15.
Forecast environmental requirements: (a) Emission CO_2 [5]: 1—Emission growing without any actions; 2—Emission reducing forecast; 3—Baseline for CO_2 level for 2020; 4—Technology approaches; 5—Operational approaches; 6—Infrastructures approaches; and 7—New fuels types (b) Noise level [6]: 1—ICAO Chapter 2 (1973); 2—ICAO Chapter 3 (1977); 3—ICAO Chapter 4 (2001); 4—ICAO Chapter 14 (2013); 5—Noise reducing forecast; 6—Different international programs

environmental impact, it is reasonable to increase it up to 20 (for example, NK-93 experimental engine had 16.6 [18]);

• Increase the pressure ratio of the engine. This factor for modern aircraft has level about 40 (for example, GE90-115 has 42 [19]). Future trend for this ratio is level about 60 (for example, GE9X experimental engine has 60 [20]);

• Increase the temperature in ahead of the turbine. The gas temperature indicates the thermal load on the turbine. Now the operating temperature before the turbine is about 1400°C [2]. But there is an example with the temperature about 1560°C (PD14 [21]);

• Reduction of aerodynamic drag by improving the geometric parameters of the airframe. In this way, the reduction in fuel consumption can reach 7% [21–24].

The first three approaches can provide fuel consumption (emission level correspondingly) decreasing about 15%.

But, as it seems, that all these approaches cannot provide decreasing in emission of 50% as it is required by ICAO. And nowadays there are new solutions, which can provide the required level of emission for the aviation industry. They are new types of fuel or engines.

First of all, about new types of fuel. In 1988, the USSR started test flights of the TU-155 (**Figure 16**), it was the first aircraft of the transport category with hydrogen fuel [25]. It had an experimental NK-88 engine.

Liquid hydrogen, with its high specific calorific value, which is three times higher than that of traditional oil-based fuels, and exceptional environmental purity, has shown great promise as a fuel for various engines.

Another possibility is the application of electric or hybrid power units. This process started with electric drones at the beginning of the twenty-first century. Nowadays, there are many projects for the general aviation aircraft (for example, **Figure 17**).

But until now, the application of electric power units for the transport category aircraft is still under development and research.

For the light aircraft, the main power source has been lithium-ion batteries. The use of batteries as the main source of energy limited the capabilities of aircraft—
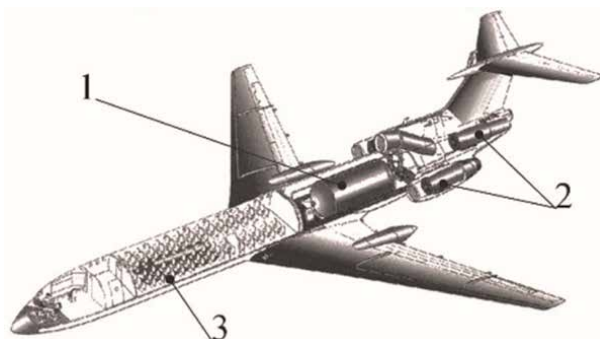
Figure 16.
Tu-155 is the first transport category aircraft with hydrogen fuel power unit [25]: 1—Hydrogen fuel tank; 2—Engines; and 3—Passenger compartment.

Figure 17.
NASA X-57 Maxwell modification IV is testing electrical aircraft [26].

range, flight duration, cargo capacity. Therefore, aviation engineers began to consider alternative options for obtaining energy. Some of them are as follows:

- Solar panels that convert radiation energy into electricity;

- Fuel cells, which convert the chemical energy of the fuel into electrical energy without combustion; hydrogen is most commonly used as the fuel.

A hybrid power unit converts energy twice: first into mechanical energy with the help of traditional engines, then into electrical energy with the help of generators. A hybrid power unit consists of an electric part (electric motor, generator, battery) and a traditional internal combustion engine using chemical fuel. And if today it is oil-based fuel, in the future it will be hydrogen, which opens great prospects for the development of aircraft based on the "all electric aircraft" approach.

An all-electric aircraft produces no emissions. However, it is not yet considered completely environmentally friendly because the production of batteries pollutes the environment and their structure and chemical composition make them difficult to dispose of.

3.6.2 Noise

Noise is also a dangerous factor that affects the environment. There are two sources of noise: airframe and engine. Improving the geometric parameters of an airframe can reduce the noise for cruise flight [27]. At the time of landing, the airframe has a landing configuration for its high-lift devices. Engine noise depends on engine operating modes (that also depends on flight mode). Most higher noise is presented for the maximum thrust mode, which is present for the take-off and maximum flight speed, and also for the thrust reverse mode, so in time of the landing (**Figure 18**).

The maximum flight speed mode is appropriate for the high flight altitude, and the noise in this case is dangerous only for the persons onboard: crew members and passengers. The noise can be reduced by the correct choice of fuselage skin panels and engine nacelle panels. These two structural solutions are usually sufficient (see **Figure 19**).
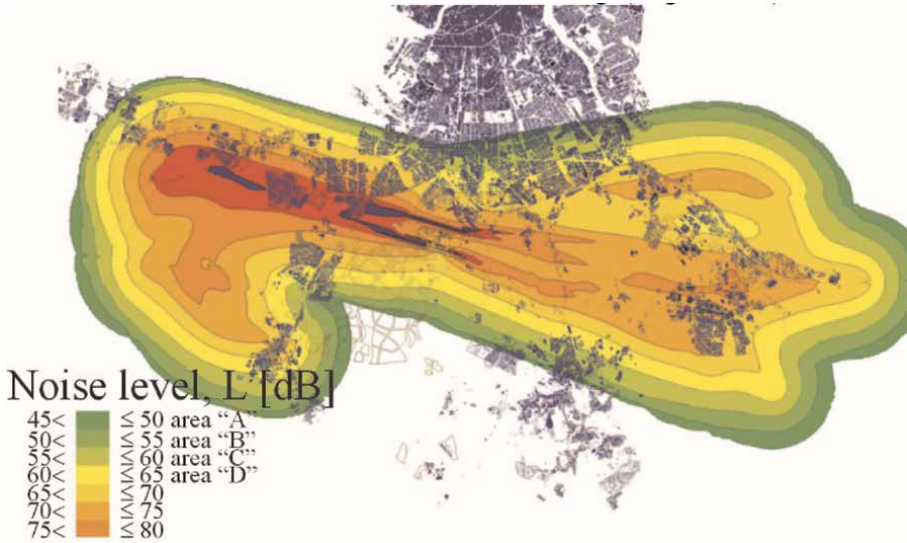
Figure 18.
Typical airport noise map [28].
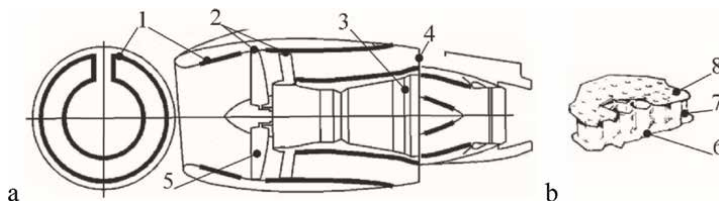
Figure 19.
Typical noise absorption methods [7, 29] (from fan, compressor, combustion) for bypass turbojet or turbofan engines: (a) structural solutions maps for an engine; (b) typical soundproof honeycomb panel; 1—Acoustical covering of power unit elements (thick lines); 2—Optimum clearances; 3—Optimal number and configuration of blades; 4—Optimal nozzle location to reduce exhaust velocity; 5—Fan without inlet guide vanes; 6—Backing skin; 7—Honeycomb with soundproofing features; and 8—Perforate lining.

However, for the near-ground flight modes (takeoff, climb, approach, landing, thrust reverse), such approaches are not sufficient. The main sources of engine noise are: propeller (for turboprop and piston engines), fan, combustion, turbine and nozzle (for turbojet engines). Noise from internal structures can also be absorbed by nacelle panels [7, 29]. However, propeller and jet noise are difficult to reduce.
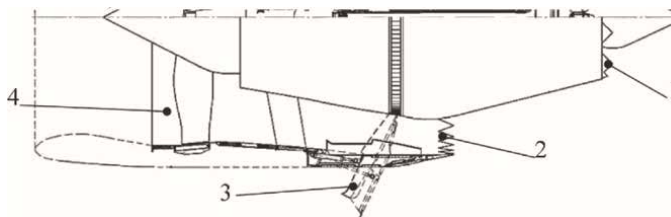
Figure 20.
Typical noise absorption methods [30] (from the jet and thrust reverse) for bypass turbojet or turbofan engines: 1 and 2—Special shapes for nozzles of hot and cold channels; 3—Thrust reverse only for the cold channel; and 4—Cold channel.

The blades of a propeller can be optimized by shape, twist angle, control device, etc. (**Figure 3**). The specific shape was developed for the exhaust nozzles to reduce the noise level (see **Figure 20**).

Thus, all of the above structural approaches can provide noise reduction for all modern high-efficiency engine types.

4. Summary and conclusions

Future development of power units requires an in-depth analysis of existing design, manufacturing, and logistics solutions. Their optimization can provide increasing in power unit efficiency. However, new ideas can provide more best performance, but they require a lot of time for research, testing, and analysis of results. New approaches (e.g. hydrogen power units) create significant impact on the traditional (for aviation engineering) design process.

Explained above detailed separation of the power unit structure by subsystems and subcomponents can provide more best understanding areas where it is necessary to apply extra efforts for the power unit efficiency increase, and can help to understand dependencies between different structural members of a power unit.

Author details

Longbiao Li* and Dmytro Tiniakov
College of Civil Aviation, Nanjing University of Aeronautics and Astronautics, Nanjing, PR China

*Address all correspondence to: llb451@nuaa.edu.cn

IntechOpen

References

[1] Anderson JD. The Airplane, a History of Its Technology. American Institute of Aeronautics and Astronautics; 2002. p. 369

[2] Walsh PP, Fletcher P. Gas Turbine Performance. 2nd ed. Oxford: Blackwell Science; 2004. p. 646

[3] Glenn A. Meteor in Action. Carrollton, Texas: Squadron/Signal Publications Inc.; 1995

[4] Pearson H. Rolls-Royce and the Rateau Patents. Derby: Rolls-Royce Heritage Trust; 1989

[5] ICAO. CORSIA Methodology for Calculating Actual Life Cycle Emissions Values. Montréal, Québec, Canada: International Civil Aviation Organization (ICAO); 2022. p. 39

[6] Sparrow V, Gjestland T, et al. Aviation noise impacts white paper. In: Chapter 2 Aircraft Noise. Montréal, Québec, Canada: International Civil Aviation Organization (ICAO); 2019. p. 61

[7] Tiniakov D, Li L, Su Y. Airworthiness Design of Civil Aircraft Systems and Structures. Beijing: Beijing press; 2018. p. 363

[8] Diamond. ATA-61—Propeller. Diamond Maintenance training division; 2011

[9] Airbus. 28 Fuel system. In: A320 Technical Training Manual. Airbus Industrie; 2000. p. 304

[10] Otis CE, Vosbury PA. Aircraft Gas Turbine Powerplants. Florida: Aircraft Technical Book Company; 2010

[11] Udalov KG, Sham OV. Aircraft Yak-40. Moscow: Transport; 1992. p. 72

[12] Rolls Royce. Aircraft Engine 522 to 524 Preliminary Maintenance Manual—TSD 1007. London, UK: Rolls Royce AVON; 1953. p. 120

[13] EASA PART66 Online Training. 1999. Available from: https://www.part66online.com/qa/329 [Accessed: May 28, 2023]

[14] Aviation Investigation Report A14Q0068. Gatineau, Québec, Canada: Transportation Safety Board of Canada; 2016. p. 53

[15] Antonov. Vol. 3 Powerplant of the An-22. In: Specification of the An-22. Kiev: Antonov; 1970. p. 160

[16] Boeing. Airplane Rescue and Fire Fighting Information B-777. Seattle, Washington, USA: Boeing; 2019. p. 8

[17] Pratt & Whitney. Pratt & Whitney Unveils Higher Thrust Pure Power Engine (Press release). Pratt & Whitney. 2014. Available from: https://web.archive.org/web/20190114132322/http://www.pw.utc.com/Press/Story/20140520-0902 [Accessed January 14, 2019]

[18] Kuznetsov. Fan-propeller engine NK-93. In: Domestic Aviation and Space Techniques. Samara: SNTK; 2005. p. 2

[19] FAA. Type Certificate Number E00049EN. U.S. Department of transportation; 2016. p. 12

[20] Ostrower J. GE plans 10% fuel burn improvement for GE9X engine. Flightglobal. Available from: https://www.flightglobal.com/ge-plans-10-fuel-burn-improvement-for-ge9x-engine/104377.article Accessed May 08, 2023]

[21] Inozemtsev AA, Sulimov DD. Experience and prospects of jsc

"UEC-AVIADVIGATEL" in the creation and operation of aircraft derivatives industrial gas turbine powerplants. In: Proceedings of the LXVIII Scientific and Technical Session on the Problems of Gas Turbines; 23–24 September 2021. Moscow: Russian Academy of Sciences, RAS commission on gas turbines, JSC Thermal Engineering Research Institute, Mosenergo PJSC. pp. 18-26

[22] Tiniakov DV, Utenkova VV. Analysis of trapezoidal wing shapes by particular criteria of their efficiency. The Designing and Manufacturing of Aircraft National Aerospace University 'Kharkov Aviation Institute'. 2012;**9**:54-60

[23] Kretov A, Tiniakov D. Evaluation of the mass and aerodynamic efficiency of a high aspect ratio wing for prospective passenger aircraft, Aerospace, MDPI. 2022. DOI: 10.3390/aerospace9090497

[24] Kretov A, Tiniakov D. Evaluation of wing structures at the conceptual stage of transport category aircraft projects. Aviation. 2022;**26**(4):235-243. DOI: 10.3846/aviation.2022.18041

[25] Tupolev AA. Clear sky variant. Technics of Youth. 1989;**1**:18-21

[26] NASA. X-57 Maxwell. NASA. LG-2018-04-048-AFRC. 2018;2

[27] Tiniakov D, Cheng Z, Liu J. Analysis of the aircraft noise impact on environment for determine the rational ways of its reduction. National University of Civil Protection: Technogenic and Ecological Safety. 2018;**3**:52-57

[28] ADI LLC. Noise map. In: Acoustic Design Institute LLC. 2018. Available from: https://iakbarier.ru/services/akusticheskie-raschety/razrabotka-kart-shuma/?PAGEN_2=3 [Accessed: August 5, 2023]

[29] Kovalev E, Tiniakov D, Riabkov V. Noise suppression capabilities by using honeycomb structures. National Aerospace University. Open Information and Computer Integrated Technologies. 2014;**63**:25-32

[30] Fomin A. PD-30 is thirty tones of the future. National Aerospace Journal Vzlet. 2012;**5**:95-96

Chapter 2

Impulse Measurement Methods for Space Micro-Propulsion Systems

Yang Ou, Yuqi Li, Yu Zhang, Jianjun Wu and Yuqiang Cheng

Abstract

Space micro-propulsion systems are increasingly considered an attractive option for station-keeping and drag-makeup purposes for the mass- and power-limited satellites due to their critical factors of simple design, small volume, and high specific impulse. These systems typically generate low-range thrust from nN to mN, and their impulses are less than mNs, making it difficult for conventional sensors to detect them directly. Consequently, the design of a special thrust stand is often necessary to measure these micro-propulsion systems. This chapter outlines recommended practices for the operation and calibration of three conventional measurement methods, along with the introduction of an impulse measurement stand developed at the National University of Defense Technology. The chapter presents the fundamentals, calibration method, and experimental results of the stand operation, while also analyzing error sources. Finally, the chapter discusses the demand and direction of micro-impulse measurement development.

Keywords: micro-propulsion system, impulse measurement, pendulum stand, electromagnetic compatibility technology, calibration method

1. Introduction

With the gradual refinement of the functions of satellite networking and space-based network information systems, the requirements for the propulsion system necessary for satellite missions are further increased [1–3]. Compared with the traditional chemical propulsion system, the electric propulsion system has the advantages of high specific impulse, lightweight, and long lifespan, so it gradually becomes a better scheme for satellite attitude control, orbit transformation, and drag compensation [1, 3, 4].

Electric thrusters are available in a plethora of types, each boasting unique operating principles and characteristics. Regardless of the specific type employed, however, all electric thrusters must undergo three essential steps: design, trial production, and testing. For the electric thruster, it needs not only the test link to evaluate and verify the function and performance, but also the test link to expose the thruster development issues and seek potential solutions. Therefore, the pre-research, pattern, prototype, and flight application stages of the electric propulsion system development are inextricably linked to the testing and measurement technology, which serves as an indispensable cornerstone of electric propulsion [5, 6].

Unlike chemical and cold air propulsion systems, electric propulsion systems typically require a vacuum environment for ignition testing and operation. Consequently, creating a high vacuum environment artificially becomes necessary during ground testing of electric propulsion. The research on electric propulsion encompasses development, testing, identification, and application, and the testing of electric propulsion systems runs through all aspects of scientific research.

There are numerous topics covered in electric propulsion testing, and some overlap between them, but the purpose of the testing is relatively clear, which can be divided into five categories according to the intended purpose [5, 6]:

1. Ignition test. The electric propulsion ignition test is a crucial means of obtaining important information about electric propulsion, including ignition start and steady-state operation tests. The ignition start test verifies successful and reliable ignition of the electric thruster, while the steady-state operation test ensures stable operation for a short time or a long time based on the ignition start test.

2. Performance measurement test. After ensuring the stable operation of the electric thruster, it is necessary to measure its performance parameters such as thrust, efficiency, specific impulse, and beam divergence angle to complete the evaluation of the comprehensive performance of the electric thruster.

3. Life test. The ground test was conducted to verify whether the accumulated working time and switching times of the electric thruster meet the design index or the requirements of the space mission.

4. Plasma diagnostics. Through an analysis of the plasma state of the electric thruster, it is possible to optimize the structural design of the thruster and evaluate the potential impact of the plume on the spacecraft.

5. Environmental adaptability test. Ensure that the reliability of the electric thruster meets the requirements of the ground test conducted in the satellite launch and on-orbit working environment, and verify the performance under the current working conditions.

Among the above five types of tests, the performance measurement test with micro-thrust and impulse measurement as the core is the main test item of the electric propulsion system. This measurement is an essential measurement link to evaluate the performance of the electric propulsion system and is also an important reference index to measure the stability of the electric propulsion system, which runs through all stages of the spacecraft, such as the single machine level, subsystem level, and the whole star level [7–10].

Combined with the principle, working environment, and thrust level of the electric thruster, the micro-thrust and impulse measurement test for the electric thruster have the following characteristics:

1. Small impulse. At present, the thrust range of commonly used electric thrusters, such as Hall thrusters and ion Hall thrusters, covers from micro-newton to nano-newton, while the impulse element of pulse-working electric thrusters generally ranges from micro-newton to milli-newton. Therefore, the micro-thrust and impulse measurement system needs to capture weak mechanical signals in small

time scales, and the measurement system needs to have high sensitivity, resolution, and anti-interference ability.

2. Low thrust–weight ratio. The thrust–weight ratio is the ratio of thrust to weight of an electric thruster. The thrust of the electric thruster is small, and the weight is large. Its thrust–weight ratio is usually between 10^{-7} and 10^{-3}, which is far less than that of the chemical propulsion system. Too low a thrust–weight ratio will lead to a negligible additional weight component that must be eliminated or suppressed; otherwise, it will bring obvious interference and error to the measurement of a small thrust or impulse. In addition, the sensitivity and load-bearing capacity of the measuring platform is often difficult to be compatible with. How to ensure that the resolution and sensitivity of the electric thruster can be improved as much as possible under the normal installation is always the core issue of micro-thrust and impulse measurement.

3. Measurement in a vacuum environment. Electric thrusters usually need to work in a vacuum environment, so the materials, components, sensors, and other equipment required for thrust measurement need to have the ability to work in a vacuum.

4. Interference factors. The thrust of the electric thruster is usually in the range of microns to microns, and the impulse element is in the range of microns to microns. Any small vibration and interference will affect the measurement. The key is to avoid the interference of cables and gas pipes, vibration interference, thermal impact, and electromagnetic interference.

2. Impulse measuring principle

The basic principle behind most existing measurement methods is to apply the thrust or impulse to be measured on the measuring platform, establish the functional relationship between the thrust and impulse, and the corresponding physical effect according to the mechanical response results of the measuring platform (e.g., vibration amplitude and rotation angle), and then calibrate the functional relationship through the standard force, thereby achieving the quantitative measurement of thrust and impulse. In electric thrusters, the key to micro-thrust and impulse measurement is to measure the variation of thrust with time. For thrusters operating in a transient state (e.g., pulsed plasma thrusters), the thrust action time is very short, and it is unnecessary or impossible to measure the variation of thrust with time. In this case, the thrust action effect can be expressed by impulse, which is also the impulse measurement [11–13].

2.1 Classification

At present, the commonly used methods for measuring thrust and impulse include the deformation structure method, balance method, torsion pendulum method, and cantilever beam method. According to the different mechanical response results of the thrust platform, they can be divided into the direct transfer measurement method, pendulum force measurement method, and target transfer measurement method.

2.1.1 Direct transfer measurement

The direct transfer measurement method refers to that the thruster being fixed directly on the force-measuring sensor or the thrust generated by the thruster being directly applied to the force-measuring sensor through the measuring platform. During the measurement, the thrust and impulse are identified by the sensor. This method is suitable for thrust measurement environments with large thrusts, such as chemical thrusters, electric arc thrusters, and resistance heating thrusters. The key to measurement is the measurement sensor. The commonly used sensors include a piezoelectric sensor, strain gauge sensor, and capacitance sensor [5, 13].

The direct transfer measurement method Is the preferred method for large thrust measurement. Its structure is relatively simple, and the measurement process is simple and fast. However, when the thrust magnitude is small, the mechanical signal is susceptible to be disturbed by environmental noise and mechanical vibration. This makes it difficult for the sensor to capture the weak mechanical signal.

2.1.2 Measurement method of swing force

In the pendulous force measurement method, the thruster is mounted directly on the measuring platform, which can measure the thrust and impulse of the thruster with a small force. The measurement accuracy and resolution are high, which is the current mainstream scheme of the thrust and impulse measurement of the electric thruster. As shown in **Figure 1**, the swing force measurement process essentially uses the thrust of the thruster to excite the pendulum structure bench and obtains the thrust or impulse in reverse calculation by calibrating the relationship between the motion law of the pendulum structure bench to the thrust or impulse [14, 15].

The specific implementation of the swing force measurement method includes closed-loop and open-loop measurement methods. In the closed-loop measurement, the electromagnetic force is used to compensate for the effect of the thrust so that the measurement platform is in the random equilibrium and the electromagnetic force equals to the thrust [16]. The closed-loop measurement method can eliminate the interference of gravity and material rigidity on the measurement, and the
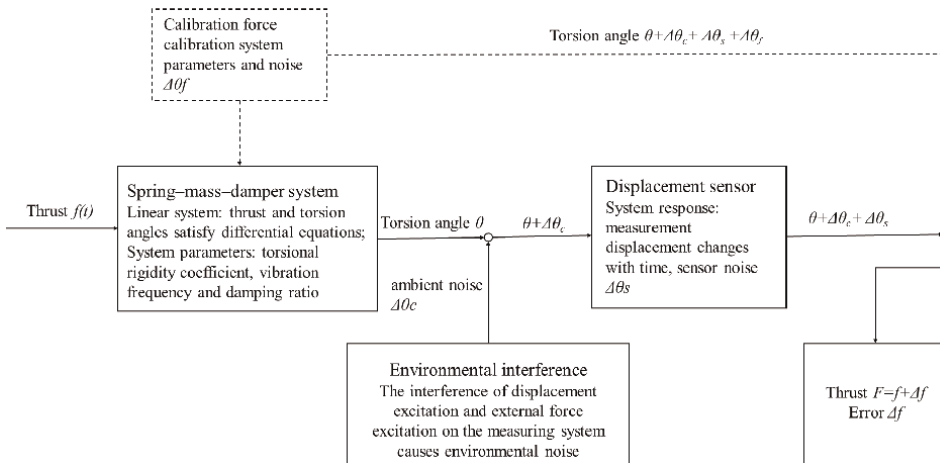
Figure 1.
Measurement principle of swing force.

measurement results are relatively more accurate. The open-loop measurement method usually records the position change of the pendulum and then calculates the thrust and impulse through the calibration of the standard force. The commonly used sensors for measuring the change of pendulum position include a laser displacement sensor, capacitance displacement sensor, laser angle sensor, and photoelectric sensor. In addition, to control the motion of the pendulum and quickly return to the equilibrium state after the measurement, the pendulum force measurement device is usually equipped with the corresponding dampers.

According to the structural form of the pendulum, the pendulum force measurement methods can be divided into three types: suspended pendulum, inverted pendulum, and torsion pendulum, as shown in **Figure 2**. Although the three structures are slightly different, they can be considered a "spring-mass-damper" system [9].

2.1.3 Target transfer measurement method

The target transfer measurement method is to impact the plume from the thruster on the target and calculate the thrust of the thruster by measuring the position change of the target under the impact force. **Figure 3** shows the schematic diagram of a typical target transfer measurement scheme, which consists of target, elastic beam, displacement sensor, and calibration device. The elastic beam with minimum rigidity is fixed with the target with maximum rigidity. When the plume from the thruster impacts the target, the elastic beam will deflect obviously, and the displacement sensor can measure the horizontal displacement of the elastic beam. Calibrate the horizontal displacement and standard force of the elastic beam through the calibration device, establish the corresponding functional relationship, and realize the accurate measurement of different thrust sizes. Most target structures are equivalent to simple pendulum structures, and their motion characteristics are similar to the pendulum force formula [17, 18].

Compared with the other two kinds of measurement methods, the target transfer measurement method is a non-contact indirect measurement, which can avoid the impact of measurement and control cable, thruster working noise, and vibration on the measurement results to a certain extent [5, 13, 16]. In addition, the target transfer measurement method has a simple structure and is easy to install and
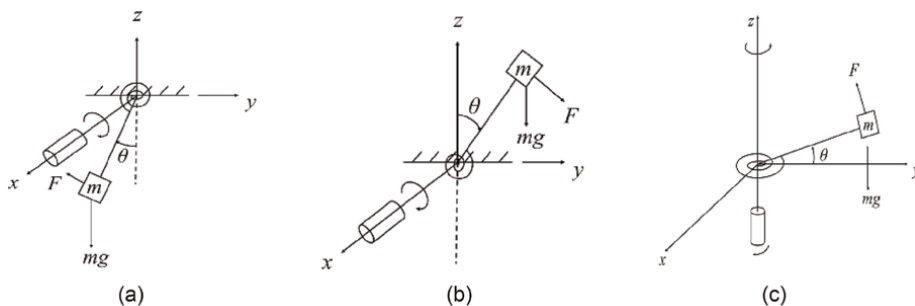
Figure 2.
Spring-mass-damper system. (a) Hanging pendulum, (b) inverted pendulum and (c) torsional pendulum.
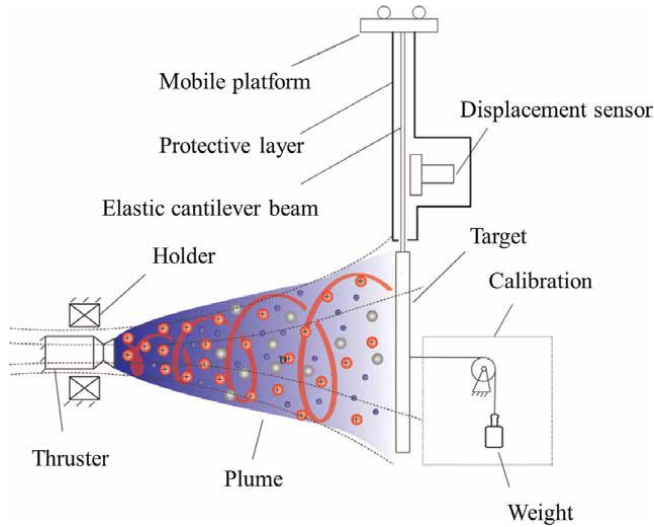
Figure 3.
Schematic diagram of a typical target transfer measurement.

implement. However, due to the effectiveness and secondary effects of the plume, the error is relatively large. The key points are as follows:

1. The plume is unable to ensure that all impacts are on the target and the actual impact level is less than the theoretical generation;

2. For the transient thruster operation, the motion of the plume has greater randomness, and the single impact force fluctuates greatly;

3. After the target impact, part of the plume will rebound, resulting in a larger measured value than the actual value;

4. The angle deviation of the elastic target is inevitable after being impacted, and the impact force of the plume will be partially lost [7, 11, 19, 20].

2.2 Calibration

At present, the principle of the mainstream measuring platform is almost based on the effect of force. The thrust is obtained by determining the basic parameters of the vibration system and measuring the displacement response of the vibration components and then by inversion according to the dynamic equation. The determination of the basic parameters of the vibration system is the calibration process, which applies a constant calibration force or calibration impulse to the measuring platform and then determines the system parameters according to the obtained system response and dynamic relationship [5]. Although the dynamic function can be calculated theoretically by obtaining the correlation coefficient of the measuring platform, it is more convenient, intuitive, and reliable to determine the system parameters through the calibration process.

In the process of micro-thrust and impulse measurement, the calibration process is indispensable. The first is to establish the functional relationship between thrust or impulse and displacement through the calibration process. The second is to determine the accuracy, repeatability, stability, and sensitivity of the measuring device by repeatedly loading the standard known force. The third is to avoid system error by comparing and correcting the measured value and theoretical value. Therefore, the repeatability, operability, adjustability, stability, and accuracy of the calibration device is one of the key technologies to ensure the performance of the micro-thrust measurement system and also an important basis to verify its measurement level.

According to whether the calibration force generation device is in direct contact with the measuring device, the calibration method can be divided into contact type and non-contact type. The contact calibration method includes the weight method and the impact hammer. The principle of the weight method is simple and easy to operate, but it is easy to be affected by sliding friction, air resistance, elastic expansion, and drag of the rope and limited by the minimum weight; it is difficult to provide high-precision micro-newton calibration force. The pendulum method uses a pendulum with a known mass to impact the measuring bench from a certain height to form an impulse with a known size. This method is also simple and easy to operate, but the error is large and difficult to control [12, 13, 21]. Non-contact calibration methods include the electrostatic comb method and the electromagnetic force method. The electrostatic comb method is usually composed of a group of interlocking non-contact comb teeth separated at very small intervals. The electrostatic repulsion force generated when approaching is used as the calibration force. It can not only provide a stable thrust but can also generate a high-accuracy impulse by controlling the number of comb charges and voltage application time. The electromagnetic force calibration method uses the magnetic effect of a current or the theorem of ampere force to generate a stable electromagnetic force, including the combination of a coil with a permanent magnet and the combination of an electromagnet with an energized wire. Similar to the electrostatic comb method, the electromagnetic force method can also generate stable calibration force and can also accurately generate calibration impulses of known size. In addition, the electromagnetic force is not easily affected by the external power supply line, and its accuracy is higher than that of the electrostatic comb method [22–24].

2.3 Performance metrics

The main technical indicators of the micro-thrust and impulse measurement platform include sensitivity, stability, accuracy, resolution, and response time.

2.3.1 Sensitivity

As the core technical index of the measuring platform, sensitivity, accuracy, and resolution are closely related, the definition of sensitivity in micro-thrust and impulse measurement is slightly different. Generally speaking, the sensitivity of steady-state micro-thrust measurement is the offset that the platform can achieve under a given thrust. As shown in Formula (2.7), the sensitivity is related to the length of the moment arm and the elastic coefficient and is regarded as the key index of the mechanical design of the measuring bench [5, 9].

2.3.2 Stability

In the process of micro-thrust and impulse measurement, it is necessary to ensure that the response of the measuring bench is consistent and repeatable; otherwise, the calibration will be meaningless, and the accuracy and accuracy of the measurement cannot be guaranteed. In addition, long-term measurement needs to ensure the long-term stability of the bench. There are two main factors that affect the repeatability of measurement. One is the zero drift, that is, the change of zero point or the actual position of the pendulum, and the other is the gain drift, that is, the change of response coefficient or elasticity coefficient. The temperature change or friction of mechanical or electronic components and elastic components will cause drift. In order to pursue the accuracy of measurement, the generation of drift should be avoided as much as possible [9, 21].

2.3.3 Resolution

Resolution is defined as the minimum difference in the response of the measuring platform after being loaded by two different thrusts or impulses. Resolution is the ability of the measuring platform to distinguish the mechanical effects of loading and is also a measure of the minimum value of thrust and impulse change of the measuring platform. The noise level of the measuring platform is directly related to the resolution, and high resolution can be achieved by minimizing the noise. In the process of micro-thrust and impulse measurement, the noise sources usually include the electrical noise of the sensor, the mechanical noise caused by environmental vibration, and the response change caused by the periodic change of temperature.

The resolution of the measuring bench can be quantified by continuously changing the magnitude of the loading force until the response cannot be resolved. However, in the actual measurement process, the error of this method is relatively large. Usually, the resolution is determined according to the measurement noise level, and the resolution can be specified to be twice the noise signal. The noise signal can be characterized by the ratio between amplitude and frequency or power spectral density [5, 8, 9, 25].

In the measurement process of an electric thruster, unless some measurement methods specifically use the resonance principle, the natural frequency between the electric thruster and the measuring platform should generally be avoided, so as to prevent the generation of resonance. In addition, to ensure the accuracy of measurement, the noise of the bench must be far less than the range of the thruster that can be produced by the thruster.

2.3.4 Response time

The response time of the measuring bench is an important indicator of dynamic measurement, which can be characterized by many parameters, such as rise time (the time required for the response to reach 100% of the steady-state value), peak time (the time required for the response to reach the peak value), and stability time (the time required for the response to change less than 2% near the steady-state value) [9].

2.3.5 Accuracy

Accuracy is a measure of the error between the measured value and the true value of the measuring bench. For a high-performance measuring bench, it is not only required to be sensitive enough, the results have obvious repeatability, not affected by

random errors, but also to ensure the measurement results [16]. In the measurement process, the system error is usually minimized to improve the measurement accuracy, and the accuracy needs to be calibrated through standard thrust and impulse. In addition, the calibration method needs to be strictly designed to avoid introducing new system errors.

3. Impulse measurement stand in NUDT

Since 1960s, researchers across the countries both domestically and internationally have successfully developed various micro-thrust/micro-impulse measurement devices, including balance, single pendulum, double pendulum, torsion pendulum, and cantilever beam. The measuring range of these devices is mostly in the millinewton scale, and some attempts have also been conducted for the lower scale. Based on the inverted pendulum structure, NASA uses capacitive displacement sensors and gravity accelerometers to detect the position change of the swing arm and then measure the thrust, which can achieve 0–700 μN measurement range, and the noise is less than 1 μN/Hz [26]. Researchers at the University of the Witwatersrand improved the torsion pendulum, which can achieve micro-newton thrust and 0.27–600 μN, the error of impulse measurement in the range of Ns is less than 4% [27]. NASA also developed a single-end fixed torsion wire suspension torsion pendulum, with a resolution of 25nN and a force measuring range of 100 nN $\sim$ 500 μN. The error is less than 25% [28]. Researchers at the University of Tokyo in Japan has developed an elastic pivot type non-equal arm torsion pendulum with a resolution of 0.7 μN·s impulse measurement [29]. Researchers at Huazhong University of Science and Technology have achieved a resolution of 0.09 μN with a maximum range of 264 μN micro-thrust measurement and a resolution of 0.47 μN·s with a maximum range of 1350 μN·s through a special suspension and torsional balance design for the torsional pendulum [30]. Although the measurement of thrust and impulse at the level of millinewton has reached a high level, there are still many difficulties in the measurement of thrust and impulse at the level of micro-nano or even nano-nano. For example, there is noise in the measuring instrument itself and the environment, which often submerges the measured signal and greatly affects the measurement accuracy. At the same time, when the micro-thruster works, the measuring platform will vibrate under the force, which will also affect the measuring accuracy. In addition, the vacuum pumping process will also have adverse effects on the vacuum chamber and internal measuring system. These difficulties lead to less thrust and impulse measurement methods of micro-newton magnitude and low accuracy. At the same time, it is extremely difficult for the existing international measurement technology to meet the requirements of integrated thrust/impulse measurement with a large range, high resolution, and high accuracy at the same time.

In order to realize the integrated measurement of micro-impulse, the National University of Defense Technology (NUDT) has built a C-tube torsion micro-impulse measurement method and a direct calibration method based on ampere force, which has solved the problems of weak signal sensing, anti-interference and anti-randomness, and online calibration, and developed a C-tube torsion micro-impulse measurement device and online calibration system as shown in **Figure 4**. The theoretically achievable micro-impulse measurement range is 100 nNs–100 mNs, The micro-thrust measurement range is 100 nN–100 mN, providing a necessary device for the development and engineering application of micro-nano satellite propulsion systems.
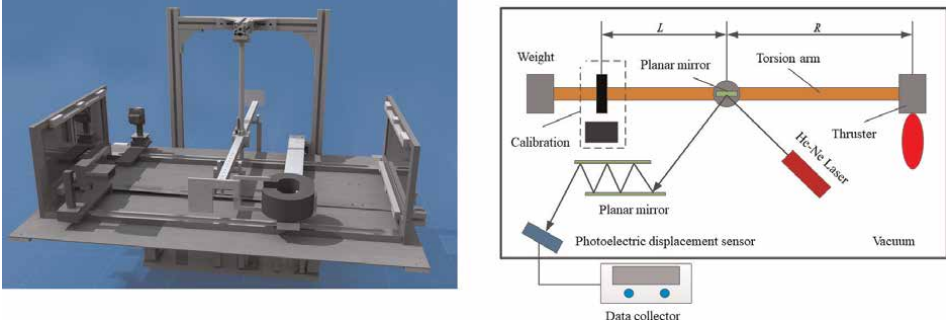
Figure 4.
C-tube torsion micro-impulse measurement device.

3.1 Fundamental theory

The C-tube torsion pendulum micro-impulse measurement system can be divided into the following subsystems: (1) displacement signal optical measurement subsystem, including He-Ne laser, planar mirror array, and photoelectric displacement sensor (PDS); (2) torsion pendulum structural parts, including torsion bar, swing arm, bracket, connecting parts, etc.; (3) damping and electromagnetic calibration subsystem, including several electromagnetic coils, permanent magnets, control circuits, etc. [21].

As shown in **Figure 4**, when the thruster works, its impulse will act on the torsion pendulum system. When the thruster works, its impulse will act on the swing arm and drive the torsion bar to rotate. The reflector installed on the swing arm reflects the laser beam emitted by the He-Ne laser to the remote PDS photosensitive surface. With the action of the impulse, the light spot produces a small displacement on the PDS photosensitive surface, which makes the PDS produce a small voltage signal output. Therefore, by calibrating the relationship between the impulse and the micro voltage signal, the corresponding micro-impulse can be calculated using the voltage signal.

The elastic element of the torsion pendulum is the key component of the torsion pendulum measurement system, which determines the mechanical response characteristics of the torsion pendulum, and is also an important component that affects the measurement performance of the torsion pendulum. According to the knowledge of engineering mechanics, it can be proved that within the elastic range of the material, the torsional deformation of the metal C-tube is strictly linear with the magnitude of the axial torque it is subjected to. The C-tube torsion pendulum measurement system uses this linear relationship to measure the impulse.

Assume that the wall thickness of the C-shaped tube is t, the length is l, the length of the cross-section centerline is m, the material shear modulus of elasticity is G, the rotational inertia of the torsion pendulum relative to the axis of the C-shaped tube is I, the impulse generated by the propulsion system is micro I_s, and the instantaneous rotational angular velocity of the torsion pendulum beam is w. When the torque T is loaded on the C-shaped tube, the torsional deformation generated is [31]:

$$T = \frac{2Gmt^3}{3l}\alpha \qquad (1)$$

where α is the torsion angle of the C-shaped pipe under the action of torque. By integrating formula (1), the rotation angle of the C-tube torsion beam can be obtained α_0, and its stored energy is [31]:

$$E = \int_0^{\alpha_0} T d\alpha = \int_0^{\alpha_0} \frac{2Gmt^3}{3l} \alpha d\alpha = \frac{Gmt^3 \alpha_0^2}{3l} \tag{2}$$

The motion of the torsion pendulum is fixed axis rotation, and its instantaneous kinetic energy is $Iw^2/2$. When the impulse Is acts on the torsion pendulum, the torsion pendulum starts to move. In the first quarter period of its movement, it can be considered that the energy is converted between the rotational kinetic energy of the torsion pendulum and the elastic potential energy stored in the C-tube, that is, the energy consumed by the C-tube is ignored. Let the initial angular velocity of the torsion pendulum beam be w_0, which can be obtained from the conservation of energy:

$$\frac{Iw_0^2}{2} = \frac{Gmt^3 \alpha_{max}^2}{3l} \tag{3}$$

where α_{Max} is the maximum swing angle of the torsion pendulum in the first quarter period of motion.

Let the distance between the impulse action point and the axis of the C-shaped tube be L_s, which can be obtained from the conservation of the moment of momentum:

$$I_s L_s = I w_0 \tag{4}$$

By combining Eqs. (3) and (4):

$$I_s = \frac{\alpha_{max}}{L_s \sqrt{\frac{2Gmt^3 I}{3l}}} \tag{5}$$

Combining Eqs. (1) and (5), it can be seen that when the C-tube torsion pendulum is under the action of static force or impulse, its static force and impulse values are linear with the mechanical response of the system.

When the pendulum is stationary, the total length of the optical path from the circular mirror to the PDS is L, and the displacement of the light spot on the PDS is s when the pendulum is stationary to moving. The PDS can convert the displacement signal to the voltage signal V for output. Set the gain coefficient of PDS signal conversion as μ, then there are:

$$s = L tan\alpha \tag{6}$$

$$V = \mu s \tag{7}$$

The relationship between voltage signal and impulse can be obtained from simultaneous formula (5)-(7) as follows:

$$I_s = \frac{V_{max}}{L_s \frac{1}{L\mu} \sqrt{\frac{2Gmt^3 I}{3l}} \frac{\alpha_{max}}{tan\,\alpha_{max}}} \tag{8}$$

The impulse generated by the micro-nano satellite propulsion system is very small, corresponding to the maximum swing angle generated α Max is smaller, at this time $\alpha_{max}/tan\alpha_{max} \approx 1$. Therefore, formula (8) can be simplified as:

$$I_s = \frac{V_{max}}{L_s \frac{1}{L\mu} \sqrt{\frac{2Gmt^3I}{3l}}} \tag{9}$$

If $K=\frac{1}{LL_s\mu} \sqrt{\frac{2Gmt^3I}{3l}}$, the K value can be determined by calibrating the torsion pendulum system, and then, the measurement impulse can be calculated by recording the maximum voltage Vmax displayed on the PDS.

3.2 Calibration

The establishment of a highly sensitive micro-impulse measurement platform enables accurate measurement of the thrust and impulse of the micro-thruster. In order to accurately measure thrust and impulse and ensure that the system operates properly and performs well, the measuring system must be calibrated as accurately as possible. Calibration is a necessary step prior to all accurate measurements, and the accuracy of calibration directly affects the accuracy of the measurements system. There are many kinds of calibration methods, and more than one method of calibration for the same measurement system. The measurement system should use the calibration method as accuracy as possible. The high-precision electromagnetic calibration technology based on pulsed ampere force uses the energized copper wire to pass through the magnetic field orthogonal to it to generate ampere force and uses this ampere force to act on the measuring bench as the calibration force, effectively solving the high-precision calibration problem of the C-tube torsion pendulum measuring device.

For a ring electromagnet, as shown in **Figure 5**, when the cross-sectional area and permeability of the electromagnet are the same everywhere, a magnetic circuit will be generated in the electromagnet and the magnetic lines of force will be basically concentrated in the magnetic core. When the air gap height is small, most of the magnetic force lines pass through the air gap, and only a few of the magnetic force lines are outside the air gap. In most areas of the air gap, the magnetic induction intensity is uniform, and at the edge of the air gap, the magnetic induction intensity drops rapidly. The software Ansoft is used to carry out a numerical simulation on the magnetic induction intensity of the air gap and its periphery, and the magnetic induction intensity distribution on the middle cross-section of the annular magnetic gap is obtained, as shown in **Figure 6**. In the simulation, the electromagnet material is silicon steel, the electromagnet coil is 200 turns, the energizing current is 0.5 A, the gap section area is, and the gap spacing is 2 mm. It can be seen from **Figure 6** that
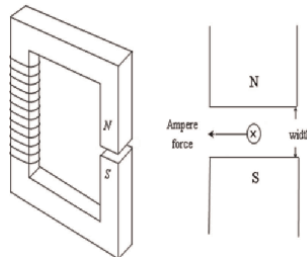
Figure 5.
Ampere force in annular magnet and gap.
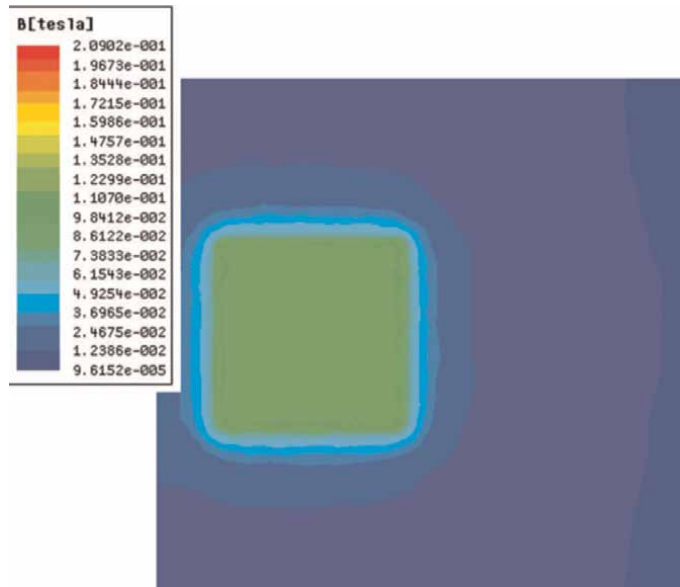
Figure 6.
Distribution of magnetic induction intensity.

when the volume is $2 \times 15 \times 15$ mm^3, the uniformity of magnetic induction intensity is satisfied.

In magnetic field *B*, the force on the current-carrying conductor can be expressed as

$$df = I_C \cdot dl \times B \tag{10}$$

Therefore, when the electrified straight wire is in the gap, it will be affected by the magnetic field. The force is called ampere force, that is, *L* is the effective length of the straight wire with current I_C in the uniform magnetic field with strength *B*.

$$F = BI_C L \tag{11}$$

Due to the edge effect of the magnetic field, it is difficult to calculate the ampere force through Eq. (11). However, when the magnetic field remains constant and *L* remains constant, the ampere force will be proportional to the coil current. In addition, when the current in the copper coil remains constant, the ampere force will be constant. As shown in **Figure 7**, the ampere force can be obtained by the physical analysis balance weighing method, and then it can be used as the calibration force. Different coil currents will correspond to different ampere forces for calibration. If there is a pulsed current in the coil, a pulsed ampere force will be generated between the coil and the magnetic field. By integrating the pulse ampere force with time, the impulse received by the copper coil can be obtained and then used as the impulse required for calibration.

Another advantage of this electromagnetic calibration method is that the ampere force is not sensitive to the angular displacement of the force arm. This is because the magnetic field is uniform in a large range of the electromagnet gap. Therefore, as long as the energized wire is not close to the edge of the gap, the generated ampere force will not be affected by the position of the copper wire. No matter how the position of
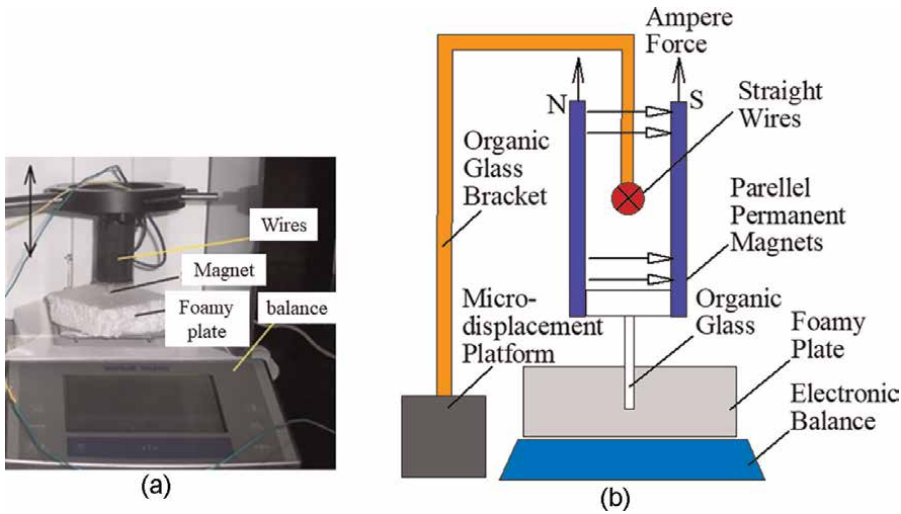
Figure 7.
Measuring ampere force with physical analytical balance. (a) Physical measurement diagram (b) schematic diagram.

the copper wire changes, as long as the copper wire enters and exits from one side of the air gap, the ampere force will remain unchanged, thus ensuring the accuracy of the calibration process.

3.3 Electromagnetic compatibility technology

In the electronic circuit system, when there is a high-frequency circuit, the circuit will radiate electromagnetic waves to the outside, or some parts of the system use components that can radiate electromagnetic waves. These radiated electromagnetic waves will interfere with other nearby equipment and will be coupled to the circuit through wires and various connectors, causing interference to the signal in the circuit. There are also many elements with antenna functions in the circuit system, such as cables, printed circuit boards, and some mechanical structures. These elements can be coupled to other lines in the form of electric and magnetic fields, causing interference to the system. Electromagnetic compatibility (EMC) of equipment or system refers to the ability of equipment or system to work normally in an electromagnetic environment without causing unbearable electromagnetic interference to any other thing in the environment.

The project team has analyzed and studied the electromagnetic compatibility technology of the C-tube torsion pendulum micro-thrust/micro-impulse measuring device and processed the line shielding, grounding, lapping technology, and signal filtering technology for the system according to the actual situation, and finally carried out a comparative study of the influence of the electromagnetic compatibility technical measures on the measured signal of the system. The research results show that these processes reduce noise and improve the signal-to-noise ratio to a certain extent, but at the same time, it is also concluded that electromagnetic compatibility technology is not perfect, and it is difficult to completely eliminate noise and obtain clean measured signals by using electromagnetic compatibility technology alone. It is also necessary to filter the signal data by software, and the combination of the two can obtain more ideal signal data.

3.4 Experimental measurement

The thrust of the thruster with known parameters is measured to further verify the accuracy of the measurement method. The overall test device is shown in **Figure 8**. The thruster is installed on one side of the torsion pendulum. When the thruster works, its impulse will act on the torsion pendulum system. When the thruster works, its impulse will act on the swing arm and drive the torsion bar to rotate; The reflector installed on the swing arm reflects the laser beam emitted by the He-Ne laser to the remote PDS photosensitive surface; With the action of the impulse, the light spot produces a small displacement on the PDS photosensitive surface, which makes the PDS produce a small voltage signal output.

The measurement results of micro and thrusts and impulses are shown in **Tables 1** and **2**. According to the results in the table, this measuring device can realize the measurement of thrust and impulse of microns. At the same time, the resolution of PDS can be further improved and more sensitive materials can be selected to excavate higher resolution. In theory, this measuring device can achieve at least 100 nN and 100 nN·s measurements.

3.5 Error analysis

According to the possible error sources, the measurement error sources of the C-tube torsion pendulum are divided into the error introduced by the optical lever structure, the error introduced by the PDS sensor, and the error introduced by the acquisition card and the calibration error. The optical lever is used to measure the mechanical response of the C-tube torsion pendulum, and its structure affects the resolution of the C-tube torsion pendulum. PDS is a part of the optical lever and a sensor sensitive to the change of light spot displacement. Its resolution and optical path of the optical lever together determine the resolution of the C-tube torsion pendulum. The acquisition ability of the data acquisition card determines the system's ability to capture signals, and the acquisition accuracy of signals also affects the accuracy of the system's measurement results. Calibration is the basis for accurate measurement of C-tube torsion pendulum, and the calibration error introduced by calibration will be directly introduced into the measurement results. Other factors that may cause the measurement error of the system include the mechanical vibration of the system, the imperfection of the measuring circuit, and some undetected influencing factors. The mechanical vibration of the system will cause the vibration of the
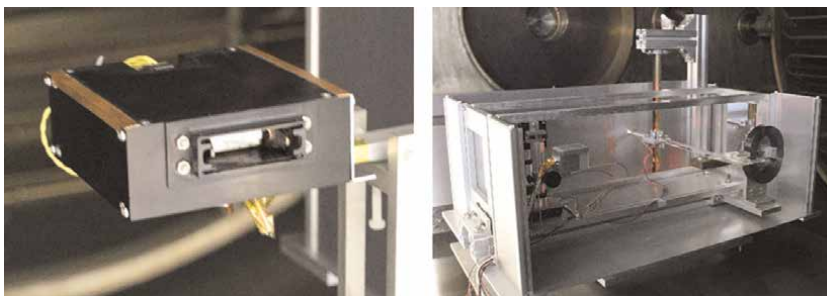
Figure 8.
Test device.

Theoretical thrust (μN)	Measuring voltage (V)	Measuring thrust (μN)
25	0.00116	26.721
50	0.00698	48.398
100	0.01860	104.487
150	0.03023	158.843
200	0.04186	211.273
250	0.01860	267.128
1250	0.11163	1208.676
2500	0.22790	2581.426
12,500	1.15814	12700.4687

Table 1.
Measuring results of thrusts.

Theoretical impulse (μN s)	Measuring voltage (V)	Measuring impulse (μN s)
10	0.04186	9.870
20	0.08837	20.345
40	0.18140	39.898
60	0.27742	62.448
80	0.36774	81.539
100	0.46065	107.352
500	2.32093	513.682
1000	4.64651	1089.613
5000	23.25116	5204.365

Table 2.
Measuring results of impulses.

C-tube, plane mirror, laser light source, and other structures of the system. The vibration of these structures will cause the vibration of the measuring optical path and cause low-frequency vibration interference to the measuring signal. The preliminary measurement circuit is not optimized, and the circuit itself may affect the quality of the measured signal, resulting in the reading error of the signal.

At the same time, the measuring range of the C-tube torsion pendulum is related to the machining accuracy and assembly accuracy when machining structural parts. For example, the beam and C-shaped tube, in order to ensure that the torsion pendulum has sufficient accuracy and resolution, the beam should have sufficient strength, and the processing should have good symmetry. When cutting an ordinary tube into a C-shaped tube, it should ensure sufficient cutting accuracy; otherwise, it will affect the mechanical properties of the C-shaped tube. During assembly, the structural dimension shall be measured before assembly. In the optical lever structure, the biggest influence on the measurement is the angle between PDS and incident light.

When the pendulum is still, PDS and incident light should be perpendicular, so the measurement model can be approximated as a linear model. Although this introduces method error, the relative error introduced by this approximation is very small. When the pendulum swing angle is 1 degree (actually far less than 1 degree), the relative error introduced by the approximation is about 0.1%. The relative position of the parallel plane mirror will affect the size of the system error. The larger the included angle of the plane mirror, the greater the system error caused, and of course, the greater the impact on the measurement results. Therefore, one of the mirrors can be installed on an adjustable platform, and the platform can be used to adjust the two mirrors close to the parallel state. The installation accuracy of the circular reflector does not need to be particularly high, but the connection between the circular reflector and the C-tube must be ensured to be tight enough.

4. Conclusion

Summarize the current status of micro-impulse measurement. To improve measurement accuracy, the following key technologies remain to be explored.

4.1 Environmental noise control technology

The system response measurement error caused by environmental noise interference is the dominant factor that causes thrust or impulse measurement errors. Therefore, environmental noise interference suppression technology is one of the key technologies for thrust or impulse measurement.

The challenge in suppressing environmental noise interference lies in its multi-source and diverse effects. Therefore, the research on the control technologies for environmental noise interference should focus on the identification of noise sources. These sources can be complex, including displacement hidden excitation interference, external force excitation interference, thrust or impulse loading interference, as well as the sight and drag interference caused by thruster connecting pipelines and cables, and the measurement error of displacement sensors.

4.2 High compensation system response measurement technology

The thrust or impulse is obtained from the inverse calculation of the measurement system response. The precision regarding the response of the measurement system will directly affect the accuracy of the thrust or impulse measurements. Therefore, high-precision system response measurement technology is one of the key technologies for thrust or impulse measurement.

The challenge of high-precision system response measurement is the measurement of small system response under environmental noise interference and small thrust-to-weight ratio. Spaceborne thruster (e.g., micro-thruster) has a very small thrust-to-weight ratio, which means that when carrying a thruster to measure thrust, the rotational inertia of the rotating parts of the measuring system is large, and the thrust that the thruster can generate is relatively small, so the displacement generated by thrust is very small, and there is also the impact of environmental noise interference, involving environmental noise interference and high-precision measurement of small displacement under small thrust-to-weight ratio.

4.3 High-precision calibration technology

Thrust or impulse measurement is to use the vibration differential equation of the measurement system to calculate thrust or impulse inversely. The calibration accuracy of system parameters will directly affect the accuracy of the thrust or impulse measurement. Therefore, high-precision system parameter calibration technology is one of the key technologies of thrust or impulse measurement. The difficulty of high-precision system parameter calibration is the suppression of environmental noise interference and the generation of high-precision constant force. In addition to the influence of environmental noise on the calibration accuracy of system parameters, the generation and acquisition method of high-precision constant force is an effective technical way to improve the calibration accuracy of system parameters.

4.4 High-precision evaluation technology

Thrust or impulse measurement is to give the measurement results of micro-thrust or impulse of millinewton (s) or even micro-newton (s) under the conditions of environmental noise interference suppression, micro-system response measurement, and high-precision system parameter calibration, as well as the evaluation conclusions with high confidence. Therefore, high-precision thrust or impulse measurement and evaluation technology is one of the key technologies of thrust or impulse measurement.

Acknowledgements

Conflict of interest

The authors declare no conflict of interest.

Author details

Yang Ou*, Yuqi Li, Yu Zhang, Jianjun Wu* and Yuqiang Cheng
College of Aerospace Science and Engineering, National University of Defense
Technology, Changsha, Hunan, China

*Address all correspondence to: ouyang16@nudt.edu.cn; jjwu@nudt.edu.cn

IntechOpen

References

[1] Levchenko I, Xu S, Teel G, Mariotti D, Walker MLR, Keidar M. Recent progress and perspectives of space electric propulsion systems based on smart nanomaterials. Nature Communications. 2018;**9**(1):879. DOI: 10.1038/s41467-017-02269-7

[2] Levchenko I, Xu S, Mazouffre S, Lev D, Pedrini D, Goebel D, et al. Perspectives, frontiers, and new horizons for plasma-based space electric propulsion. Physics of Plasmas. 2020;**27**(2):020601. DOI: 10.1063/1.5109141

[3] Levchenko I, Bazaka K, Ding Y, Raitses Y, Mazouffre S, Henning T, et al. Space micropropulsion systems for Cubesats and small satellites: From proximate targets to furthermost frontiers. Applied Physics Reviews. 2018;**5**(1):011104. DOI: 10.1063/1.5007734

[4] Dale E, Jorns B, Gallimore A. Future directions for electric propulsion research. Aerospace. 2022;**7**(9):120. DOI: 10.3390/aerospace7090120

[5] Kang X, Liu J, Qiao C, Zhang Y. Space Electric Propulsion Test Measurement Technology. Beijing: Science Press; 2020 (in Chinese)

[6] Wang M, Zhong X, Wang Y. General Design of Electric Propulsion Spacecraft. Beijing: Science Press; 2019 (in Chinese)

[7] Zhang H, Li DT, Li H. Development of a cantilever beam thrust stand for electric propulsion thrusters. Review of Scientific Instruments. 2020;**91**(11):115104. DOI: 10.1063/5.0027911

[8] Asakawa J, Nishii K, Nakagawa Y, Koizumi H, Komurasaki K. Direct measurement of 1-mN-class thrust and 100-s-class specific impulse for a CubeSat propulsion system. Review of Scientific Instruments. 2020;**91**(3):035116. DOI: 10.1063/1.5121411

[9] James E, Anthony P. Recommended practice for thrust measurement in electric propulsion testing. Journal of Propulsion and Power. 2001;**33**(3):539-555. DOI: 10.2514/1.B35564

[10] Ou Y, Zhang Y, Wu J, Tan S, Du X. Measurement method by inferring the thrust from the stress of the cantilever beam based on the photoelasticity theory. Applied Optics. 2019;**58**(36):9746. DOI: 10.1364/AO.58.009746

[11] Wang D, Ye J, Li N, Wang Q, Wang J. A method of Micro-impulse measurement based on cantilever beam structure. Instrument Technique and Sensor. 2019;**3**(6):39-44. DOI: 10.3969/j.issn.1002-1841.2019.03.009

[12] Ou Y. Research on Thrust Measurement Method of Plasma Thruster Based on Stress Detection Technology. Changsha: National University of Defense Technology; 2018 (in Chinese)

[13] Mo X. Research on Micro Bull Thrust Measurement Technology. Chengdu: University of Electronic Science and Technology; 2019 (in Chinese)

[14] Hong Y, Jin X, Ye J, Zhou W. Microthrust and Microimpulse Measurement and Error Analysis Methods. Beijing: Science Press; 2017 (in Chinese)

[15] Hong Y, Li D, Feng X, Jin X, Wang S. Measurement and Evaluation Methods for Propulsion Performance of Spaceborne Microthrusters. Beijing: Science Press; 2021 (in Chinese)

[16] Kakami A. Chapter 8 - thrust measurement. In: Cheah KH, editor. Space Micropropulsion for Nanosatellites. Elsevier; 2022. pp. 197-243. DOI: 10.1016/B978-0-12-819037-1.00010-4

[17] Weng H, Cai G, Liu L, Zheng H, Zhang M, Zhang B. Modifying the theoretical model of the target indirect measurement method for measuring the thrust of electric propulsion. Measurement Science and Technology. 2021;**32**(8):085301. DOI: 10.1088/1361-6501/abe509

[18] Wang B, Yang W, Tang H, Li Z, Kitaeva, et al. Target thrust measurement for applied-field magnetoplasmadynamic thruster. Measurement Science and Technology 2018;**29**:075302. DOI: 10.1088/1361-6501/aac079

[19] Zhang H, Li DT, He F, Chen XW. Development of an indirect thrust stand based on a cantilever beam. AIP Advances. 2021;**11**(3):035006. DOI: 10.1063/5.0041530

[20] Meng H, Lou J, Chen T, Xu C, Chen H, Yang Y, et al. Cantilever-based micro thrust measurement and pressure field distribution of biomimetic robot fish actuated by macro fiber composites (MFCs) actuators. Smart Materials and Structures. 2021;**30**(3):035001. DOI: 10.1088/1361-665X/abdaa9

[21] Lu G. Research on High Precision Micro Impulse Measurement Technology of PPT. Changsha: National University of Defense Technology; 2014 (in Chinese)

[22] Feng X, Hong Y, Cui H, Feng G. Numerical simulation and experimental research of high-precision electromagnetic calibration force. Journal of Propulsion Technology. 2021;

43(8):1-18. DOI: 10.13675/j.cnki. tjjs.210806

[23] Chang H, Ye J, Chen Y, Zhou W. Research on electromagnetic constant force characteristics for micro thrust measurement, infrared and laser engineering. Infrared and Laser Engineering. 2019;**6**:147-152. DOI: CNKI: SUN:HWYJ.0.2019-S1-021

[24] Wang D, Jin X, Zhou W. Design and implementation of an electromagnetic force calibration device for micro thrust measurement, military automation. Ordnance Industry Automation. 2017;**36**: 68-72. DOI: 10.7690/bgzdh.2017.09.017

[25] Conde L, Lahoz MD, Grabulosa J, Hernández R, González J, Delgado M, et al. Thrust stand based on a single point load cell for impulse measurements from plasma thrusters. Review of Scientific Instruments. 2020;**91**(2):023308. DOI: 10.1063/1.5127189

[26] Jarrige J, Thobois P, Blanchard C, Elias PQ, Packan D, Fallerini L, et al. Thrust measurements of the Gaia Mission flight-model cold gas thrusters. Journal of Propulsion and Power. 2014; **30**(4):934-943. DOI: 10.2514/1.B35091

[27] Lun J, Law C. Direct thrust measurement stand with improved operation and force calibration technique for performance testing of pulsed micro-thrusters. Measurement Science and Technology. 2014;**25**(9): 095009. DOI: 10.1088/0957-0233/25/9/095009

[28] Phipps CR. A low-noise thrust stand for microthrusters with 25nN resolution. In: AIP Conference Proceedings. Nara (Japan): AIP; 2006. pp. 492-499. DOI: 10.1063/1.2203291

[29] Koizumi H, Komurasaki K, Arakawa Y. Development of thrust stand

for low impulse measurement from microthrusters. Review of Scientific Instruments. 2004;**75**(10):3185-3190. DOI: 10.1063/1.1790568

[30] Yang YX, Tu LC, Yang SQ, Luo J. A torsion balance for impulse and thrust measurements of micro-Newton thrusters. Review of Scientific Instruments. 2012;**83**(1):015105. DOI: 10.1063/1.3675576

[31] Zhang D, Wu J, Zhang R, Zhang H, He Z. High precision micro-impulse measurements for micro-thrusters based on torsional pendulum and sympathetic resonance techniques. Review of Scientific Instruments. 2013;**84**(12): 125113. DOI: 10.1063/1.4850615

Chapter 3

Matter/Anti-Matter Propulsion

Mark Pickrell

Abstract

One of the key potential technologies for generating high speeds in space is matter/anti-matter annihilation. With the Compton effect, if positrons and electrons can be annihilated in a controlled way, and in sufficient quantities, then humans are able to achieve relativistic speeds in space. This chapter describes a technology, matter/anti-matter propulsion, which is likely to enable the generation of relativistic speeds in space. To explain this technology, background information and prior efforts to promote matter/anti-matter annihilation as a propulsion source are introduced. Further, based on recent experiments conducted in the United States and Germany, the theoretical feasibility of generating relativistic speeds in space is explained. Finally, initial experiments designed to evaluate matter/anti-matter propulsion are described.

Keywords: matter, anti-matter, annihilation, Compton effect, relativity, relativistic speed, photon rocket

1. Introduction

This book is an outgrowth of the reality of the limitations of the speeds of chemical rockets. As Tsiolkovsky demonstrated over 100 years ago, the speeds achievable by chemical rockets are, in practice, limited by the exhaust speeds of their thrusters and the energy density of their propellants, because chemical rockets must push all their fuel as they accelerate [1].

Many technologies have been proposed to propel spacecraft faster than can be achieved with chemical rockets: ion propulsion, fusion propulsion, space sails, etc. This chapter is concerned only with matter/anti-matter propulsion. Based on fairly recent experiments conducted at Lawrence-Livermore National Laboratory (LLNL) [2] and the Max Planck Institute for Plasma Physics (MPIPP) [3], matter/anti-matter annihilation appears to be a promising candidate for dramatically exceeding speeds capable by chemical-rocket technologies. Most importantly, it appears that matter/anti-matter annihilation is a likely propulsion source for generating relativistic speeds in space—speeds that are a significant fraction of the speed of light.

In order to understand the possibilities of matter/anti-matter propulsion, it is necessary to understand: (1) the nature of light, matter, and anti-matter; (2) how light and matter interact; (3) how anti-matter can be generated; and (4) how the generation and annihilation of matter with anti-matter can propel a spacecraft. With these principles established, it is possible, as a theoretical matter, to anticipate the speeds that may be reached using matter/anti-matter propulsion.

The project of realizing matter/anti-matter propulsion is exciting, and the impact of successful development of this technology would be profound. With matter/anti-matter propulsion, the nearest stars are within our reach. This chapter is intended to show that the technology necessary for interstellar travel has already been demonstrated in the laboratory.

To the greatest extent possible, this chapter starts with basic concepts and works through to likely theoretical outcomes, with the intention to be readable and understandable for a general audience. It is hoped that scientists and engineers who are well-versed in these basic concepts will, with understanding, tolerate the simplest information provided here.

2. The problem: the Tsiolkovsky equation and its implications

The basic structure of a rocket is well-known. Demonstrating Newton's Third Law ("For every action, there is an equal and opposite reaction"), when a gas (particularly, a hot, expanding gas) exists within an open-ended chamber, the unequal distribution of forces within the chamber causes the gas to push the rocket forward. **Figure 1** shows the basic application of Newton's Third Law in a "balloon" rocket; chemical rockets work the same way.

Chemical rockets work by burning a fuel (such as liquid oxygen, or a solid combustible compound) inside a thruster. The hot, expanding gases in the thruster push the rocket forward. There is a practical limit to the speeds that can be achieved by chemical rockets, however, because they must "push" all of their own fuel. In 1896, Konstantin Tsiolkovsky, the great Russian rocket scientist, determined the formula for calculating a change in rocket velocity. The formula is:

$$\Delta v = v_e \bullet \ln\left(m_0 / m_f\right), \tag{1}$$

where v_e is the velocity of the rocket's exhaust, m_0 is the initial mass of the rocket, and m_f is the mass of the rocket at the end of the burn [4].

Importantly, because the change in speed of a rocket is a logarithmic function of the ratio of the change in the rocket's mass, and because the change in speed is a direct function of the exhaust's velocity, there is a practical limit to the speeds achievable by chemical rockets. The more mass the rocket must have (in fuel weight), the less it is able to accelerate. For that reason, much of twentieth-century rocket technology involved
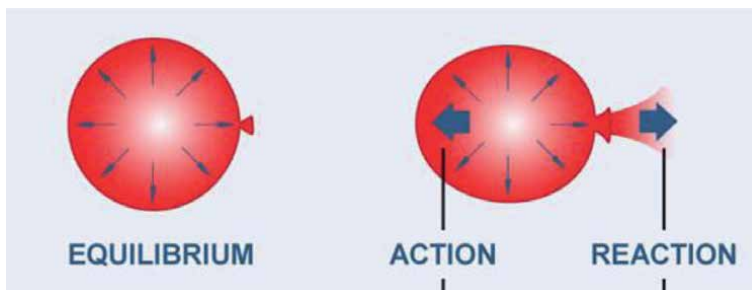

Figure 1.
Rocket principle (courtesy Mustang Publishing).

increasing both the velocity of exhaust and the energy density of fuel, while building multiple stages to achieve escape velocity. (When a stage drops off, the mass of the rocket is decreased, increasing potential acceleration of the rocket for the next given period of time.) The United States' Apollo V rocket, with its dense fuel (liquid oxygen), high-speed fuel pumps, and its multiple stages, is a perfect example of the practical implications of Tsiolkovsky's rocket equation when applied to chemical rockets.

Matter/anti-matter rockets work under the same principle as chemical rockets, only light itself (specifically, 511-keV gamma rays) is the propellant. The velocity of the "exhaust" of a matter/anti-matter rocket is the speed of light; the change in mass of the rocket as it accelerates is virtually zero. For that reason, matter/anti-matter rockets, as a practical implication of Tsiolkovsky's equation, given enough time, can achieve speeds that are a significant fraction of the speed of light.

3. Fundamental background: the nature of matter, anti-matter, and light

3.1 The nature of matter & anti-matter

Matter is the "stuff" that you know. It's the material that you can touch and feel, that you can breathe. It's the material that makes you.

In a basic way, matter is composed of protons, neutrons, and electrons. Protons have a positive electrical charge, neutrons have no electrical charge, and electrons have a negative electrical charge. Protons and neutrons are heavy, and electrons are very light, but electrons are not weightless. **Figure 2** shows a "planetary model" of a helium atom, with electrons "orbiting" the nucleus of the atom.

Anti-matter is the mirror opposite of matter. In a basic way, it is composed of anti-protons, anti-neutrons, and positrons. ("Positron" is the "P" in "PET" scan, for example.) Anti-protons have a negative electrical charge, anti-neutrons have no electrical charge, and positrons have a positive electrical charge. Anti-protons and anti-neutrons are heavy, and positrons are very light. But, as with electrons, positrons are not weightless. **Figure 3** shows an anti-matter "helium" atom, a mirrored concept of a helium atom.

When our universe was first created, there were probably equal amounts of matter and anti-matter. For some reason, our universe ended up being composed almost entirely of matter. Nonetheless, when an electron and a positron collide, they are annihilated—reduced to nothing. No mass, no electrical charge. But they do expel two
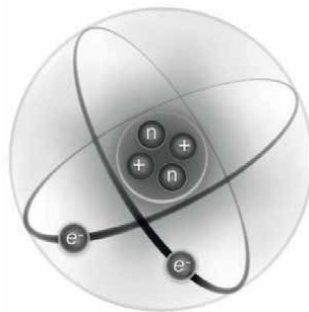

Figure 2.
Basic model of a helium atom (courtesy Mustang Publishing).

Figure 3.
Basic model of an anti-helium atom (courtesy Mustang Publishing). (Note: the symbol "p+" is used to show the positron. It is used here for a general audience, for ease of understanding; it should be noted that the international scientific convention for positrons is "e+").
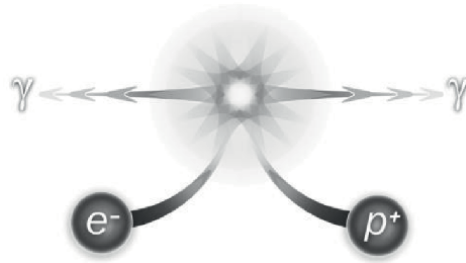
Figure 4.
Electron/positron annihilation (courtesy Mustang Publishing).

rays of light, called gamma rays ("γ"), in opposite directions, as well as a neutrino (or neutrinos—the exact number produced in an annihilation is unknown), a light, extremely fast particle with no electrical charge. The gamma rays produced in an electron-positron annihilation possess the energy of 511,000 electron volts, usually represented as "511-keV" [5]. **Figure 4** conceptualizes the collision of an electron and positron, resulting in their annihilation and the creation of two gamma rays; the resulting neutrino or neutrinos is/are not shown.

3.2 The nature of light

In addition to matter, our universe contains energy, particularly light and gravity.

Gravity is what holds you to the ground. Isaac Newton, famously, is said to have thought of gravity as the force that causes an apple to fall from a tree and hit the ground.

Light is the energy that lets you see, or makes a radio work, or makes an x-ray machine work. In a basic way, light can be thought of as a bit like the waves on a lake. Our understanding of light-as-a-wave began in 1803 with Thomas Young, who conducted the first experiment that we now call the "double slit" experiment [6]. It showed that light, traveling through two separate, but close, slits, creates a pattern that is just like the pattern made by waves of water after a splash hits near two piers.

But light can also be thought of as particles—a thing that goes from one place to another. The light from distant stars, for example, looks to us like a single point, without a wave aspect at all. Albert Einstein received the Nobel Prize in Physics in
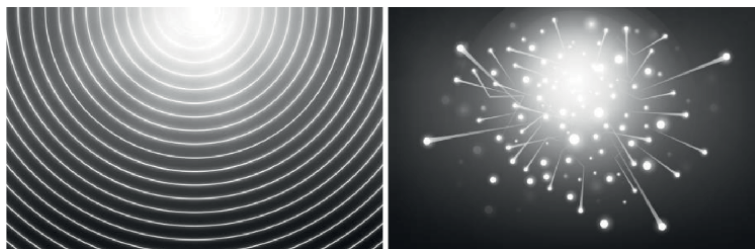
Figure 5.
Light as a wave, light as particles (courtesy Mustang Publishing).

1921 for his discovery of the "photoelectric effect," which demonstrates that light, in some ways, acts as if it is made of particles.

So light has a dual nature. In some ways, it's like a wave, and in some ways it's like a particle—like a golf ball hit by a golf club. Thinking of light as a particle helps one analogize matter/anti-matter rockets with chemical rockets. Instead of the gaseous particles that propel chemical rockets, matter/anti-matter rockets use light "particles" to propel the rocket forward. **Figure 5** visualizes our two ways of thinking about light: light as waves and lights as particles.

4. Interactions between light and matter, including the Compton effect

When we think of light as particles, we call these particles photons. The energies of photons constitute a continuous spectrum, from lowest energies to highest (and longest wavelengths to shortest), called the "electromagnetic spectrum": radio waves, microwaves, infrared, visible light, ultraviolet, X-rays, and gamma rays.

Photons interact with matter in a number of ways. Photons can be absorbed by matter. Photons can be reflected by matter. At higher energies, light can push matter. Arthur Compton won the Nobel Prize in 1927 for demonstrating that X-rays push the electrons of matter, depending upon the angle that the photons strike the electrons of the material [7]. At even higher energies, photons, in a process known as the Bethe-Heitler Process, can cause pairs of electrons and positrons to be ejected from an atom. It is generally understood that the electrons and positrons produced in the Bethe-Heitler Process arise from the "quantum vacuum" [8]. **Figure 6** shows

Figure 6.
Photon interaction with lead, as a function of photon energy [9].

the interaction of photons at various energies interacting with lead; the photoelectric effect, Compton scattering, and Bethe-Heitler pair production are shown (Rayleigh scattering is not separately indicated).
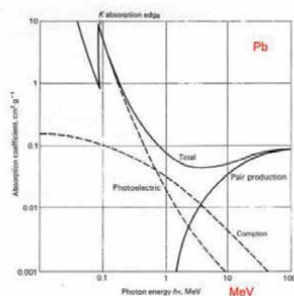
The electron/positron pairs generated in the Bethe-Heitler Process, and the Compton effect, where gamma rays push matter, are the two physical processes that are at the heart of matter/anti-matter propulsion. As will be discussed more fully below, in a matter/anti-matter spacecraft, a high-energy laser will generate electron/positron pairs in the Bethe-Heitler Process and then those pairs will separately be directed to a thruster where they will collide, annihilate, and generate gamma rays. When the gamma rays hit the inner shell of the thruster, the gamma rays will propel the spacecraft forward utilizing the Compton Effect and Newton's Third Law.

5. Theoretical background: the problems of paired-particle generation and storage

5.1 Origin of the idea of photon propulsion & theoretical follow-on

Eugen Sanger, a Bohemian-Austrian-German-French aeronautical engineer and scientist, is generally credited with proposing the idea of a photon-propelled space-craft in the late 1950s [10]. He even proposed gamma rays as a source of propulsion for rockets. At that time, laser technology was barely in its infancy, and positrons were mainly understood as cosmic rays that arrive from outer space in small numbers, or from rare radioactive decay. No mechanism for generating large quantities of positrons was conceivable.

But the idea of anti-matter annihilation as a potential propulsion source of energy for space travel persisted. The attraction of the energies generated by matter/anti-matter annihilation reactions, combined with the low mass of positrons and electrons, in light of Tsiolkovsky's equation, was too powerful. Furthermore, over the ensuing decades, laser technology, positron generation (even in low numbers, like in PET scanners), fission reactors, and magnetic containment vessels (such as for fusion experiments) were developed.

By the late 1990s and early 2000s, anti-matter propulsion became a topic of increased research and discussion [11–13]. In the United States, at least two programs were undertaken to further matter/anti-matter propulsion. At Embry-Riddle Aeronautical University (ERAU), the Hyperion Project, led by Darrel Smith and Jonathan Webb, sought to advance this form of propulsion. At the conclusion of the project, in 2007, Smith and Webb concluded that the "current state of the art technology is lacking in the areas of positron production and storage techniques for these concepts to be realized any time in the near future" [14]. The prior year, the United States' National Aeronautics and Space Administration (NASA) concluded a project at its Institute for Advanced Concepts (NIAC) exploring the possibility of anti-matter-propelled spaceships. The NIAC team, like the team at ERAU, concluded that the "technical challenge of positron production," and the challenge of "storing enough positrons in a small space," persisted as obstacles for achieving matter/anti-matter propulsion [15].

5.2 Key laboratory discoveries

The difficulties with positron generation and storage did not last long.

First, in 2008, Hui Chen and others on her team at LLNL demonstrated that large quantities of positrons could be produced by high-energy, short-burst lasers striking

high-Z (i.e., high-atomic-mass) targets [16]. Then, a few years later (beginning in 2015), the storage of electrons and positrons in an optimized dipole stellarator, by Eve Stenson and others on her team at the MPIPP, was demonstrated [3].

With these two discoveries, the primary obstacles identified by NASA and the Hyperion Project as impediments to matter/anti-matter propulsion had been overcome, at least in the laboratory. Based on these discoveries, the feasibility of matter/anti-matter propulsion for generating relativistic speeds in space was hypothesized, along with concepts for systems that could utilize Chen's and Stenson's discoveries to make matter/anti-matter propulsion practicable [17, 18].

6. Components of a matter/anti-matter spacecraft

Based on the discoveries of Chen and Stenson, the basic components of a matter/anti-matter propulsion system are fairly simple. The system will probably need four main components: a power source, a paired-particle generator, a storage system, and an annihilation chamber (or, an "interaction" chamber). Depending on the efficiency of the paired-particle generator, and the nature of the mission, it may not be necessary to have a storage system.

With a storage system, the engine would probably be ordered something like **Figure** 7, with a payload on top.

6.1 Power source

The power source for the system is probably going to be a fission-based nuclear reactor. These reactors have been used in industry and in multiple navies around the world. The reactor for space travel would be similar to the nuclear reactors used to power modern nuclear submarines. In the 1960s, nuclear reactors for propulsion systems for aircraft were developed in the United States, showing that the weight of a reactor required for a space-propulsion system should not be an impediment to success.

6.2 Paired-particle generator

The heart of the system is the paired-particle generator. Based on the work of Chen and her team, this component would require a high-energy laser and a gold (or similar) target substrate. It would also require a magnetic collection system. The magnetic system would collect the electrons and positrons generated by the laser and direct them to the storage component.

6.3 Storage system

The storage system will probably consist of twin tokamaks, one for storing electrons and one for storing positrons. A tokamak is a large magnetic container. It is shaped like a donut, and the magnets inside are also shaped like donuts. **Figure** 8 shows the basic configuration of a tokamak; the electrons or positrons would be stored as "Plasma current".

The tokamaks for a matter/anti-matter propulsion system will probably be different from the fusion tokamaks that have been produced to date. Fusion tokamaks are designed to contain very high pressures. The tokamaks for matter/anti-matter space propulsion will probably not require such high pressures, but will still require creating very high magnetic forces.
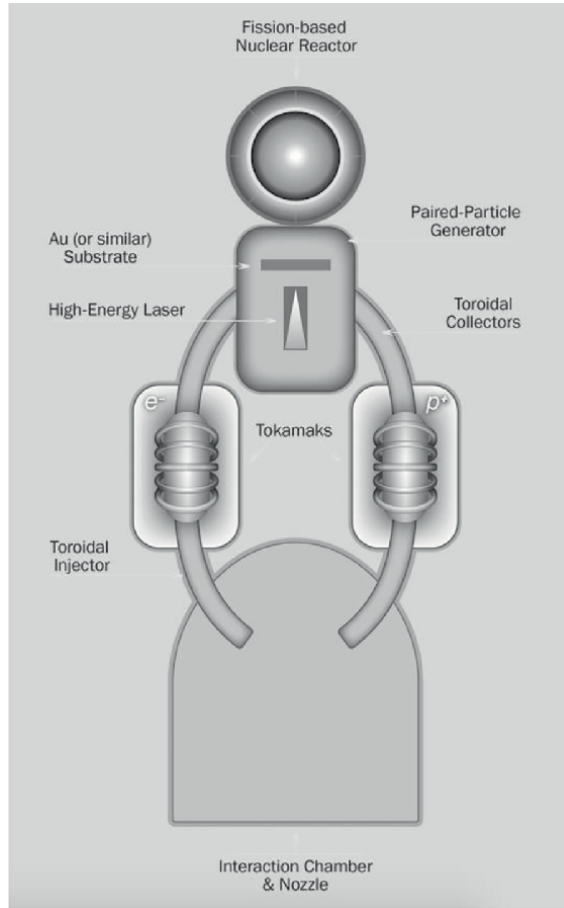
Figure 7.
System concept (courtesy Mustang Publishing).
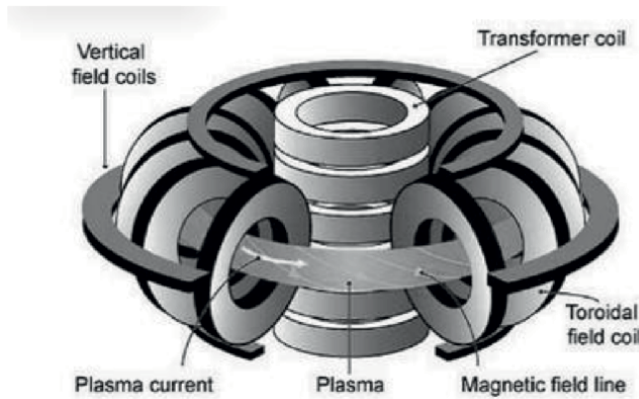
Figure 8.
Tokamak (courtesy Mustang Publishing).
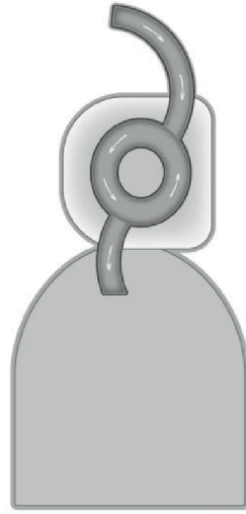
Figure 9.
Particle-flow diagram (courtesy Mustang Publishing).

Like the paired-particle generator, the twin tokamaks will require a magnetic system for directing the electrons and positrons to the annihilation chamber. In **Figure** 7, those components are called toroidal injectors.

The paired particles would flow into, and out of, the tokamaks in a pattern that is something like what is shown in **Figure 9**, with the tokamak "donut" in the middle:

6.4 Annihilation chamber

The annihilation chamber (or the "interaction chamber" in **Figures** 7 and **9**) is where the electrons and positrons will collide and annihilate. It is where the gamma rays will be produced to propel the entire spaceship.

The annihilation chamber will, at least on its inside, be somewhat bell-shaped, although probably flatter. The shape is similar to the rocket nozzles that are used on chemical rockets. **Figure 10** highlights a cutaway of the interaction chamber, where matter/anti-matter annihilation will take place.

6.5 Interstellar probes

Probes to nearby stars will probably not require a storage system. Instead, the electrons and positrons created in the generator will probably be directed immediately to the annihilation chamber, where they will annihilate and propel the craft. The highest speeds are achievable when a mission, like an unmanned interstellar mission, has a low spacecraft weight and an extended time to travel.

The annihilation chamber will also be the probes' primary tool of stearing. In order to stay on target, moveable panels in the annihilation chamber will likely asymmetrically direct the gamma-ray "exhaust" to stear the probe.
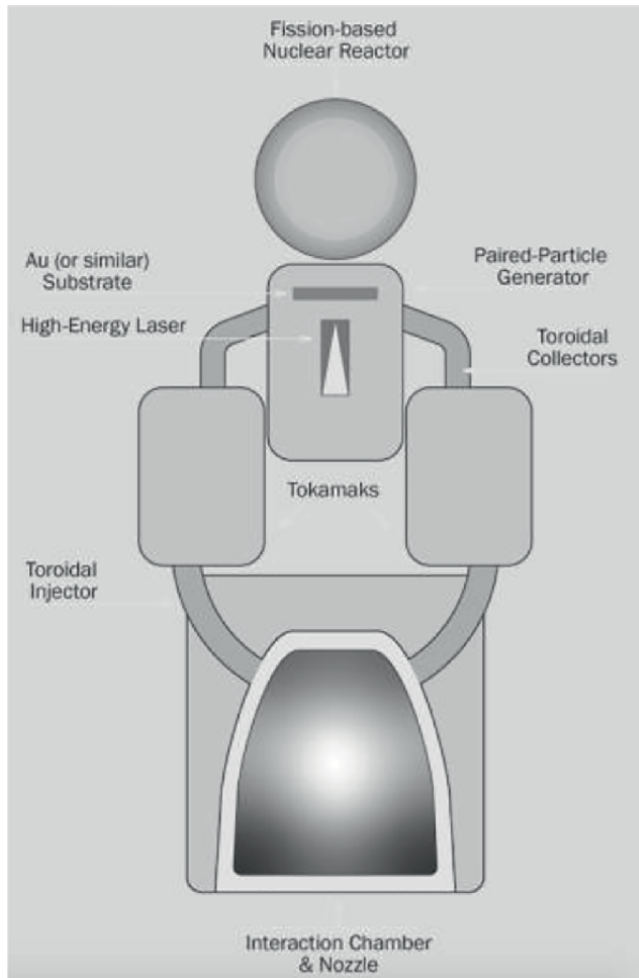
Figure 10.
Cutaway of annihilation chamber, or "interaction chamber" (courtesy Mustang Publishing).

6.6 Launch environment

The best launch environment for matter/anti-matter spacecraft is probably the Moon. With no atmosphere, the matter/anti-matter annihilations will be better controlled. The lower mass of the Moon permits faster launch acceleration. Furthermore, it is likely that chemical booster rockets will aid the initial launch of a matter/anti-matter spacecraft, in order to achieve maximum initial acceleration, somewhat like the solid-propellant rocket boosters of the United States' Space Shuttle and Artemis rocket. The United States' current Artemis Project would be well-suited to build the infrastructure and to ferry the components and materials for launch of an interstellar probe.

7. Theoretical speeds

It is possible to theorize the speeds capable of being achieved by matter/anti-matter-propelled spacecraft, based upon some reasonable assumptions involving the mass of the spacecraft and the production of paired particles by the system.

1. Some givens & approximations: (1) the hypothetical spacecraft weighs 10,000 kg; (2) an electron/positron annihilation produces 2 511-keV gamma rays; (3) the average Compton Effect force of a 511-keV gamma ray hitting an atom is approximately 200 keV [19]; (4) in the annihilation chamber, only about half of the gamma rays produced will strike the walls of the chamber, propelling the spacecraft; and (5) 100 keV = 1.6×10^{-14} N m; 100 keV = 1.6×10^{-14} kg m/s/s; 200 keV = 3.2×10^{-14} kg m/s/s.

2. Assuming that a paired-particle generator produces 6×10^{17} paired particles per second [20] (therefore producing approximately 6×10^{17} 511-keV gamma rays that will strike the annihilation chamber to propel the spacecraft, at an average of 200 keV per gamma ray), the force generated by the system is: $6 \times 10^{17} \cdot 3.2 \times 10^{-14}$ kg m/s/s $\approx 1.9 \times 10^{4}$ kg m/s/s.

3. Because the spacecraft, in this thought experiment, weighs 10,000 kg, and

$$F = ma \left(\text{Newton's Second Law} \right) \qquad (2)$$

and

$$a = F / m, \qquad (3)$$

The spacecraft will accelerate at approximately 1.9 m/s/s.

4. The formula for the velocity achieved by a constantly-accelerating object, starting at rest, is

$$v_f = at, \qquad (4)$$

where, for our purposes, by international convention, velocity (final) is measured in meters/second (direction is not relevant for this purpose), acceleration is measured by meters/second/second, and time is measured in seconds.

5. Because there are 31,536,000 seconds in a year, the speed achieved by the spacecraft hypothesized here, after 1 year, would be approximately 6×10^{7} m/s. Because the speed of light (c) is approximately 3×10^{8} m/s, the spacecraft would, after 1 year, be traveling at approximately 20% of the speed of light. After 2 years of constant acceleration, the spacecraft would be traveling at approximately 40% of the speed of light.

Mission planning would necessitate sufficient time for deceleration, but these speeds, if achievable, indicate that relativistic speeds—speeds even approaching the speed of light—are conceivable with matter/anti-matter propulsion.

8. Validation testing

Just like Tsiolkovky's equation has significance for the practical limitations of chemical rockets, the velocity equation (Eq. (4)) has great significance for the possibilities of matter/anti-matter spacecraft. Because the speeds that can be achieved by a matter/anti-matter spacecraft are a function of the number of electron/positron pairs

that can be produced, experimental determination of an optimized paired-particle generator's capacity to produce paired particles is the most logical first experimental step (in engineering terms, a "validation" step). These experiments, and follow-on experiments, should also determine whether the target substrate or the laser used are lost in some way ("burning", degradation of some sort, etc.) in the Bethe-Heitler Process, so that the potential *time* that the system can reliably operate can also be determined.

The first planned experiment to further develop this technology is an experiment to determine the specific numbers of paired particles that can be generated by a high-energy laser striking various targets. Taking advantage of a matter/anti-matter "circuit" in a custom laboratory apparatus, as well as a precision gamma-counting system designed for the task, Albireo Scientific Corporation is currently in the process of conducting this experiment, possibly under the auspices of the LaserNetUS consortium in the United States.

With this experiment, and follow-on experiments, it should be possible to determine the practical feasibility of matter/anti-matter propulsion.

9. Implications

It is reasonable to believe, based on Hui Chen's and Eve Stenson's laboratory discoveries, that matter/anti-matter propulsion is a viable—possibly the most viable—technology for achieving relativistic speeds in space. Instead of being mere science fiction, relativistic speeds are now defensible scientific theory, and they may, within a matter of a few years, become actual scientific and engineering fact.

With matter/anti-matter propulsion, the outer planets of our solar system are likely within our reach, for further scientific exploration. Most importantly, the nearest 15 stars to Earth are four to eleven light-years away [21]. At those distances, sending matter/anti-matter probes to our nearest neighboring stars, and receiving signals back from our probes, will involve a mission of only a few years. Possibly of greatest importance of all, two of the stars that are closest to us are a lot like our Sun. It would be intriguing, and potentially quite important, to find out how similar those two star systems are to our own.

10. Conclusion

When high-energy photons strike a nucleus, pairs of electrons and positrons are created. Those pairs can be separated and stored, or simply separated and re-directed, to a thruster where they can collide, annihilate, and generate 511-keV gamma rays. Those gamma rays can then strike the interior shell of the thruster and generate thrust via the Compton Effect. Depending upon the number of electron/positron pairs that can be generated in an optimized system, it is highly likely that relativistic speeds can be achieved by matter/anti-matter propulsion. The logical next step for developing this technology is a well-designed set of validation experiments. If matter/anti-matter propulsion is validated, probes to the nearest stars can be developed and launched, and their signals received, within a single human lifetime. The prospect of human interstellar travel using matter/anti-matter propulsion is now realistic and amazing.

Acknowledgements

Potential conflict of interest disclosure

The author is President of Albireo Scientific Corporation, an America corporation established to further experimental testing of matter/anti-matter propulsion.

Note

Although not directly related to the idea of matter/anti-matter propulsion, an outgrowth of this inquiry has been a novel, fundamental idea about the nature of matter and anti-matter in the Universe. In describing, and questioning, the composition of matter and anti-matter for this project, the author has hypothesized that what we understand as "matter" is actually a combination of quarks, anti-quarks, electrons, and positrons [22]. In other words, it appears possible that there is not a bifurcated distinction between all matter and all anti-matter. The initial validation experiment described here should help assess this hypothesis, in addition to helping develop matter/anti-matter space propulsion.

Regardless of the outcome of the fundamental physics inquiry pursued in this initial experiment, the prospects for matter/anti-matter propulsion will remain promising. In addition, better understanding of the components and energies within atomic nuclei may inspire technologies for space propulsion that will prove to be superior to matter/anti-matter propulsion.

Author details

Mark Pickrell
Albireo Scientific Corporation, Vanderbilt University, Nashville, Tennessee,
United States

*Address all correspondence to: mark.pickrell@albireoscientific.net

IntechOpen

References

[1] Tsiolkovsky K. The exploration of cosmic space by means of reaction devices. The Science Review. 1903;**5**(1)

[2] Lawrence Livermore Laboratory News. Billions and Billions of Particles of Anti-matter Created in Laboratory. 2008. Available from: https://www.llnl.gov/news/billions-and-billions-particles-anti-matter. [Accessed: April 5, 2020]

[3] Max Planck Institute for Plasmaphysick. Electrons and Positrons in an Optimized Stellarator. 2020. Available from: https://www.ipp.mpg.de/4793936/nwg-19. [Accessed: April 6, 2020]

[4] Turner MJL. Principles of Rocket Propulsion. Chichester, United Kingdom: Praxis Publishing Limited; 2006. p. 15

[5] Sodickson L et al. Single-quantum annihilation of positrons. Physical Review. 1851;**124**(6):1970

[6] Thomson W. The Wave Theory of Light. New York: P.F. Collier & Son; 1910

[7] Compton AH. Recoil of electrons from scattered x-rays. Nature. 1923;**112**:435

[8] Hill WT, Roso L. Probing the quantum vacuum with petawatt lasers. Journal of Physics Conference Series. 2017;**869**:012015

[9] Thioye M. Topics in the Measurement of Electrons with the ATLAS Detector at the LHC. New York: Stony Brook University; 2008. p. 69

[10] Bohn W. Propulsion by light: A tribute to the German pioneer Eugen Sanger. In: Proceedings of the SPIE -- The International Society for Optical Engineering; 25-30 April 2004; Taos, New Mexico, USA. Bellingham, Washington: Society of Photographic Instrumentation Engineers; DOI: 10.117/12.548453

[11] Smith D, Webb J. The Antimatter Photon Drive: A Relativistic Propulsion System. AIAA Paper 2001-3231; Washington, D.C.: American Institute of Aeronautics and Astronautics; 2001. DOI: 10.2514/6.2001-3231

[12] Deutsch C. Fusion reactions and matter-antimatter annihilation for space propulsion. Laser and Particle Beams. 2006;**24**(04):605-616. DOI: 10.1017/S0263034606060691

[13] Vulpetter G, Pecchioli M. Considerations about the specific impulse of an antimatter-based thermal engine. Journal of Propulsion and Power. 1989;**5**(5):591-595. See also Keane R, Zhang W-M. Reconsideration of propulsion by antimatter. Journal of Propulsion and Power 2011;**27**(5). DOI: 10.2514/1.B34140

[14] Webb J et al. Project hyperion, exotic propulsion research at Embry-Riddle Aeronautical University. AIAA 2007-5603. In: Proceedings of the 43rd AIAA/ASME/SAE/ASEE Joint Propulsion Conference; July 8-11, 2007. Cincinnati, Ohio. Washington, D.C.: American Institute of Aeronautics and Astronautics; DOI: 10.2514/6.2007-5603

[15] Steigerwald B. New and Improved Antimatter Spaceship for Mars Missions. 2006. Available from: https://www.nasa.gov/exploration/home/antimatter_spaceship. [Accessed: January 20, 2023]

[16] Chen H et al. Relativistic positron creation using ultraintense short burst lasers. Physical Review Letters. 2009;**102**(1):105001-105004. DOI: 10.1103/PhysRevLett.102.105001

[17] Pickrell M. Feasibility of a matter/anti-matter propulsion system for generation of relativistic speeds in space. Journal of Space Exploration. 2020;**9**(2):162-167. DOI: 10.21767/2319-9822.1000162

[18] Pickrell M. Humanity's Greatest Leap: The Science and Technology Behind Feasible Interstellar Space Travel. Nashville, Tennessee: Mustang Publishing; 2021

[19] Compton AH. A quantum theory of the scattering of x-rays by light elements. Physical Review. 1923;**21**(5):483-502. DOI: 10.1103/PhysRev.21.483

[20] By comparison, the TRIUMF cyclotron ejects 6 x 10^{14} particles/second. Alberding, N. SFU Physics 121: Optics, Electricity & Magnetism. Spring 2010. Available from: http://www.sfu.ca/phys/121/1101/lectures/lecture32.pdf. [Accessed: September 9, 2021]

[21] Muirden J. Astronomy Handbook. New York: Arco Publishing, Inc.; 1982

[22] Pickrell M. Hypothesis for a universal matter/anti-matter hadron structure, with resulting cosmology. HAL 03475258. 2021. (working paper)

Section 2

Marine Propulsion

Optimised PVDF Placement Inside an Operating Hydrodynamic Thrust Bearing

Andrew Youssef, David Matthews, Andrew Guzzomi and Jie Pan

Abstract

In our previous work we demonstrated the feasibility of using Polyvinylidene Fluoride (PVDF) sensors inside an operational thrust bearing and were able to measure the blade passing frequencies (BPF) due to an asymmetric flow around different propellers. In that work however the sensors were positioned inside the flat surface of the stationary portion of the bearing with the tilted pads rotated on the opposite side. Due to this configuration the output signal of the PVDF consisted of a superposition of the pad passing frequency (PPF) and the blade passing frequency (BPF) making it difficult to extract useful information from the results. Here, an improved bearing pad-film configuration is proposed in order to minimise the effects of the PPF. By embedding the films inside the pads, positioned on the stationary side of bearing, and rotating the flat surface, it was possible to eliminate the PPF and significantly increase the signal to noise ratio. The measured results give a better understanding of the fundamental vibratory components that arise from the propeller-shaft system.

Keywords: PVDF, monitoring, thrust bearing, force transducer, marine vessels, piezoelectric sensor

1. Introduction

Most marine vessels have propellers at the stern operating in non-linear wakes. This propeller placement is done primarily for ease of construction and propulsion efficiency. The main disadvantage of such a setup is having to operate in a region where the wake is non-linear. This generates noise from an oscillating thrust and, in terms of hull induced vibrations at frequencies below 100 Hz [1], can have large effects on passenger comfort, mechanical wear and acoustic detection. Developing an accurate vibrational model of the propulsion system in a non-uniform wake is extremely difficult. It is necessary to have a good understanding of the hydrodynamic forces inside the thrust bearing and measuring this force is logistically difficult. This is due to the complex nature of thrust bearings which self stabilise based on operating parameters such as speed and load [2]. To simplify the inclusion of thrust bearing stiffness in analytical modelling, simple linear stiffness representations are used
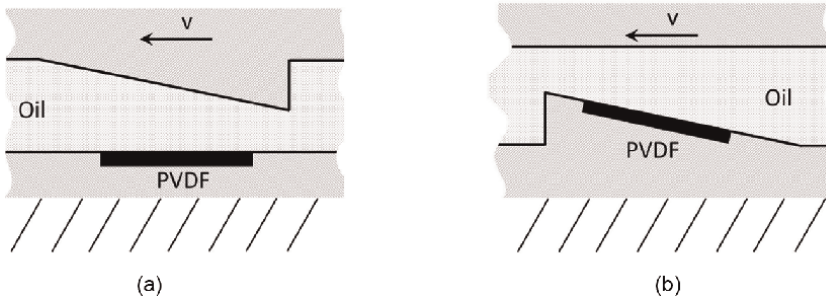
Figure 1.
The arrangement of the PVDF film within the thrust bearing in our previous work [8] (a) and in this work (b). In both arrangements the PVDF is embedded on the stationary body and 'v' indicates rotational direction of the rotating body.

[1, 3, 4], however these are limited as it has been shown that due to large perturbations of the oil film thickness, a nonlinear response is required [5–7]. Therefore measuring the internal hydrodynamic forces inside the thrust bearing is ideal. This paper attempts to address this problem by using intrinsic piezoelectric sensors installed inside the thrust bearing itself. Conventionally this would be done with accelerometers however their physical properties make them unsuitable for use inside a moving bearing. Another option is the use of thin piezoelectric polymer film such as PVDF (Polyvinylidene Fluoride).

In our previous paper [8], an in-depth review of the use of PVDF to measure dynamic forces in static structures [4, 9–16] was discussed. It was noted that PVDF cannot measure absolute pressures, only the fluctuations, which is a common use of PVDF in fluids [17–22], due to its piezoelectric properties [23, 24]. The paper reported on the use of PVDF inside a thrust bearing to measure the pressure fluctuations and infer the change in contact force. Due to limitations in the experimental design, namely the placement of the PVDF films in relation to the pads on the rotating body, the signatures captured from the PVDF films were heavily influenced by the Pad Passing Frequency (PPF). Hence, although that study found that the sensors could measure the pressure fluctuations generated by the sliding pads, the true nature of the excitation of interest, the BPF was masked.

Here, the design of the experiment was reworked so that the true excitation force from the propeller and the resulting change in contact force within the bearing could be observed without the influence of the PPF. This was achieved by placing the PVDF in the tilted portion on the stationary body.

The previous configuration (**Figure 1a**), resulted in the pressure profile generated by the pad sliding over the PVDF film. This led to the dynamic pressure fluctuations being subjected to the PVDF from the pad motion relative to the PVDF sensor. The new configuration proposed in this study (b) removes this component and results in the PVDF film being subjected to the dynamic fluctuations arising from the shaft axial load and hence propeller. The static component of the pad's pressure profile cannot be observed in the signature as a result of the intrinsic nature of PVDF.

2. Materials and methods

The original rig [8], shown in **Figure 2**, is used here and its main attributes described here for completeness. It was designed to model a typical propulsion system
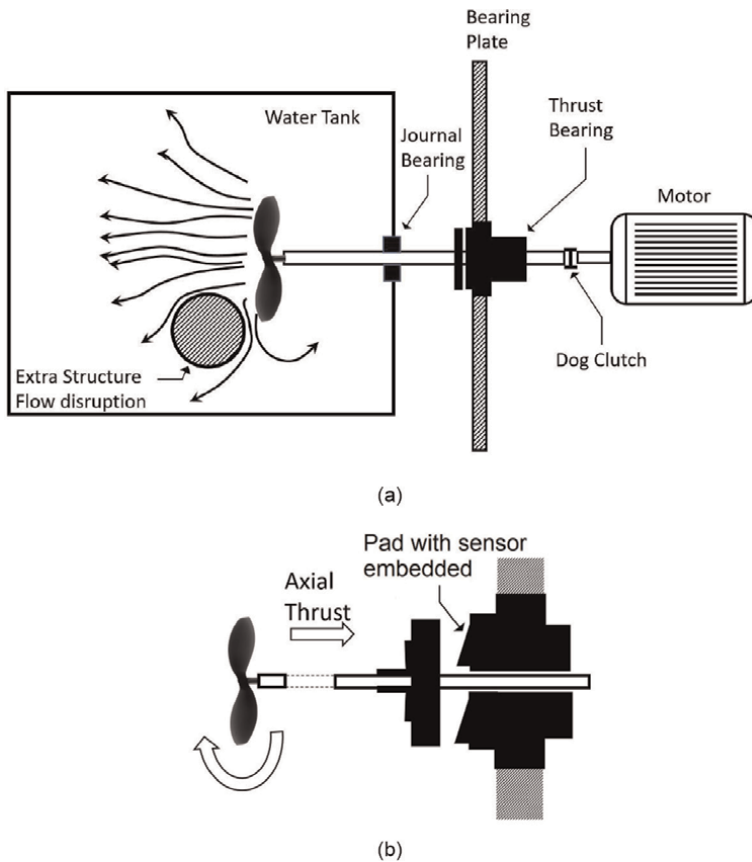
Figure 2.
Schematics of the experimental set-up: (a) layout of entire physical system; (b) enlarged view of propulsion system.

used in marine settings. The system consists of a propeller (prop), shaft, journal bearings, and a thrust bearing attached to a supporting plate structure which represents the hull. The propeller provides axial thrust to the shaft which is transmitted to the hull (supporting plate) via the thrust bearing. The coupling, known as the "dog clutch", is rigid in torsion but flexible in bending thus allowing axial motion to be transmitted along the "floating" shaft. This helps to isolate any unwanted vibration from the motor. The 10 mm thick, 1500 mm wide supporting steel plate is fixed to a concrete block to take the thrust load generated by the propeller and also supports the motor as shown.

A two-blade and three-blade propeller of equal diameter (0.22 m), shown in **Figure 3**, were separately coupled to the propulsion system in the water tank (0.99×0.59×0.58 m) to observe different blade passing forces. A larger (diam = 0.3 m) alternative style bronze two-blade propeller was also used (**Figure 3**).

In addition to the four test configurations (No prop = NP, standard two-blade prop = TBP, bronze two-blade prop = TBBP and three-blade prop = ThBP), two PVDF arrangements were investigated with these test configurations. For each case, the non-rotating component into which the PVDF was embedded was constructed out of ABS (Acrylonitrile Butadiene Styrene) using a 3D printer. Since the forces, temperatures and operating times were relatively low, it was presumed that using the plastic
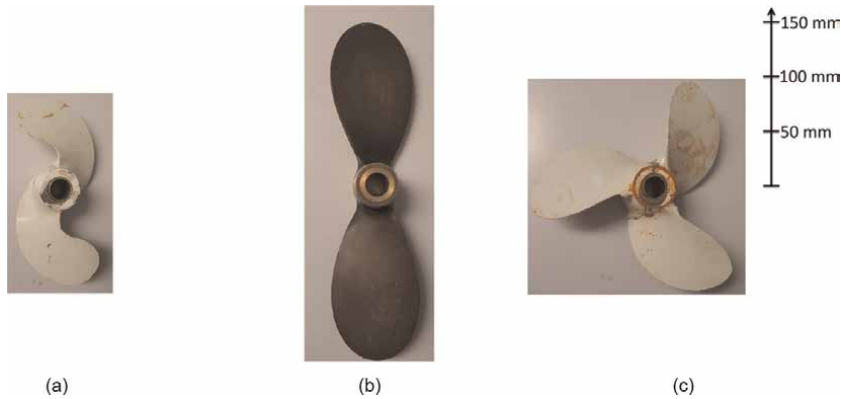
Figure 3.
Propellers used in the experiment: (a) standard two-blade; (b) bronze two-blade; and, (c) three-blade.

material inside a functioning, small-scale, thrust bearing would not be a problem. This was confirmed by our previous study [8].

Two different designs were investigated regarding the placement of the PVDF: Case 1 - the stationary component was a plain washer with the thrust washer in the rotating component sliding over top as in our first study [8]; Case 2 - was arranged such that the stationary component had the thrust washer and the PVDF embedded on top, with a plain washer in the rotating component sliding over top. Both arrangements (cases) had the PVDF fixed to the non-rotating body to permit the signals to be measured without the need for telemetry or slip rings (**Figure 4**).

In Case 1, (**Figure 4**), where the stationary component was the plain washer, recesses were made in the washer to insert two PVDF films as shown. Opposite the plain washer, a thrust washer, also constructed out of ABS, was used with two pads angled at two degrees to the surface. In Case 2, in **Figure 4**, the thrust washer was printed with two, two-degree tilted pads and the PVDF film was embedded into the tilted portion of the washer. Opposite the thrust washer, a plain washer was used in the rotating component. This configuration better resembles what is seen in a typical thrust bearing in a marine propulsion system.

The PVDF sensors were cut from a sheet of 110 μm thick film obtained from Measurement Specialties. Contacts were made using conductive copper tape on the electrodes and the films were glued using West Systems 105 epoxy resin inside the two recesses in the plastic washer. The PVDF sensors were protected by covering the interacting surface of the washer with a thin layer of epoxy. Heat from a blow torch was briefly applied to the epoxy overlaying the PVDF sensors to remove any small bubbles in the thin layer before it was left to cure. Connectors were then added to the end of the cables from the PVDF sensors such that they could be operated independently.

A Brüel & Kjaer (B&K) 2635 charge amplifier was used to condition the signal from the PVDF film. In conjunction with the B&K Pulse Time Data Recorder software, a B&K LAN-XI data acquisition system (Type 3050-B-060) was used to analyse and collect data in the time domain from the PVDF. At a sampling rate of 16,384 Hz, any higher frequency noise from the sensors would be collected while retaining manageable file sizes.

The data was post-processed using Matlab. The raw voltage measured from the PVDF film were converted to force via the measured calibration factor as discussed in
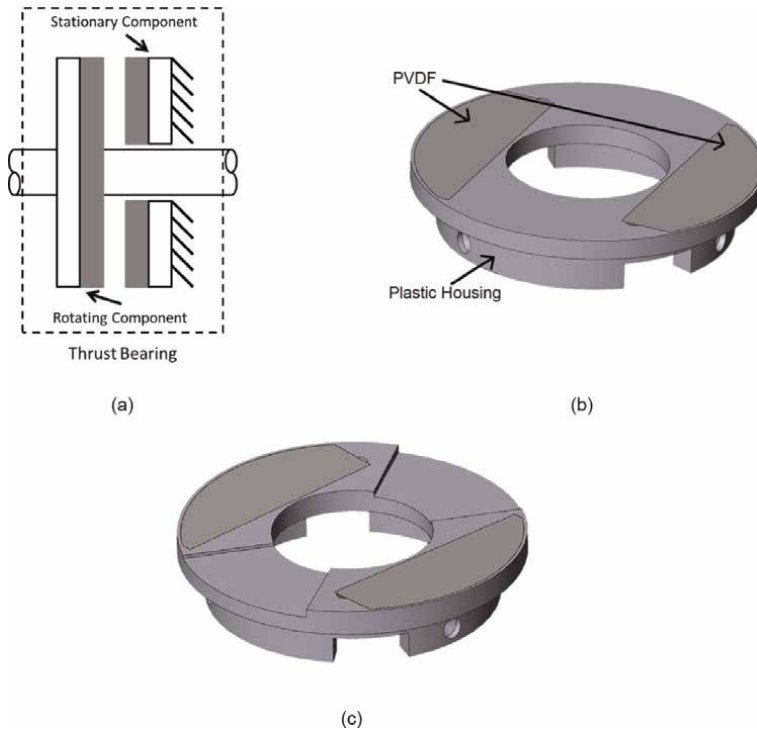
Figure 4.
Thrust bearing comprising stationary and rotation components (a). Stationary bearing configuration: Case 1 - PVDF embedded in plain washer (b) and Case 2 - PVDF embedded in thrust washer (c).

our previous papers [8, 25]. Although no physical trigger was implemented in the experimental setup, the time domain signals were aligned using Matlab's "alignsignals" function. The frequency-domain data was obtained using the inbuilt FFT function by dividing each track into 8 equal segments to obtain a better frequency representation of each time-domain signal. Each segment was windowed with a Hamming window, with 50% overlap to reduce the effect of windowing.

The set-up enabled the prop shaft to be spun in different configurations. The first being with no propeller at the end of the shaft to give a representation of the noise transmitted to the sensors from just the shaft spinning. Then, three different propellers were attached to the shaft in turn and rotated at speeds of 0 to 600 RPM in 20 RPM increments. Each configuration was performed for both Case 1's and 2's design.

3. Results and discussion

Figures 5 and **6a** shows the results with Case 1 bearing arrangement at 500 RPM for each of the three aforementioned propellers. The features seen here are representative of what is discussed in our previous paper [8]. **Figures 5** and **6b** show the result when the bearing design of Case 1 (**Figure 4**) is replaced with Case 2 (**Figure 4**). The result pertains to the force from one of the embedded sensors at 500 RPM, the other channel shows similar trends. In this arrangement, the sensor signature is dominated by the blade passing effects.
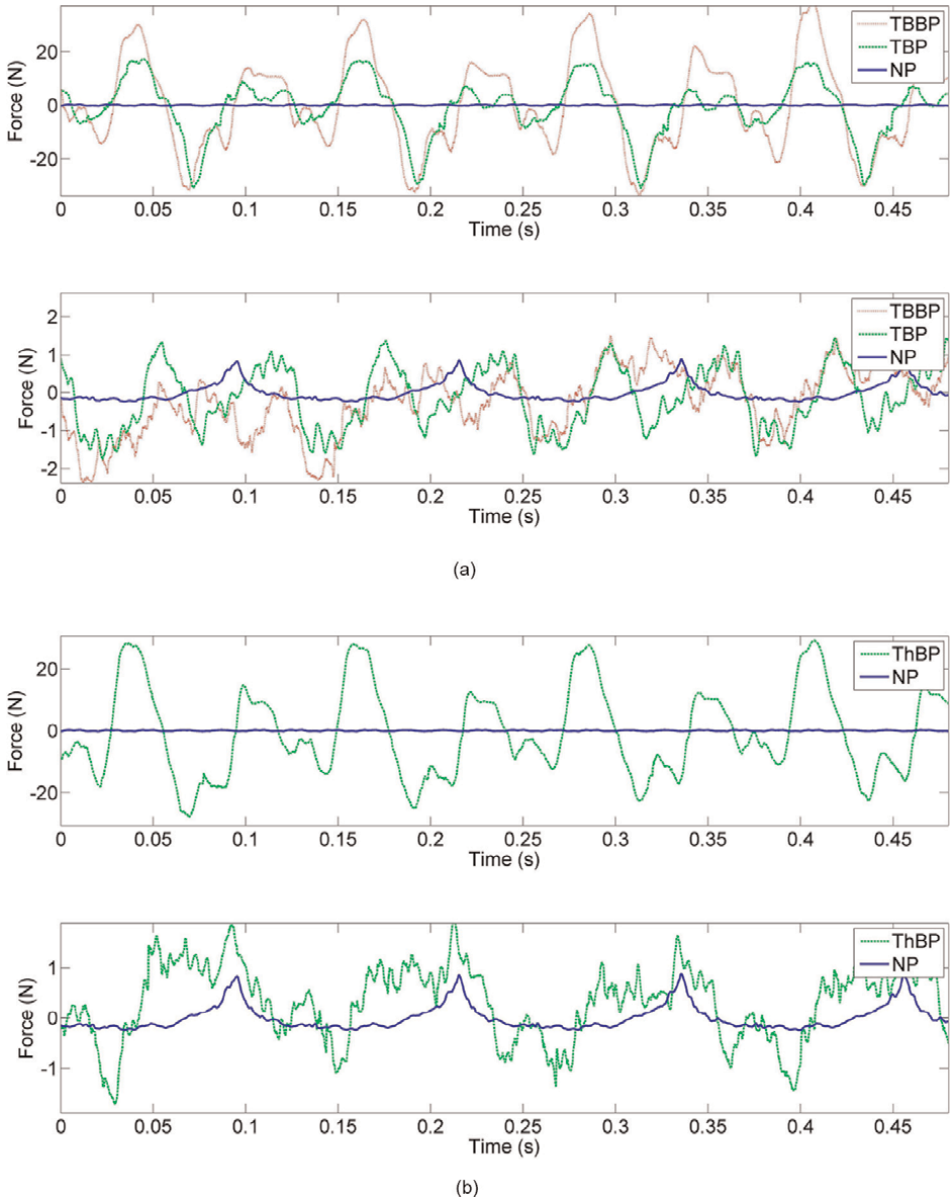
Figure 5.
Time data of the captured dynamic force from the PVDF with Case 1's design (a) and Case 2's design (b). The two (TBP), bronze two (TBBP) and three (ThBP) blade propeller is spun at 500 RPM when compared to no propeller (NP).

The time-domain signatures in **Figure 5** is difficult to interpret due to superposition of the frequency components contained in the signal, however, it can be seen that the propeller force varies approximately ±2 N in Case 2's result. This change in propeller force is similar in magnitude for the three propeller types. In addition to this, the plain shaft exhibits a large signature at the shaft rate, which is attributed to the shaft rotating in the journal bearing which is coupled to the PVDF film via the thrust bearing.

It can be seen in the frequency domain of **Figure 6** that the most significant peak after the shaft rate $\left(A_{f1\ Case\,2}\right)$ is the second harmonic $\left(A_{f2\ Case\,2}\right)$ for the
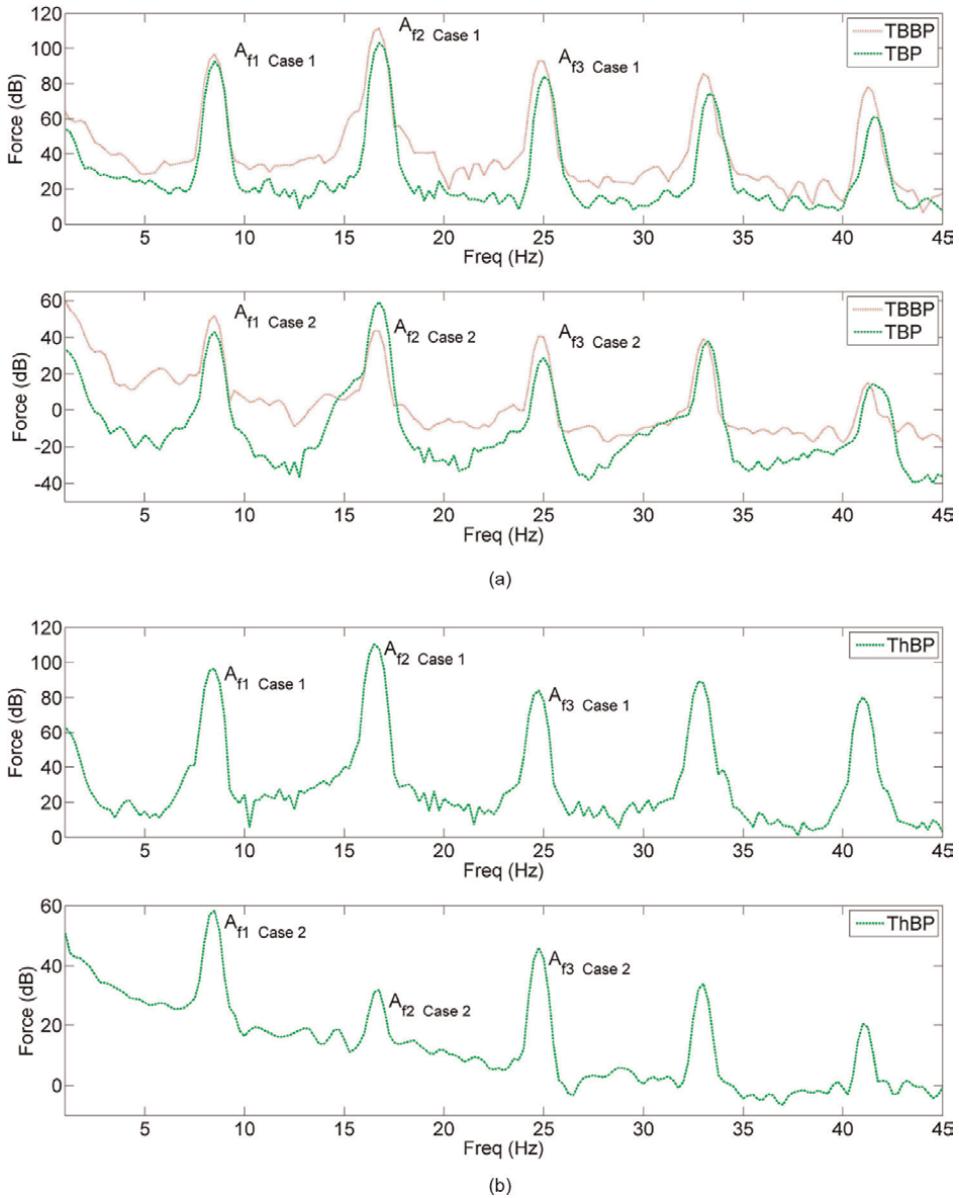
Figure 6.
Frequency data of the captured dynamic force from the PVDF with Case 1's design (a) and Case 2's design (b). The two (TBP), bronze two (TBBP) and three (ThBP) blade propeller is spun at 500 RPM when compared to no propeller used (NP).

two-blade result and the third harmonic $\left(A_{f3\ Case\ 2}\right)$ for the three-blade propeller, these correspond to the respective BPFs. The effect of the PPF is eliminated as $A_{f2\ Case\ 2} << A_{f3\ Case\ 2}$ with reference to the three-blade result; the improvement is less apparent if considering just the form without accounting for the amplitude regarding the two-blade data as the PPF and BBF are superimposed for these arrangements involving a bearing comprising 2 pads and propellers with 2 blades. This is in contrast to when the PVDF is embedded as in Case 1's design. No matter which propeller is

used, the second harmonic of the shaft rate is the most significant,
$A_{f2 \text{ Case } 1} > A_{f3 \text{ Case } 1}$, due to the two pads sliding over the PVDF film. This artefact is a by-product of the set-up and confounds the true nature of the propeller excitation forces, as revealed in **Figures 5** and **6** (L2, L4).

These trends can be further demonstrated across all test speeds, and more clearly depicted in the frequency domain (**Figure 7**). For the plots shown on the left in **Figure** 7, 10 s of measured data was recorded for each rotational speed tested. The 10 s records were stitched together to produce a spectrogram. For clarity, only the three blade propeller (ThBP) results are shown (similar results were observed for the two blade propeller variants). The spectrogram amplitudes along the second and third harmonics have been extracted and are shown in **Figure** 7 and denoted by A_{f2} and A_{f3}, respectively. This method of data representation clearly evidences that the second harmonic is typically lower or much closer to the third harmonic for the Case 2 arrangement compared to the Case 1 arrangement.

With reference to the Case 1 results depicted in **Figure 7a**, a bifurcation is observed about a 50 Hz centre frequency. (This phenomenon was also observed for the TBP tests not shown here). The bifurcation was not observed in any of the Case 2 tests. The 50 Hz centre frequency is attributed to background Australian supply voltage EMF. The bifurcation is believed to result from the superposition of the strain in the PVDF arising from the hydrodynamic force which moves with rotational speed and the strain caused in the PVDF as a result of it being subjected to the external field. Further investigation is required to understand this phenomenon.

The proposed PVDF arrangement of Case 2 can also be compared to the initial PVDF bearing pressure measurement investigation presented by the authors [25]. In that work the PVDF was embedded in the flat base of the thrust bearing similar to Case 1's configuration presented herein. The vertical test rig arrangement [25] facilitated different rotational speed and different fixed bearing gap investigations in the absence of a fluid immersed propeller. **Figure 8** shows 300 RPM data from that study processed into the frequency domain and compares the result to that of the current study for the Cases 1 and 2 arrangements for the same speed with no propeller (NP). As the sensitivities of the sensors vary, the data has been normalised to the shaft rate. There are two attributes: (1) that the second harmonic is reduced when compared with the original study; (2) that the noise floor is reduced across all frequencies, that warrant more detailed explanation. Firstly, the results obtained by [25] and Case 1 here show an increase in the second harmonic of the shaft rate when compared to newly proposed Case 2 arrangement. The larger amplitude pertaining to the original [25] study compared to Case 1 here is attributed to the increased pressure formed under the tilted pad as a result of the original set-up which forced a fixed film thickness whereas in the current study the bearing can adjust the film thickness to achieve force equilibrium. Secondly, and of potentially greater importance, is that the noise floor across all speeds has been reduced significantly using the Case 2 arrangement. It is thought that this can be attributed again to the new arrangement's reference frame. Specifically, that unlike the arrangements that have the pad moving passed the PVDF, because the PVDF films are mounted on the pads in Case 2 then they effectively experience the cleaner established pressure field above the pad and are not as influenced by the frequency content contained in the upstream and downstream flow and eddies [25] on each side of the pad. Whilst further experimental and numerical work is underway, these results add credence to the utility of the new arrangement.
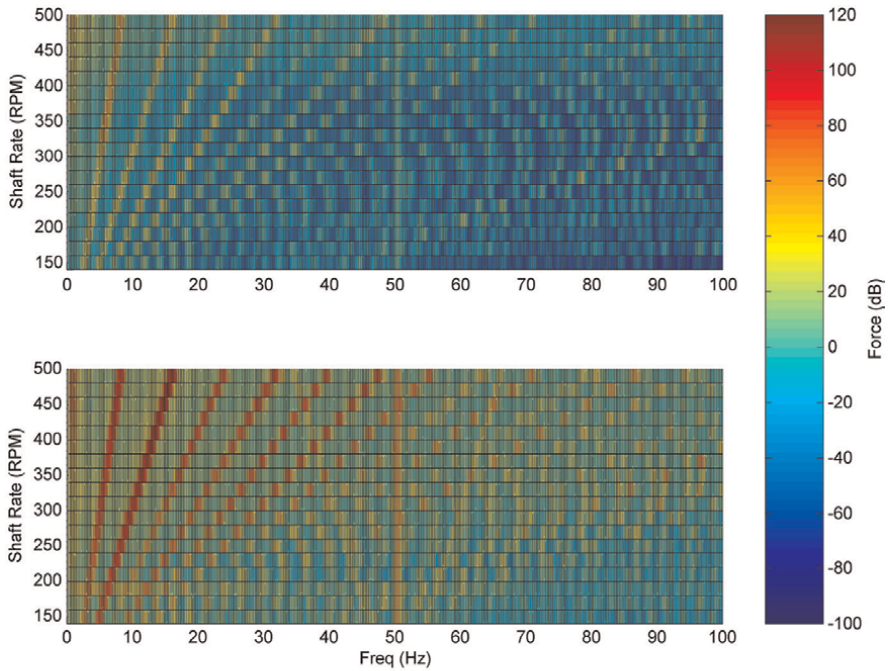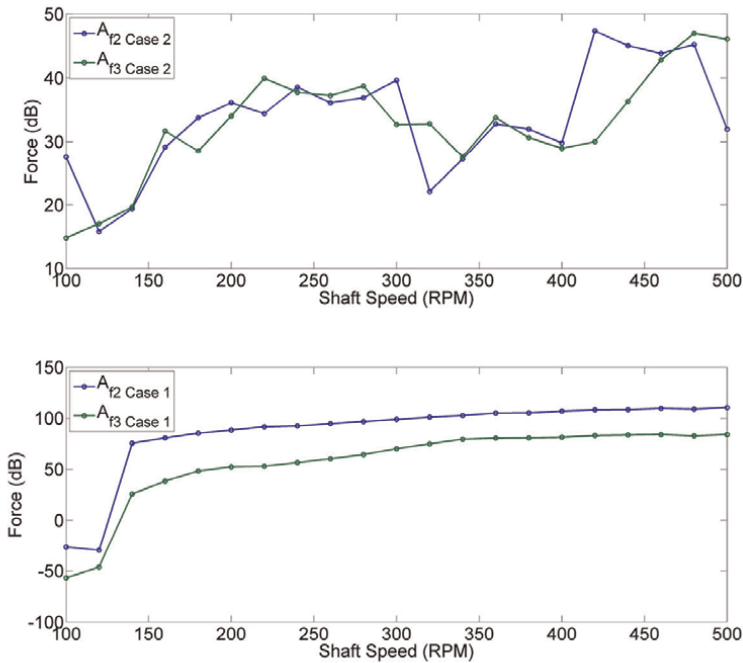
Figure 7.
The frequency response of the PVDF sensors across all test speeds for the Case 2's arrangement and Case 1's arrangement (a) with the three-blade propeller (ThBP). The magnitudes at the second and third harmonics are shown in (b) for both test cases.
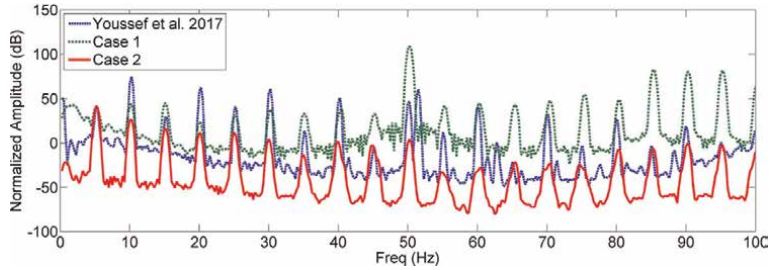
Figure 8.
Comparison of the [25] frequency content to that of Cases 1 and 2 at 300 RPM with no propeller.

4. Summary

The focus of the paper is to evidence differences between results from PVDF sensors when they are placed within different surfaces of the thrust bearing. In particular, the pad passing frequency (PPF) was discovered when the rotating pads act across the surface of the sensors. Also observed was an increase in broadband noise associated with fluid motion generated by the rotating pads. Both of those observations are important for the measurement of the interaction force within a thrust bearing. The PVDF placement on the pad, on the other hand, provides signals free from the pad passing and broadband signals as a result of the changed reference frame. This significant reduction in the noise floor across the full frequency of rotational speeds tested is achieved without post processing filtering. Despite its promise, this latter configuration of the PVDF placement is by no means to be the optimal placement, as the interpretation of the PVDF output in terms of the force components on its surface and the dynamic response of the structure upon which the sensor is attached still require more sophisticated experimental and modelling work.

Conflict of interest

The authors declare no conflict of interest.

Author details

Andrew Youssef[*][†], David Matthews[†], Andrew Guzzomi[†] and Jie Pan[†]
School of Engineering, The University of Western Australia, Perth, Australia

*Address all correspondence to: andrewyoussef22@gmail.com

† These authors contributed equally.

IntechOpen

References

[1] Dylejko PG, Kessissoglou NJ, Tso Y, Norwood CJ. Optimisation of a resonance changer to minimise the vibration transmission in marine vessels. Journal of Sound and Vibration. 2007; **300**(1):101-116

[2] Kingsbury A. Development of the Kingsbury thrust bearing. Mechanical Engineering. 1950;**172**:957-962

[3] Sawicki JT, Rao TVVLN. A nonlinear model for prediction of dynamic coefficients in a hydrodynamic journal bearing. International Journal of Rotating Machinery. 2004;**10**(6): 507-513

[4] Lee I, Sung HJ. Development of an array of pressure sensors with PVDF film. Experiments in Fluids. 1999;**26**(1): 27-35

[5] Pan J, Farag N, Lin T, Juniper R. Propeller induced structural vibration through the thrust bearing. In: Proceedings of the Annual Conference of the Australian Acoustical Society. Adelaide, Australia; 2002. pp. 13-15

[6] Parkins DW, Horner D. Tilting pad journal bearings—Measured and predicted stiffness coefficients. Tribology Transactions. 1993;**36**(3): 359-366

[7] Zhang S, Zhang Q. Coupled torsional and axial nonlinear vibration model of the crankshaft with a propeller. In: 2008 Asia Simulation Conference 7th International Conference on System Simulation and Scientific Computing. Beijing, China: IEEE; 2008. pp. 668-674

[8] Youssef A, Matthews D, Guzzomi A, Pan J. Contact force measurement in an operational thrust bearing using PVDF

film at the blade and pad passing frequencies. Sensors. 2018;**18**(11):3956

[9] Sahaya Grinspan A, Gnanamoorthy R. Impact force of low velocity liquid droplets measured using piezoelectric PVDF film. Colloids and Surfaces A: Physicochemical and Engineering Aspects. 2010;**356**(1):162-168

[10] Kim J, Park Y, Choi I, Kang D. Development of smart elastomeric bearing equipped with PVDF polymer film for monitoring vertical load through the support. VDI Berichte. 2002;**1685**: 135-140

[11] Mahale BP, Bodas D, Gangal SA. Development of PVDF based pressure sensor for low pressure application. In: Nano/Micro Engineered and Molecular Systems (NEMS), 2011 IEEE International Conference on. Kaohsiung, Taiwan: IEEE; 2011. pp. 658-661

[12] Nash BT. Pressure mapping using PVDF film. The UNSW Canberra at ADFA Journal of Undergraduate Engineering Research (Canberra, ACT, Australia). 2012;**4**(1):2-16

[13] Shirinov AV, Schomburg WK. Pressure sensor from a PVDF film. Sensors and Actuators A: Physical. 2008; **142**(1):48-55

[14] Talbot JP. On the performance of base-isolated buildings: A generic model. [PhD thesis], University of Cambridge. 2002

[15] Tiwari R, Lees AW, Friswell MI. Identification of dynamic bearing parameters: A review. Shock and Vibration Digest. 2004;**36**(2):99-124

[16] Zhang J, Wang Y. On the design of intelligent insoles using PVDF film. In:

Piezoelectricity, Acoustic Waves, and Device Applications (SPAWDA), 2016 Symposium on. Xi'an, China: IEEE; 2016. pp. 193-196

[17] Huiliang G, Zuoyong H, Wenjun Y. The self-noise response of a large-planar PVDF hydrophone to turbulent boundary layer pressure fluctuation. Acta Acustica. 1999:02

[18] Li Q, Xing J, Shang D, Wang Y. A flow velocity measurement method based on a PVDF piezoelectric sensor. Sensors. 2019;**19**(7):1657

[19] Zimo L, Dorantes-Gonzalez DJ, Chen K, Yang F, Jin B, Li Y, et al. A four-quadrant PVDF transducer for surface acoustic wave detection. Sensors. 2012;**12**(8):10500-10510

[20] Van Tol D, Jack Hughes W. Underwater PVDF acoustic intensity probe. The Journal of the Acoustical Society of America. 1993;**93**(4): 2273-2273

[21] Wang Y-C, Huang C-H, Lee Y-C, Tsai H-H. Development of a PVDF sensor array for measurement of the impulsive pressure generated by cavitation bubble collapse. Experiments in Fluids. 2006;**41**(3):365-373

[22] Ren-shu YUAN, Shi-qun SUI. Dynamic response of PVDF thin film under pulse pressure. Instrument Technique and Sensor. 2011;**1**(8)

[23] Gusarov B, Gusarova E, Viala B, Gimeno L, Cugat O. PVDF piezoelectric voltage coefficient in situ measurements as a function of applied stress. Journal of Applied Polymer Science. 2016;**133**(14): APP.43248

[24] Kawai H. The piezoelectricity of poly (vinylidene fluoride). Japanese Journal of Applied Physics. 1969;**8**(7):975

[25] Youssef A, Matthews D, Guzzomi A, Pan J. Measurement of pressure fluctuations inside a model thrust bearing using PVDF sensors. Sensors. 2017;**17**(4):878

Section 3

Train Propulsion

Chapter 5

Developing a Novel Superstructure System for the Ballasted Railways Using RRP$_{235special}$ Stabilized Clayey Soil

Hossein Ghorbani Dolama

Abstract

The ballasted tracks have been considered due to their benefits such as low construction cost, simple technology, good performance in vibration, and proper drainage. Despite the advantages, low bearing capacity, time-consuming maintenance, low vertical stiffness, vertical and horizontal displacement, and ballast problems are the reasons for the scientist's effort to enhance the track using different methods. The problems increase in the presence of clay. The Royal Road Product 235 Special (RRP$_{235Special}$) have used in road construction since 1960s. In this regard, all the layers underneath the sleeper have been replaced with the clayey subgrade stabilized with RRP$_{235Special}$. A series of static and dynamic lab tests with different additive dosages were carried out to investigate the stabilized soil properties, and an optimal percentage was found. The sample with $0.15 \, lit/m^3$ RRP$_{235Special}$ was determined as the suitable dosage for lab experiments. According to the lab experiment results, a track was constructed in Urmia railway station, and field tests such as single tie push test (STPT) and plate loading test (PLT) were carried out. The conventional system is compared to the proposed superstructure. As a result, STPT has no significant difference, and PLT was increased due to the use of RRP$_{235special}$.

Keywords: RRP$_{235Special}$, soil stabilization, ballast box test, track damping, track stiffness, track settlement, STPT, PLT

1. Introduction

The traditional ballasted tracks have been used widely in railway transportation infrastructure. These tracks have been investigated in two views in terms of civil engineering, layers underneath the ballast layer (subgrade) and the ballast layer (pavement). Facing clayey soils in the subgrade of railway tracks reduces the bearing capacity, increases water absorption, and as a result, creates horizontal and vertical deformations that are transmitted through the ballast layer to the railway pavement. Construction of ballasted tracks on the clayey soft subgrade causes high settlement and low bearing capacity. In addition, significant maintenance costs and

time-consuming operations have been encountered due to the presence of clay. Despite the ballast layer advantages in low construction cost and time, proper drainage, simple technology, and proper damping, it has some disadvantages such as vertical and horizontal displacement, low vertical stiffness, need for time-consuming and expensive maintenance operation, low lateral resistance, slippage, pumping, dirty ballast, ballast breakage and flying ballast in high-speed railways. In this regard, many researches have been done to manage these drawbacks.

It will be a caught-in-crossfire situation when structures fail due to the presence of clayey soils and the need for their microstructural, mechanical, and strengthening properties to be improved before construction.

A huge amount of suitable material and enormous costs is needed in transportation projects. Thus different stabilizing methods have been considered by scientists [1].

Clayey soft soil can damage the transportation infrastructure due to its disadvantages such as low strength and huge volumetric changes that generate expensive maintenance costs [2, 3].

The subgrade of railway track is an important part that cans cause increased maintenance costs [4].

Facing soft subgrade causes a challenge in railway track design. The long-term behavior of soft subgrade under repeated load is important in track design [5].

Extensive costs and structural damages generate in clayey soil due to volumetric change arising from wet-dry conditions [6].

Cement and lime-stabilized subgrade soils are considered environmentally unfriendly. So, as a solution Sodium Alginate Biopolymer have used in pavement construction. The results show an increase in resilient modulus, stiffness and strength depending on the material type and concentration and curing time [7].

Lime-Microsilica has been used as a silty soil stabilizer in the railway subgrade to improve California Bearing Ratio (CBR). The results show an increase due to the use of additives [8].

The railway subgrade has been stabilized with Fly-ash. Results show a significant increase in shear strength, CBR, and cohesiveness [9].

Different methods such as preparing suitable material, using mechanical techniques, and using additives are common in subgrade enhancement. Application of chemical additives has been proposed using reliable research in soft subgrade, some of which are listed below:

Advanced techniques enhanced subgrade bearing capacity instead of the lime treatment method [10].

Application of cement and lime lonely had disadvantages such as insufficient specified properties and environmental impacts. So the combination of them in suitable dosage had an important influence. The optimum proportion was investigated using a compressive strength test, and results show the highest amount [11].

Due to rolling stock movement, forces are applied to the track and cause movement in horizontal and vertical planes. Horizontal forces have resisted by longitudinal and lateral resistance of the track. Using the different materials and procedures, resistance against forces has increased. Longitudinal resistance has improved using continuous welded rails (CWR) technology. However, it is impossible to join the rails in tight curves due to higher lateral forces. The material, size, geometry, and dimension of track components affect lateral resistance. Researchers have carried out several studies to enhance lateral resistance. In this regard, changing sleeper shape is a common method. Lateral resistance has influenced by various factors such as environment conditions, applied loads, track components, track geometry, and maintenance

procedure. The lateral resistance between ballast and sleeper usually is conducted using the tests with single or multiple sleepers in full-scale or scaled model in laboratory or in situ [12]. The ballast layer geometry and interaction between the ballast and the sleeper is the main factor of lateral resistance [13]. With the introduction of CWR, buckling may occur due to thermal expansion. So, lateral resistance is an important factor in track stability. In this regard, a series of laboratory tests were carried out using STPT and track panel pullout test (TPPT) on different types of concrete sleepers. Results revealed the importance of the shape, the spacing, and the number of sleepers [14]. Determination of participation of each part on total lateral resistance has important to choose a sleeper and designing the components in railway. Lateral resistance of the sleeper achieves from sum of base, crib, and shoulder area. According to the experimental laboratory research on STPT test and corresponding to the material of sleeper, base area resistance of concrete, steel, and wood are 62%, 56%, and 51%, crib area are 28%, 27%, and 18% and shoulder area are 9%, 22%, and 26%, respectively [15].

The sleeper's shape significantly affects ballasted track's lateral resistance [16]. Changing the shape and material of the sleeper is recommended by scientists. In this regard, the frictional sleeper is an effective solution. The measurement has been conducted on conventional and frictional B70 sleepers by panel displacement method. Results show an increase in lateral resistance [17]. Based on the experimental test, the lateral resistance of three different frictional sleepers has been evaluated using the STPT test. Results indicated increases in lateral resistance due to frictional sleeper-enhanced interaction between ballast particles and sleeper [18]. A numerical model in finite element software has developed and investigated the effect of shoulder extend, base friction, and ballast layer thickness. Compared with the conventional sleeper, the frictional sleeper led to increased lateral resistance. A decrease in the ballast layer causes an increase in lateral resistance. Increasing in ballast shoulder, results increase in lateral resistance [19]. Y-shape steel sleeper in ballasted track has been investigated based on experimental methods using STPT and lateral track panel test (LTPT). The longitudinal resistance force (LRF) in STPT and LTPT [20]. The lateral resistance of HA110, winged and middle-winged sleeper achieved from STPT test, compared to the conventional B70, increased [21].

Track maintenance is one of the factors that influence lateral resistance. The lateral resistance was reduced significantly due to surfacing and increased by mechanical stabilization following the surfacing [22, 23]. The influence of ballast material type on the interaction between ballast and sleeper has been investigated. So the ballast consisting of crushed and angular particles has more lateral resistance than rounded and crushed angular types [24]. The lateral resistance of polyurethane-mixed ballasted track has been investigated using a discreet element model. Results show increases in lateral resistance due to an increase in the bonding depth of the shoulder ballast [25]. Lateral support is a new method to enhance lateral resistance in ballasted tracks. Field investigation by using STPT and Multi Tie Push Test (MTPT) tests and numerical modeling illustrated that lateral supports significantly increase lateral resistance [26]. Ballast bonding is a way to enhance track performance. Lateral resistance increases in curves due to bonding stabilization technology [27]. Waste tiers have been used in ballasted track foundations, rendering higher lateral resistance [28]. The use of geogrid causes a decrease in lateral deformation [29]. A field and laboratory sample has been made by geogrid stabilized ballast layer. The STPT and track panel displacement tests have been conducted. The results show an increase in lab and field, respectively [30].

The comprehensive method that increase majority of ballasted track disadvantages considering economic impact rarely proposed. A method is needed that, while improving the desired properties in terms of mechanical, physical, durability, environment impact, construction time, maintenance operation and dynamic, is also economic and constructive. Slab-track is the method that developed recently due to its advantages compared to ballasted track. But the economic issues and complicated construction technology are the challenges to prevent comprehensive extension. So the middle method is containing majority advantages of both of methods is needed.

2. Measuring tests

Using road construction experience with Royal Road Product ($RRP_{235Special}$), as an innovative method for the first time, the layers underneath the sleeper have been replaced with the clayey subgrade stabilized with $RRP_{235special}$. To investigate reaction against applied forces, a series of static and dynamic lab and field experiments such as maximum compaction test, California bearing ratio, unconfined compressive strength, Brazilian indirect tensile test, direct shear strength, uniaxial cyclic tests, and single tie push test (STPT) are needed. All the tests were done using the international codes according to **Table 1**.

The samples were made in different $RRP_{235special}$ dosages according to **Table 2**.

Test name	Type of test	Standard code
Maximum compaction test	Laboratory	ASTM D 698-78 [31]
Uniaxial compression test	Laboratory	ASTM C39 [32]
Brazilian indirect tensile test	Laboratory	ASTM C496 [33]
Direct shear strength	Laboratory	ASTM D3080 [34]
California bearing ratio (CBR)	Laboratory	ASTM D1883 [35]
Ballast box	Laboratory	—
Plate loading test (PLT)	Field	DIN 18134 [36]
Single tie push test (STPT)	field	—

Table 1.
Table of tests.

Sample number	$RRP_{235special}$ dosage (lit/m^3)
1	0
2	0.09
3	0.15
4	0.21
5	0.27

Table 2.
Dosage of RRP235special in different samples.

3. Royal road product 2-3-5 special (RRP$_{235special}$) introduction

The RRP$_{235special}$ has been made in Germany. The additive is acidic liquid and affects clayey soil through the chemical–mechanical process. **Figure 1** shows the RRP$_{235Special}$ with the R symbol and its chemical reaction.

As shown in **Figure 2**, the additive acts chemical process in three stages dissociation, ion exchange, and neutralization. The additive is diluted with water to achieve dissociation. Then, the mixture is pure to the soil, and the exchange of ion starts. The reaction time is different depending upon the type of soil, fine grain fraction, and the chemical elements of the soil. Finally, the neutralization is done by exodus of water.

The soil particles can perform the chemical reaction with water and other elements only when the fine grain fraction is less than 0.06 mm. Large part of soil (sand and gravel) cannot produce a chemical connection with water. So particles smaller than 0.06 have a key role in clayey soil stabilization with RRP$_{235special}$.
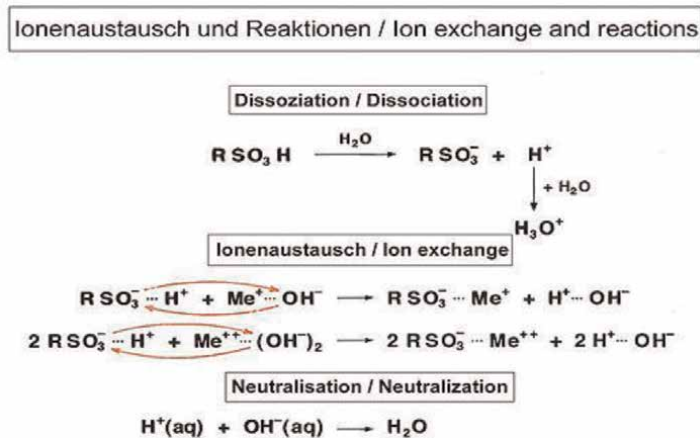
Figure 1.
Chemical reaction of RRP235Special [37].
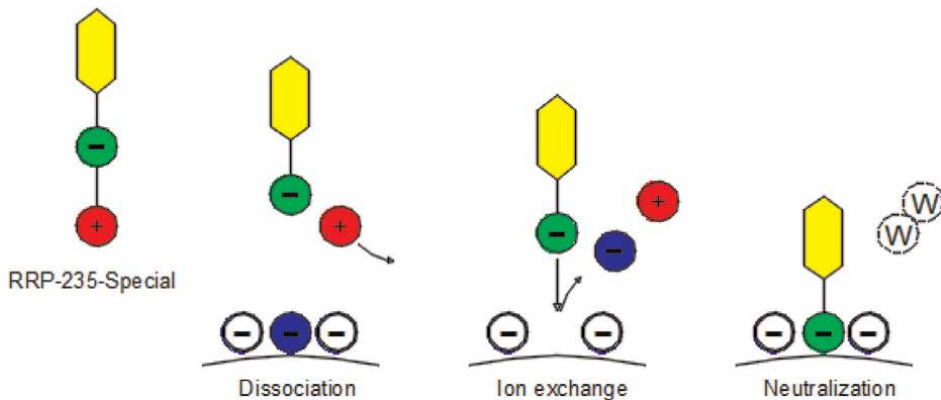
Figure 2.
Description of the ion exchange at the colloids [37].

4. Clayey sand subgrade

As mentioned in the last paragraph, the percentage of fine particles smaller than 0.06 indicates $RRP_{235special}$ dosage. The soil was brought from Urmia railway station. Typically the region soil has enough clay.

The primitive soil tests such as particle size distribution were done, and the type of soil was specified. Results revealed 40–50% of soil was smaller than 0.06 mm (**Figure 3**).

5. Sample preparation

The results of tests must achieve the least acceptable amounts. As mentioned in **Table 1**, laboratory and field experiments are needed to investigate additive performance. The similarity of samples must be considered. In this regard, all the specimens have equal water content and compaction energy.

The specimens were made with different additive dosages according to ASTM D 698 standard. The compaction energy for all the specimens was same and determined from eq. (1):

$$E = \frac{N * L * W * h}{V}$$

(1)

where E is compaction energy (kJ/m^3), N is the number of blows, L is the number of layers, W is hammer weight (N), h is the height of falling (m), and V is the mold volume (m^3).

According to the manufacturer's guidance, additive usage amounts were classified into five dosages of 0, 0.09, 0.15, 0.21, and 0.27 lit/m^3. The chemical process needs at least 8 hours for ion exchange.
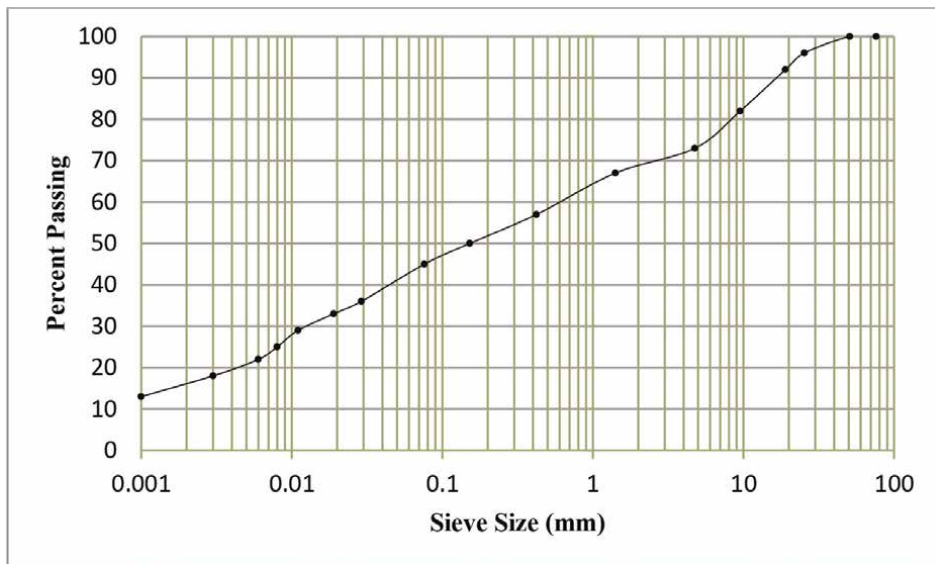
Figure 3.
Particle size distribution of the soil.

6. Tests

According to **Table 1**, the tests were done to investigate the proposed method. First, the lab experiments were done for different additive dosages, and the optimal amount was found. Using optimal dosage, the track with 50 meters length in 4 RRP$_{235special}$ stabilized subgrade layers was constructed in Urmia railway station. Then the field tests were done on this site.

6.1 Maximum compaction test

The maximum compaction is a common test that gives useful information about optimum water content and maximum density of soil. The test can be done in the standard proctor and modified proctor method. The results are criteria of sample preparation and field controls and guides (**Figure 4**).

6.2 Uniaxial compression test

The samples were made in a cubic vessel with dimensions of 15 by 15 by 15 cm. To investigate the effect of time on additive performance, six different ages was selected. **Figure 5** depicts some of the prepared samples. The last series of specimens were tested at the age of 46 days and visually completely dried.

6.3 Indirect Brazilian tensile test

This test is an indicator of soil tensile strength. The samples were made in a standard mold with different dosages of an additive, according to **Table 2**. The age of 46 days was selected to compare the latest uniaxial compressive test time. **Figure 6** shows the sample with 0.15 lit/m^3 in the Brazilian Indirect Tensile Test device before failure.

Figure 4.
The mold of maximum compaction test.

Figure 5.
a) sample with 0.15 lit/m³ additive tested in 7 days of age and b) sample with 0.21 lit/m³ additive tested in 28 days of age.

Figure 6.
The sample with 0.15 lit/m³ additive in Indirect Brazilian Tensile Test device.

6.4 Direct shear test

As the additive affects surface energy of colloids, shear parameters need to investigate. Based on the manufacturer's statements about the possibility of loading the route and releasing traffic immediately after construction, the shear test age was conducted on the day after sample preparation (**Figure** 7) [37].

6.5 Uniaxial cyclic test

A series of dynamic tests were carried out to investigate proposed track properties. Each track component has a specific role, and the performance depends on its type

Figure 7.
Direct shear test device.

and geometry. Any change in the specification of a component leads different reaction. The important factors of track under dynamic loads were investigated using the Ballast box test. The Ballast box device simulates applied forces from rolling stock to track.

6.6 Cyclic test setup

As depicted in **Figure 8**, the ballast box device is used at IUST University to simulate rolling stock forces applied to the track. The device includes power supplier, pump, and piston to provide vertical forces, computer software, sensors to measure displacements and calculate them, and a box to hold ballast specimens. The dimension of ballast box and piston is 0.7 m (l) × 0.45 m (h) × 0.3 m (w) and 0.22 × 0.22 m, respectively. Using the hydraulic pump power controlled by software in terms of applied force and frequency, the piston applies vertical force to specimen in box. This process continues to 100,000 cycles. In this research, the vertical force of 27 kN and frequency of 3 Hz in 100,000 cycles were applied to the specimens.

6.7 California bearing ratio (CBR)

The CBR is a well-known test in transportation projects. The CBR is a criterion of acceptance of structural layer proficiency. The specimens in CBR test were tested at 1, 3, and 7 days of age in wet situations (**Figure 9**).

6.8 Plate loading test (PLT)

This test aims to help determine important parameters such as Young's modulus, deformation, and strengths characteristics, and modulus of subgrade reaction. Different methods are used according to the type of structure. Due to the frequency of
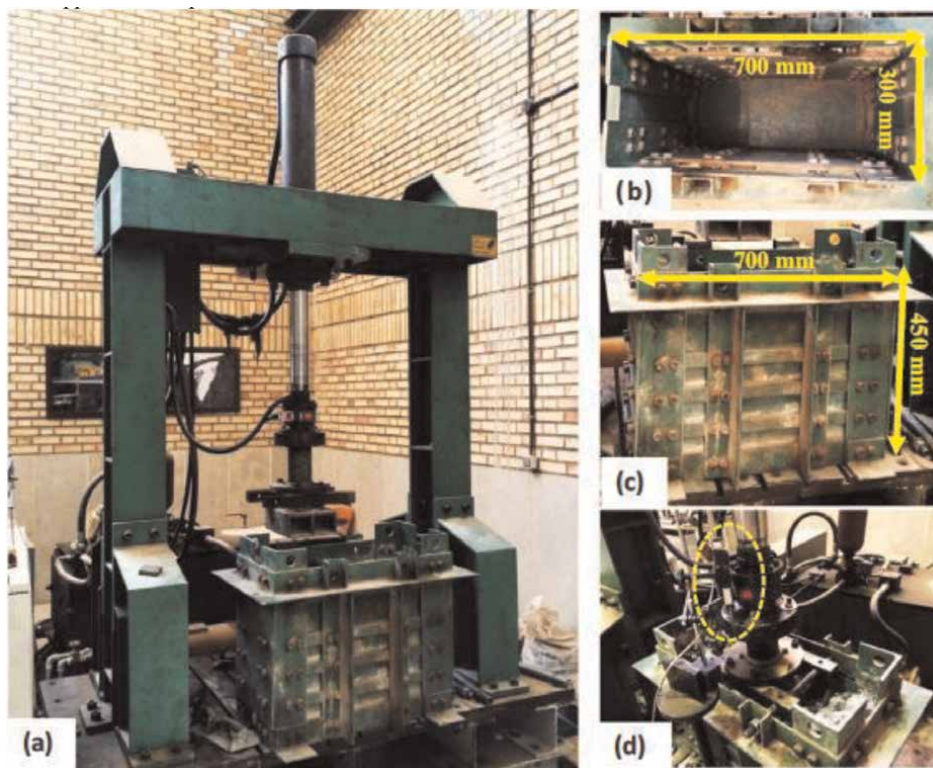
Figure 8.
a) Ballast box test apparatus; b and c) ballast box dimensions; d) LVDT location [38].

Figure 9.
The CBR device.

Figure 10.
PLT test device.

loading and unloading cycles in transportation engineering, incremental and cyclic loading can be used. The test can be done at surface level or subgrade depth (**Figure 10**).

6.9 Lateral resistance

Due to recent development in train speed and freight and the use of CWR technology, lateral resistance is a key parameter to provide track safety and stability and counteract buckling. Lateral resistance of railway track measures using four methods mentioned below [39]:

1. single tie push test (STPT),

2. panel displacement test,

3. mechanical track displacement test, and

4. continues dynamic measurements of lateral resistance.

In this study, the STPT test was selected and used (**Figure 11**). In ballasted tracks, the most important components that affect lateral resistance are sleeper and ballast layer specifications such as shape, material, geometry, thickness, and interaction between them.

7. Lab tests result

7.1 Maximum compaction test

With due attention to part 3 and the principle of additive chemical act, further use of RRP$_{235special}$ causes more water release using ion exchange process and decreases optimum water content. The more use of RRP$_{235special}$, the more release of interlayer

Figure 11.
STPT test devices.
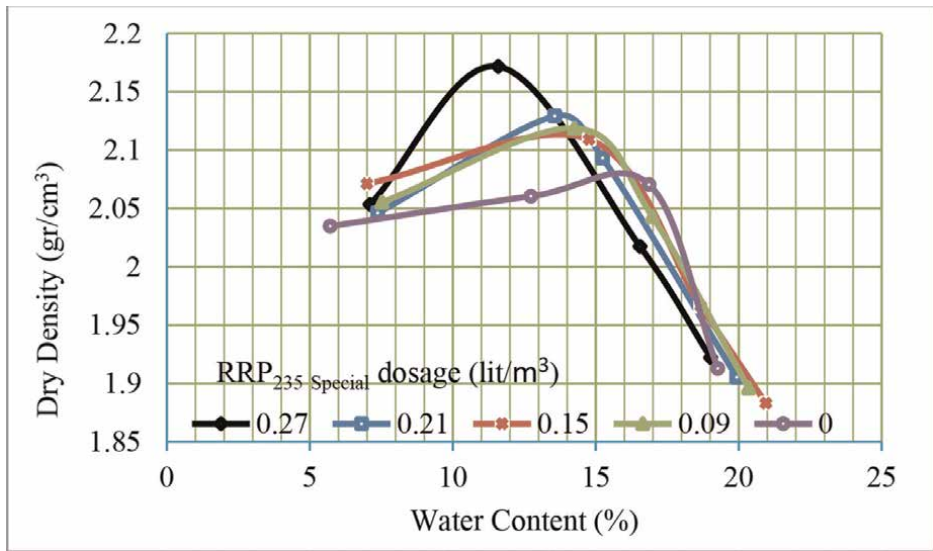
Figure 12.
Maximum dry density curves.

water. Also, the additive arranges the colloid placement. Releasing interlayer water and colloids arrangement increases congestion and maximum dry density. The results in **Figure 12** reveal that maximum dry density increases and optimum water content decrease by 4, and 38 percent, respectively.

7.2 CBR

The CBR ratio limitation for subballast, subbase, and base are 25, 30, and 80, respectively [40, 41]. Application of $RRP_{235special}$ increases CBR value in general. But
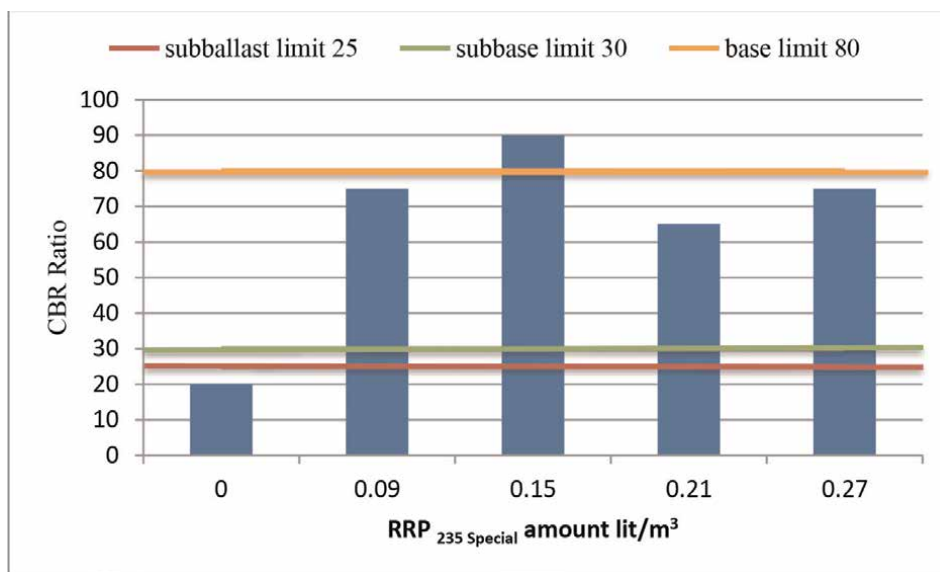
Figure 13.
The effect of RRP235 special on CBR value.

the strengthening is not proportion to the additive dosage. As shown in **Figure 13**, the CBR ratio increases from 0 to 0.15 lit/m^3 additive dosage and then is reduced and then by further use of the additive, is increased and strength again. In the optimum dosage of additive (0.15lit/m^3), the CBR increased more than 400% compared to the sample with no additive.

Clay colloids absorb a certain amount of additives, and the excess remains between the colloids. A large amount of excess material seems to reduce the soil's physical properties and make the situation glide colloids. Due to the concentration of the ions, the zeta potential decreases, and cations and anions are liberated from the diffuse double layer; thereupon, the swelling properties of soil reduce [42].

7.3 Compressive test results

To place the sleepers on the stabilized layer, the minimum strength of soil is needed to be evaluated by compressive test. Similar to the CBR test results, the use of additives gives higher strength to the specimens. The strengthening process ascends from 0 to 0.15 lit/m^3 and then descends. This pattern is repeated at different ages. As indicated in **Figure 14**, the use of RRP$_{235special}$ had caused a 46 and 300 percent increase in compressive strength compared to the sample with no additive. Therefore, the optimal required amount of additive, according to **Figure 14** is 0.15lit/m^3.

7.4 Indirect Brazilian tensile test results

The tensile strength has improved using RRP$_{235Special}$. Like the previous sections, increasing the additive usage up to 0.15 lit/m^3 increases the tensile strength and then descends. As shown in **Figure 15**, the sample with 0.15 lit/m^3 additives has the best result and is selected as the optimum dosage. Compared to the sample with no additive, the strength improves by more than 20%. Comparing **Figures 14** and **15** reveals that more compressive strength mirrors more tensile strength.
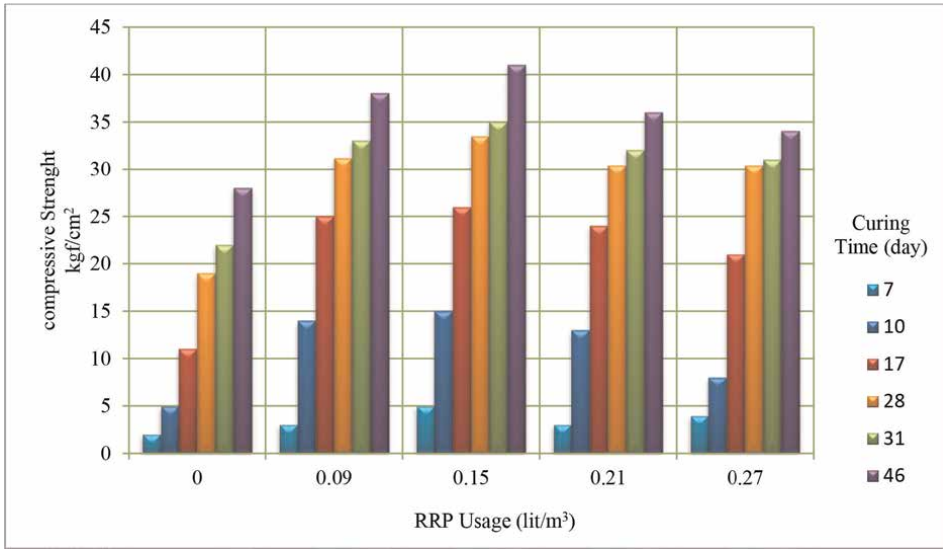
Figure 14.
RRP-stabilized soil compressive strength with different amounts over time.
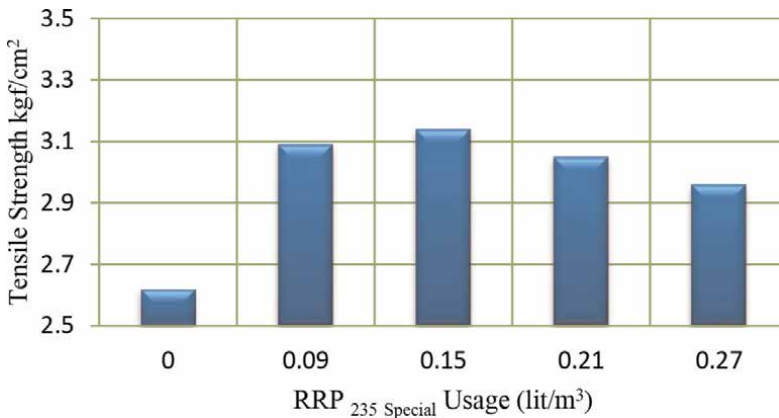
Figure 15.
Tensile strength of samples with different RRP235 special at 46 days of age.

7.5 Direct shear test results

As depicted in **Figure 16**, the maximum shear stress was obtained from Mohr–Coulomb diagrams.

To evaluate shear stress, different samples with $RRP_{235special}$ were made and tested. The additive has a positive role in the shear parameter. As illustrated in **Figure 17**, same as in previous tests, the strengthening pattern ascends up to 0.15 lit/m^3 additive and then decreases, and further use causes increases again. The 0.15 lit/m^3 amount is determined as the optimum value among the used additive dosages.
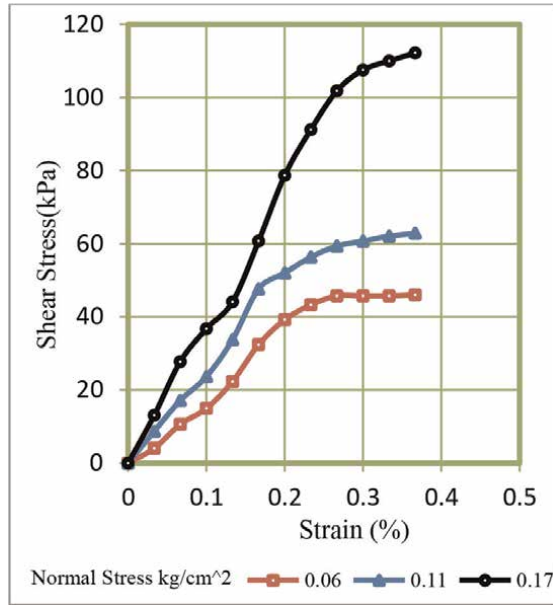
Figure 16.
Shear stress–strain diagram (the sample with 0.15 lit/m³ additives).
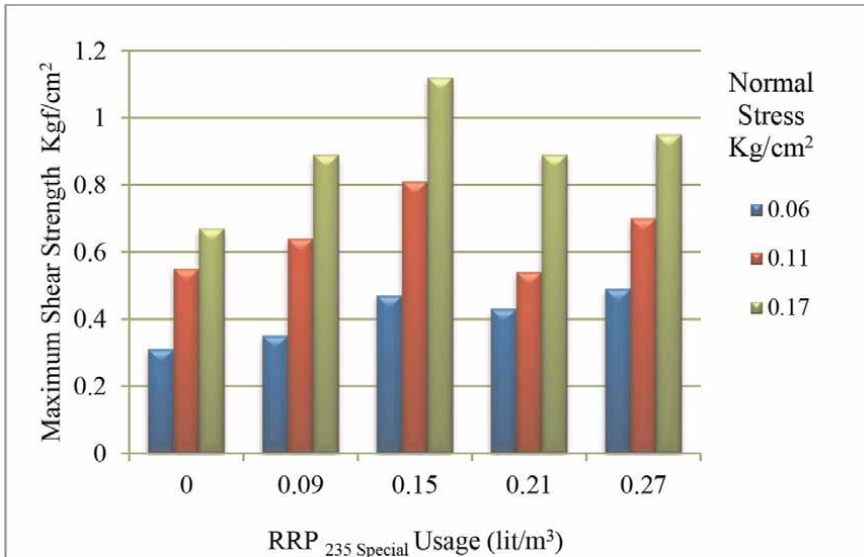
Figure 17.
Maximum shear stress diagram.

Good compaction and high density of soil increase the shear strength. When the reaction has occurred, less water can accumulate in the soil than was originally possible. As a result, the swelling capacity is reduced, the internal moisture of the soil is also reduced, and complete compaction to zero content of air-tilled voids becomes possible because of the space that has become available from the expelled pore water. Subsequent additions of water cannot reverse this process once the latter has been accomplished (the swelling capacity is destroyed and the shearing strength increased) [43].

7.6 Uniaxial cyclic test results

7.6.1 Settlement

Vertical and horizontal displacement of structural layers is an important problem in ballasted railways that cause noticeable geometry change, reduce maintenance intervals, and consequently increase maintenance costs. The RRP$_{235special}$ stabilized clayey soil can replace the ballast underneath the sleepers. This led a significant reduction of displacement in vertical and horizontal directions. The specimens with different dosages of additives were made in special boxes and tested using a ballast box device. **Figure 18** shows the specimens after 100,000 cycles of loading.

The ballast box test was carried out on the samples, and as rendered in **Figures 19** and **20**, the additive is an influential factor in the strengthening of clayey soil. Reverse to the static tests pattern, the sample with 0.15 lit/m^3 has the least amount (2 mm), and the specimen with no additive has the largest amount (4.7 mm) of settlement. Use

Figure 18.
Ballast box samples after testing (specimens from left to right correspond to 0, 0.09, 0.15, 0.21, and 0.27 lit/m³ of RRP235 Special).
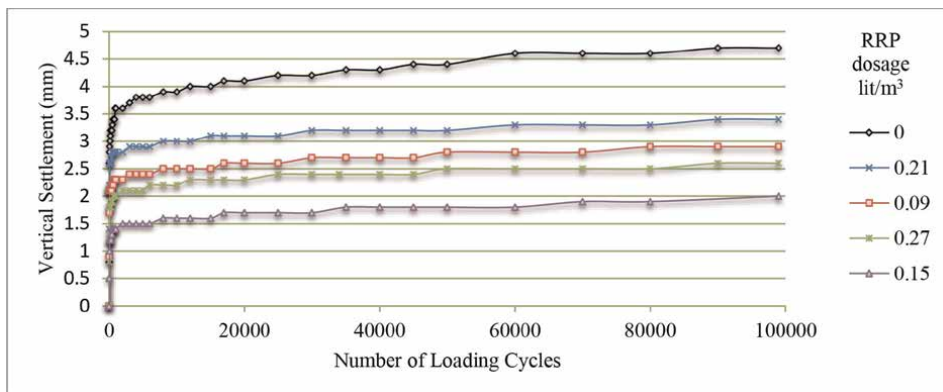
Figure 19.
Settlement diagram.
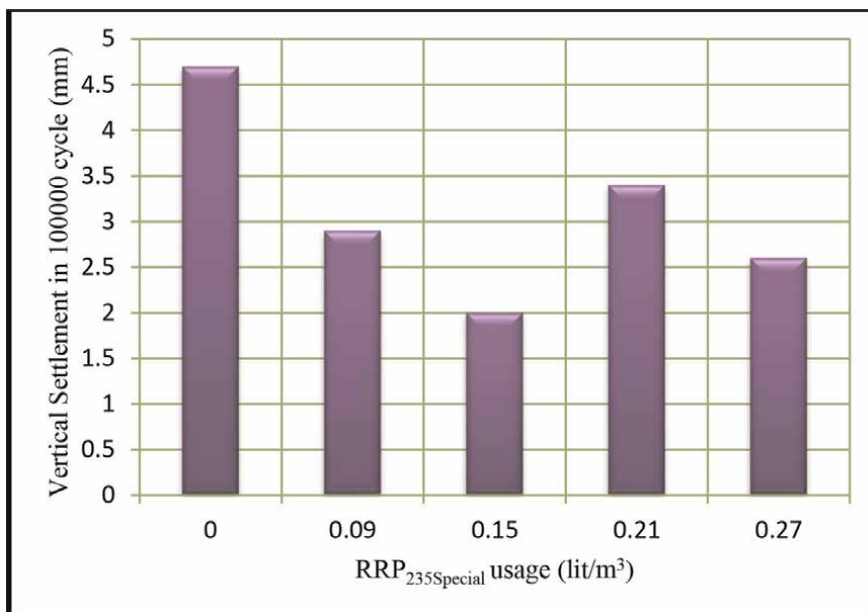
Figure 20.
Settlement of samples in cycle 100,000.

of RRP$_{235special}$ causes more than 57% reduction in vertical displacement. Therefore, the dosage of 0.15 lit/m^3 was selected as the optimal amount in terms of settlement in the ballast box test.

The exodus of interlayer water due to ion exchange gives improved compaction to the stabilized soil and is the main factor of strengthening, but increased additive results in excess of free ions around the colloids, which renders negative properties [43].

7.6.2 Stiffness

The stiffness of the track is affected by the materials used. Any change in material type causes a change in stiffness. Using the ballast box test, the stiffness of clayey soil with different additive dosages has been evaluated. According to the RRP$_{235special}$ action, the results are predictable. As shown in **Figure 21**, the sample with 0.15 lit/m^3 RRP$_{235Special}$ has the highest stiffness, and the sample with no RRP$_{235Special}$ has the lowest. Low and high stiffness limits have been shown in **Figure 21** by 30 and 80 kN/m, respectively [40]. The specimen with 0.15lit/m^3 has the best result and is selected as the optimal value for stiffness.

7.6.3 Damping ratio

Comparing different amounts of RRP$_{235Special}$, the damping ratio of each sample, which is representative of the lost energy, divided by the energy input in a cycle, has been determined using eq. (2), proposed by Jacobsen [44];

$$\xi = \frac{\Delta E}{2\pi K x^2} \tag{2}$$
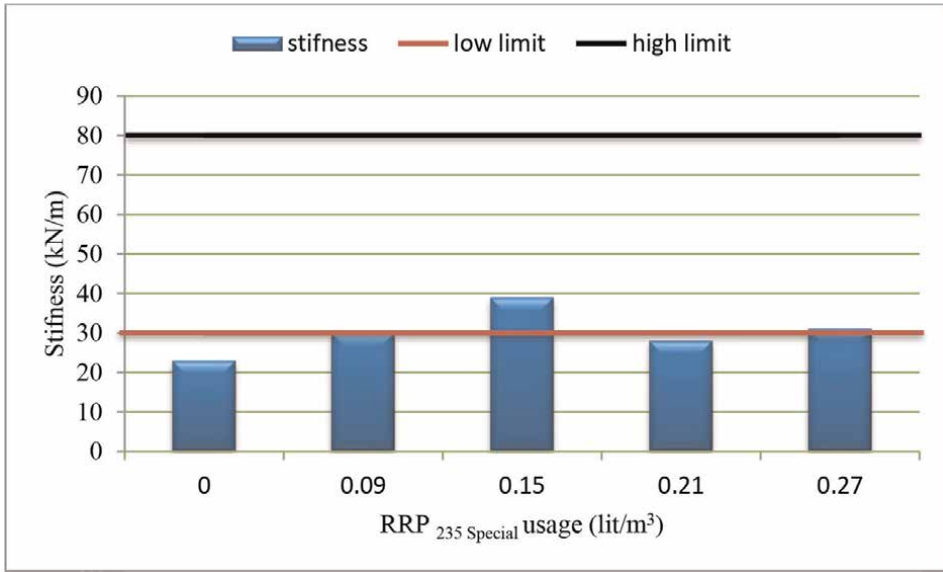
Figure 21.
Stiffness of samples with different dosages of RRP235Special.

Where ΔE is the dissipated energy, and k and x refer to the stiffness and deflection of samples, respectively.

Figure 22 shows the force–displacement relationship of the sample with 0.15lit/m^3 RRP$_{235\ Special}$ at the final cycle (100,000th). The red zone on this graph indicates the dissipated energy. In order to calculate the damping ratio of the samples, the area of this zone should be divided by that of the loop.
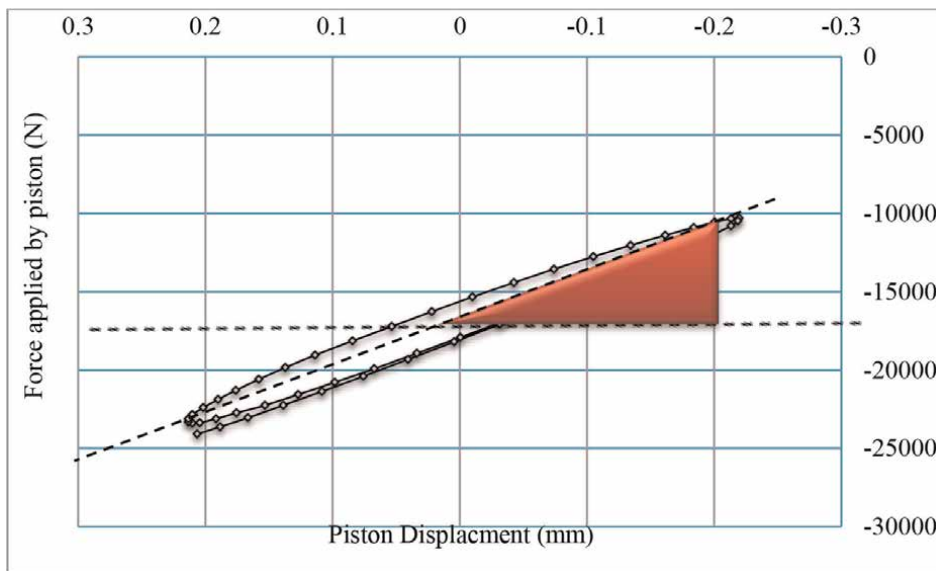
Figure 22.
Calculation of damping ratio by means of the force–displacement.

Figures 23 and 24 show the force–displacement loops of all samples and their damping ratio values, respectively.

The settlement, stiffness, and damping ratio are interdependent. The damping ratio and settlement are opposite of the stiffness. The specimen with high stiffness has a low settlement and damping ratio. Greater concentration of colloids with the use of additive and ion exchange causes vibration transmission and low damping ratio. So the results shown in **Figure 24** confirm the relation between the specifications. The sample with a high damping ratio behaves better facing dynamic forces and reduces transmitted energy than others. The sample with 0.15 lit/m^3 has the lowest, and the sample with no additive has the highest damping ratio. The sample with no additive was selected as optimal dosage for damping ratio. But the preference for stiffness and settlement cause the challenge of optimal dosage selection. So the dosage of 0.15 lit/m^3 has been selected as an optimal value for dynamic tests.

Samples with different dosages of additive were made, and an optimal percentage was found. As a result, the sample with 0.15 lit/m^3 RRP$_{235Special}$ was determined as the suitable dosage for mechanical and physical tests, while only in the Maximum Compaction test, by increasing the additive, the optimum water content decreased.
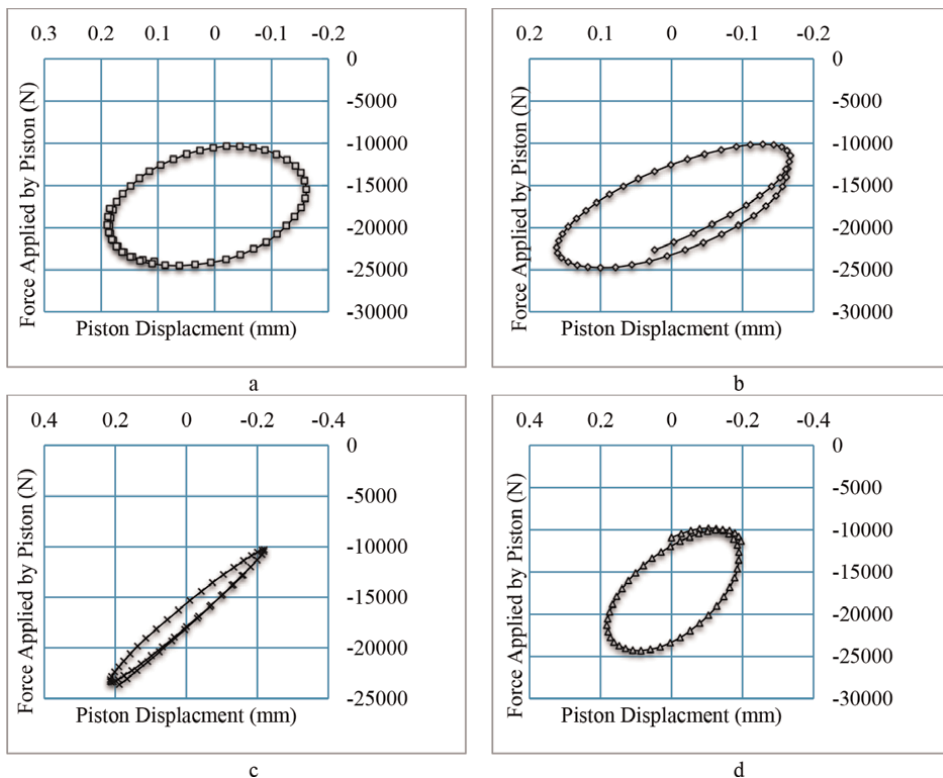
Figure 23.
Piston Force–displacement graphs for five different samples (a, b, c, d, and e are the sample with 0, 0.09, 0.15, 0.21, and 0.27 lit/m³ additive, respectively).
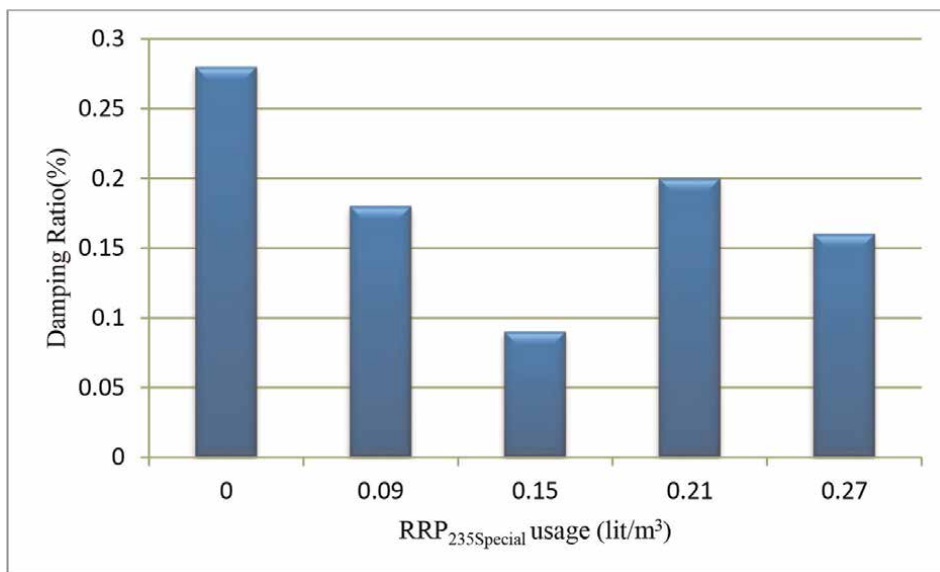
Figure 24.
Damping ratio of samples with different percentages of RRP235 special.

8. Field tests result

8.1 STPT

The lateral resistance was determined using STPT device in conventional and RRP$_{235special}$ stabilized tracks at Urmia railway station. All the characteristics are the same between tracks except ballast thickness under the sleeper.

Regarding the results, there is no significant difference between conventional and RRP$_{235special}$ tracks. The difference has two reasons. First, the ballast layer compaction in conventional tracks was more than RRP$_{235special}$ tracks, leading to higher side and end resistance. The second reason comes from the placement position of the ballast under the RRP$_{235special}$ track. When the roller compacts the ballast to the last stabilized layer, most ballast particles have rotated in a position that surfaces parallel to the sleeper's bottom side (**Figure 25**). So this led to the uniformity of layer decreases and

Figure 25.
The ballast particles placement under the sleeper in RRP235special method.
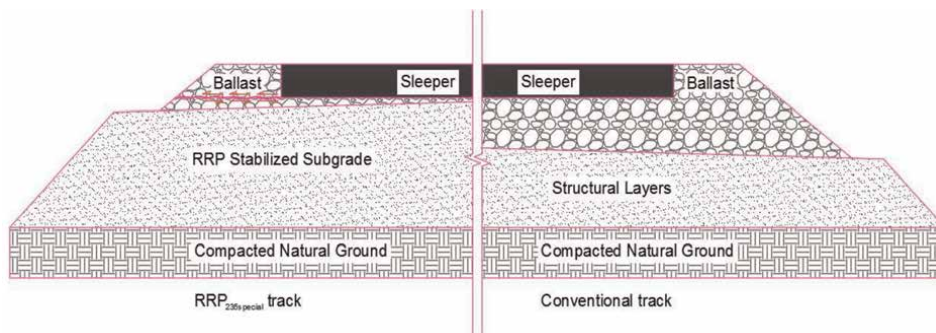
Figure 26.
Conventional and RRP235special tracks comparison.

caused less load transfer (**Figure 26**). Of course, this action has a beneficial side that causes increase in the contact area between ballast particles and the sleeper bottom side.

8.2 PLT

The PLT test was conducted in the Urmia railway station RRP$_{235special}$ stabilized track, conventional track, and in the part of the Urmia-Oshnaviyeh road track constructed by RRP$_{235stabilized}$ clayey soil. The EV was determined, and there are significant differences between conventional tracks and RRP$_{235special}$ stabilized tracks. The results show an approximately 232% increase in EV.

9. Conclusion

RRP$_{235special}$ is an acidic additive that makes a situation in which colloid surface energy changes, and consequently, water is released, and using the physical process, permanent compaction is created. The result of lab and field experiments indicated improvement of stabilized clayey soil properties.

1. The RRP$_{235special}$ stabilized clayey soil has less optimum water content and much maximum dry density.

2. Static tests include compressive strength, tensile strength, shear stress, and CBR, has improved due to stabilization with additives. The sample with 0.15 lit/m^3 has been selected as the optimal dosage, and the pattern of strengthening is the same.

3. The RRP$_{235special}$ influenced the soil positively in terms of dynamic tests. The results render significant enhancement in stabilized soil properties. RRP235special stabilized clayey soil has the highest stiffness and lowest settlement and damping ratio. Additives increase the parameters of clayey soil to acceptable limit values. The sample with 0.15 lit/m^3 has been selected as the optimal dosage in terms of dynamic tests.

4. Stabilizing clayey soil with RRP completely differs from ordinary materials such as cement and lime. RRP changes the properties of colloids and gives permanent

changes to the soil, whereas cement and lime give their own properties to the soil. RRP-stabilized soil properties depend on the chemical–physical process, so there is no limitation to compaction energy. According to the manufacturer's statement, the additive makes colloids hydrophobic, creating a waterproof layer and consequently preventing capillarity.

5. In term of methodology, the STPT test in the field was conducted, and lateral resistance was measured in both of conventional and $RRP_{235special}$ method. Generally, the lateral resistance of the tracks is almost the same. There is no need to use other methods to increase lateral resistance. Therefore, the $RRP_{235special}$ method can be recommended because of lateral resistance.

6. The PLT test was conducted, and the results showed significant increases in EV.

Acknowledgements

Conflict of interest

This research did not receive any specific grant from funding agencies in the public, commercial, or nonprofit sectors.

Author details

Hossein Ghorbani Dolama
Department of Civil Engineering, Science and Research Branch, Islamic Azad University, Tehran, Iran

*Address all correspondence to: hossein.ghorbani@srbiau.ac.ir

IntechOpen

References

[1] Sameera VKN, Udayakumara EPN, Dhammika JK. Stabilization of weak subgrade soil for road construction using fly ash and rice husk ash - Mahokanda, Sri lanka. International Journal of Scientific and Research Publications. 2018;**8**(1)

[2] Kang X et al. Chemically stabilized soft clays for road-base construction. Journal of Materials in Civil Engineering. 2015;**27**

[3] Karamia H et al. Use of secondary additives in fly ash based soil stabilization for soft subgrades. Transportation Geotechnics. 2021;**29**

[4] Lazorenko G et al. Dynamic behavior and stability of soil foundation in heavy haul railway tracks: A review. Construction and Building Materials. 2019;**205**:111-136

[5] Thevakumara K et al. The influence of cyclic loading on the response of soft subgrade soil in relation to heavy haul railways. Transportation Geotechnics. 2021;**29**

[6] Ahmadi HC et al. The effect of zeolite and cement stabilization on the mechanical behavior of expansive soils. Construction and Building Materials. 2021;**272**

[7] Arab MG et al. Resilient behavior of sodium alginate–treated cohesive soils for pavement applications. Journal of Materials in Civil Engineering. 2019;**31**:04018361-1

[8] Moayed RZ, Lahiji BP. Effect of wetting- drying cycles on CBR values of silty subgrade soil of Karaj railway. In: Proceedings of the 18th International Conference on Soil Mechanics and Geotechnical Engineering. Paris; 2013. pp. 1321-1324

[9] Vukićević M et al. Fly ash and slag utilization for the serbian railway substructure. Transport. 2018;**33**(2):389-398

[10] Celauro B et al. Design procedures for soil-lime stabilization for road and railway embankments. Part 1 - review of design methods. Social and Behavioral Sciences. 2012;**53**:755-764

[11] Malkanthi SN, Balthazaar N, Perera AA. Lime stabilization for compressed stabilized earth blocks with reduced clay and silt. Case Studies in Construction Materials. 2020;**12**:8

[12] Tomita H, Hayano K, Anh PT. Effects of model scale on lateral resistance characteristic of sleepers in railway ballasted tracks. 2017

[13] Jing G, Aela P. Review of the lateral resistance of ballasted tracks. Rail and Rapid Transit. 2019;**0**(0):1-14

[14] Koike Y et al. Numerical method for evaluating the lateral resistance of sleepers in ballasted tracks. Soils and Foundations. 2014;**54**(3):502-514

[15] Zakeri JA, Bakhtiary A. Comparing lateral resistance to different types of sleeper in ballasted railway tracks. Scientia Iranica A. 2014;**21**(1):101-107

[16] Hayano K et al. Effects of Sleeper Shape on Lateral Resistance of Railway Ballasted Tracks. In: Conference paper in Geotechnical Special Publication. 2014

[17] Zakeri JA, Mirfattahi B. Field investigation on the lateral resistance of railway tracks with frictional sleepers.

In: IOP Conference series, 3rd International conference on engineering science. Materials Science and Engineering. 2020. p. 671

[18] Guo Y et al. Effect of sleeper bottom texture on lateral resistance with discrete element modelling. Construction and Building Materials. 2020;**250**

[19] Zakeri JA et al. A numerical investigation on the lateral resistance of frictional sleepers in ballasted railway tracks. Rail and Rapid Transit. 2014; **0**(0):1-10

[20] Zakeri JA, Bahari Y, Yousefian K. Experimental investigation into the lateral resistance of Y-shape steel sleepers on ballasted tracks. Rail and Rapid Transit. 2020. p. 1-8

[21] Mansouri P et al. Discrete element method analysis of lateral resistance of different sleepers under different support conditions. Construction and Building Materials. 2022. p. 327

[22] Sussmann T, Kish A, Trosino M. Influence of track maintenance on lateral resistance of concrete-tie track. Transportation Research Board. 2003. p. 1825

[23] Sussmann T, Kish A, Trosino M. Investigation of the influence of track maintenance on the lateral resistance of concrete tie track. 2015

[24] Mulhal C, et al. Large-Scale Testing of Tie Lateral Resistance in Two Ballast Materials. In: Third International Conference on Railway Technology: Research, Development and Maintenance. 2016

[25] Ling X, Xiao H, Jin F. Investigating the effect of different bonding areas on the lateral resistance of polyurethane-mixed ballast using the discrete element

method. Rail and Rapid Transit. 2021; **235**(2):133-142

[26] Zakeri JA. Milad Alizadeh Galdiani, and Seyed Ali Mosayebi, field investigations on the effects of track lateral supports on the ballasted railway lateral resistance. Periodica Polytechnica Civil Engineering. 2020; **64**(3):640-646

[27] D'Angelo G, Thom N, Presti DL. Bitumen stabilized ballast: A potential solution for railway track-bed. Construction and Building Materials. 2016;**124**:9

[28] Indraratna B, Ngo TN, Ferreira F. Advancements in Track Technology: Use of Artificial inclusions for stabilising Transport Infrastructure. 2018. p. 6

[29] Sol-Sánchez M, Thom NH, Moreno-Navarro F, Rubio-Gámez MC, Airey GD. A study into the use of crumb rubber in railway ballast. Construction and Building Materials. 2015;**75**:6

[30] Morteza Esmaeili JAZ, Babaei M. Laboratory and field investigation of the effect of geogrid-reinforced ballast on railway track lateral resistance. Geotextiles and Geomembranes. 2017;**45**:11

[31] ASTMD698. Standard Test Methods for Laboratory Compaction Characteristics of Soil Using Standard Effort. 2007

[32] ASTMC39. Concrete Cylinderical Compression Testing. 2015

[33] ASTMC496. Standard Test Method for Splitting Tensile Strength of Cylindrical Concrete Specimens. 1996

[34] ASTMD3880. Standard Test Method for Direct Shear Test of Soils Under Consolidated Drained Conditions. 2003

[35] ASTMD1883. Standard Test Method for CBR (California Bearing Ratio) of Laboratory-Compacted Soils. 2007

[36] 736, Plate Loading Test of Soil and Weak Rock (Application, Method and Interpretation). Islamic Republic of Iran: Plan and Budget Organization; 2018

[37] Gerling, T. RRP Gmbh. 2016. Available from: RRPGmbh.com

[38] Esmaeili M, Aela P, Hosseini A. Experimental assessment of cyclic behavior of sand-fouled ballast mixed with tire derived aggregates. Soil Dynamics and Earthquake Engineering. 2017;**98**:1-11

[39] Zakeri JA. Lateral Resistance of Railway Track. London, UK: InTech; 2012

[40] Code of Railway Track Super Structure General Technical Specifications. The Ministry of road and transportation. 2005

[41] 234. Iran Highway Asphalt Paving Code No. 234. 1″Edition. The ministry of Roads and Urban Developmant; 2011

[42] Ghorbani H et al. Improvement of ballasted tracks using RRP stabilized soft clayey soils in Persian. Journal of Transportation Infrastructure Engineering (JTIE). 2020;**6**(4):20

[43] Pressmar P. Catalog of: RRP - Reynold's road packer RRP 235 special. In: CH Non-Food Corp. England: C.N.-F. Corp; 2022

[44] Jacobsen LS. Steady forced vibration as influenced by damping. Transactions ASME-APM. 1930;**52**(15):169-181

Chapter 6

High-Speed Train Traction System Reliability Analysis

Kunpeng Zhang, Bin Jiang, Fuyang Chen and Hui Yang

Abstract

As the core power unit of high-speed train (HST), the diagnosis of faults in traction motor system has a significant importance on both safety and reliability, which can avoid HST crashes. According to the current problems such as early fault characteristics are not obvious and tight coupling, the reliable model with fault severity analysis and the required diagnosis accuracy cannot be achieved by current techniques. Therefore, it is crucial to evaluate HST reliability through resilience enhancement strategies to ensure it can operate with higher resilience. This chapter proposes a method for evaluating the overall reliability of HST traction motors associated with the idea of system modeling and machine learning techniques. First, a novel fault severity model is proposed suitable for the normal and fault conditions. Then electromagnetic torque energy entropy coding is utilized to extract fault features and construct different feature matrixes. Resilience enhancement strategies with support vector machine models are generated from a novel gray wolf optimizer algorithm. The performance of the proposed work is validated through simulation and experimentation on a fault-testing verification platform for the HST traction system.

Keywords: reliability analysis, high-speed train, traction motor, fault severity modeling, coupled faults, resilience enhancement

1. Introduction

Compared with other transportation means, the high-speed train (HST) has been recognized as one of the most popular tools owing to its unique advantages such as safe, comfortable and environmentally friendly. It is reported that Japan, Germany, China and France have their own HST intellectual property rights [1, 2]. On the other hand, the system performance could be severely affected by various uncertainties, such as material diversities, manufacturing tolerances and operational environment variations, resulting in a high probability of failure. As the key power equipment of HST, the resilience enhancement of the traction motor control system is essential to ensure its reliable operation. Most of the fault feature extraction and diagnosis strategies are based on the motor current signature analysis, which may cause false-negative diagnosis results in several cases [1–3]. As an alternative analysis tool, the motor's torque has been proved as the resilience enhancement method most affected by the faults during the steady-state operation [4]. In addition, the HST traction motor is a

fail-safe system with few fault samples, which makes the traditional machine learning algorithm (especially neural network) fails to the lower diagnosis accuracy associated with limited fault characteristic information [5]. In order to improve the coupled fault diagnosis, the support vector machine (SVM) classification model optimized by the gray wolf optimizer (GWO) algorithm has been proposed in [6, 7]. Though GWO has more obvious optimization power than other heuristic algorithms, the optimal local outcomes will often occur with an inflexible scheme.

It is worth noting that most of the existing works are brought forward under the assumption that only certain types of single fault may occur [8, 9]. However, in practice, coupled faults are more common to encounter in HST [1]. Considering the tight coupling components in traction motor, a single stator interturn fault may eventually lead to rotor broken bar fault [10, 11].

In general, compared with the traditional method, this paper has considered electromagnetic torque characteristics, data driven model and fault attribute knowledge coding to construct an agile fault feature matrix. Aiming at the linear indivisible attribute between fault feature and the corresponding fault classes, an improved GWO (IGWO) has been proposed to agile optimize the SVM classification model with various fault severity levels. Through the experimental analysis of the multiple fault diagnosis indexes, the advantages of the proposed reliable diagnosis approach have been proved.

2. Resilience enhancement of traction motor with coupled faults

In order to achieve resilience enhancement with high accuracy and fast speed, the empirical mode decomposition (EMD), fault coding, SVM multiclassification model and IGWO are employed in this chapter, as shown in **Figure 1**.

2.1 Fault feature extraction

For the nonlinear electromagnetic torque signals, the EMD is introduced to decompose the signal into different linear components. Then, the intrinsic mode functions (IMF) obtained from the EMD are utilized to calculate the IMF entropy, which is used to determine the fault feature matrix with the help of fault attribute knowledge coding.

2.2 Fault mechanism analysis for traction motor control system

As shown in **Figure 2**, the traction control unit achieves control of the traction motor speed and current by adjusting the gating signal of the converter at a given traction/braking command. However, the existing control units only detect faults by comparing the measured values of the sensors with the threshold values, which makes it difficult to effectively diagnose early fault (bearing fault, broken rotor bars fault, stator interturn short circuit fault, air gap eccentricity fault, rotor broken bar and interturn short circuit coupled fault). During the small fault injection phase, the traction motor current, magnetic flux and speed still satisfy the fifth-order model in the stator-side (a, b) coordinate system. Related studies have shown that the variation of parameters such as rotational inertia, rotor resistance, stator resistance and mutual inductance in the motor model can respectively describe the severity of bearing fault, broken rotor bars fault, stator interturn short circuit fault, air gap eccentricity fault.
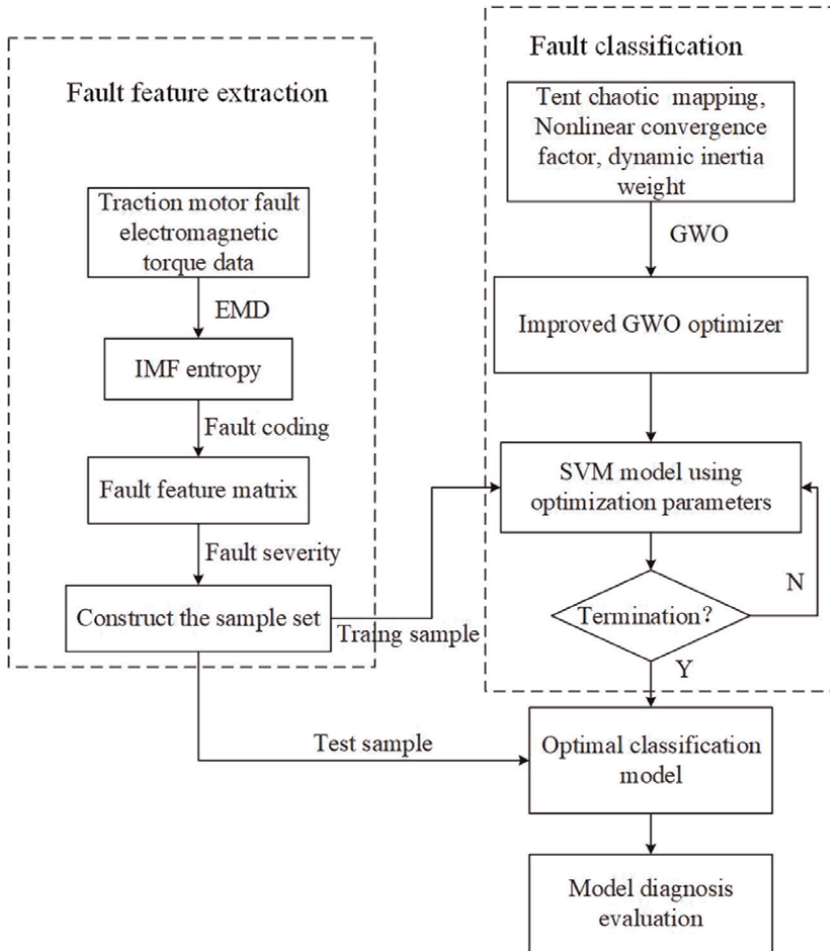
Figure 1.
Flowchart of the proposed method.
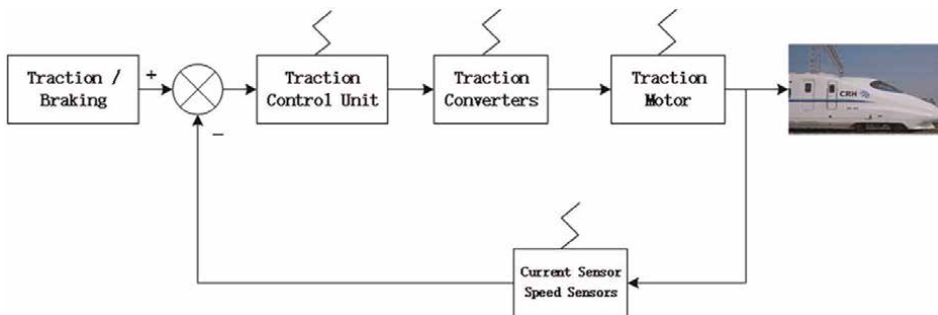
Figure 2.
High-speed train traction system.

$$\frac{dw}{dt} = \frac{1}{(J + \Delta J)}(\varphi_{sa}i_{sb} - \varphi_{sb}i_{sa} - T_L)$$

$$\frac{di_{sa}}{dt} = -\frac{(R_s + \Delta R_s)}{\sigma}i_{sa} - \frac{(R_r + \Delta R_r)}{L_r}(1 + \vartheta(M + \Delta M))i_{sa}$$

$$-\omega i_{sb} + \frac{(R_r + \Delta R_r)}{L_r\sigma}\varphi_{sa} + \frac{\omega}{\sigma}\varphi_{sb} + \frac{1}{\sigma}u_{sa}$$

$$\frac{di_{sb}}{dt} = -\frac{(R_s + \Delta R_s)}{\sigma}i_{sb} - \frac{(R_r + \Delta R_r)}{L_r}(1 + \vartheta(M + \Delta M))i_{sb} \qquad (1)$$

$$-\omega i_{sa} + \frac{(R_r + \Delta R_r)}{L_r\sigma}\varphi_{sb} + \frac{\omega}{\sigma}\varphi_{sa} + \frac{1}{\sigma}u_{sb}$$

$$\frac{d\varphi_{sa}}{dt} = -(R_s + \Delta R_s)i_{sa} + u_{sa}$$

$$\frac{d\varphi_{sb}}{dt} = -(R_s + \Delta R_s)i_{sb} + u_{sb}$$

$$T_e = \varphi_{sa}i_{sb} - \varphi_{sb}i_{sa}$$

where u_{sa} and u_{sb} are the stator side a phase and b phase voltages; i_{sa} and i_{sb} are the stator side a phase and b phase currents; φ_{sa} and φ_{sb} are the stator side a phase and b phase fluxes; w is the motor speed, J is the motor inertia, ΔJ represents the change in inertia in case of bearing fault; R_r is the rotor resistance, ΔR_r is the change in rotor resistance in case of broken rotor strip fault; R_s is the stator resistance, ΔR_s means the relative change of stator resistance; L_s, L_r and M are stator self-inductance, rotor self-inductance and mutual inductance, respectively; is the mutual inductance change during air gap eccentricity fault, T_L is the load torque; $\vartheta = \frac{M + \Delta M}{\sigma L_r}$, $\sigma = L_s\left(1 - \frac{(M + \Delta M)^2}{L_s L_r}\right)$.

From the above equation, it can be seen that the electromagnetic torque T_e contains the interaction of magnetic chain φ_{sa}, φ_{sb} and current i_{sa}, i_{sb}, and also describes the variation law of motor speed w. It is sensitive to the early motor fault variation quantities ΔJ, ΔR_r, ΔR_s and ΔM, which can best characterize the traction motor fault features. According to [10, 11], the motor early bearing fault severity η_1, broken rotor bars fault severity η_2, stator interturn short circuit fault severity η_3, air gap eccentricity fault severity η_4 can be quantified and described as follows:

$$\eta_1 = \frac{\Delta J}{J} \times 100\%; \quad \eta_2 = \frac{\Delta R_r}{R_r} \times 100\%$$

$$\eta_3 = \frac{\Delta R_s}{R_s} \times 100\%; \quad \eta_4 = \frac{\Delta M}{M} \times 100\% \qquad (2)$$

2.3 Fault severity levels coding

Based on the available fault features obtained by EMD and IMF entropy, the current analysis methods often ignore the difference in fault levels. In order to make use of the distributed feature more effectively, the fault features are first coded in group mode, and then the fault feature bases that reflects various fault severity levels can be obtained. According to [12], the grouping fault features can be divided into five subblocks in terms of normal state, bearing fault, rotor broken strip, interturn short circuit and air gap eccentricity. The corresponding fault codes are described as follows:

$$
\begin{cases}
f_1(H_1, H_j, B_1) = \gamma_1 \\
\quad\quad \vdots \\
f_5(H_1, H_j, B_5) = \gamma_5
\end{cases}
\tag{3}
$$

where $f_1, \cdots, f_5$ are the code mapping functions characterizing the motor operation conditions, $\gamma_1, \cdots, \gamma_5$ refer to the coded fault feature matrix; $B_1, \cdots, B_5$ are the five binary matrices describing the fault severity levels, which can be determined by the maintenance experience. As for B_i, the corresponding binary bits are defined in **Table 1**.

For the single fault, **Table 1** summarizes the number of potential classes is 32. Since the real fault that occurred is limited, the constructed fault coding matrix will cover 160 classes that can satisfy fault attribute transfer with various levels.

As mentioned before, the key to coding is to determine the attributes of newly extracted features only by these bases. Then, the fault feature-based agile diagnosis problem is naturally done in a classification way that transfers from training faults to target faults [13].

2.4 Gray wolf optimization algorithm

The gray wolf optimization algorithm simulates the behaviors of searching and tracking, encircling and attacking the prey based on the cooperative behavior of the gray wolf pack to achieve the purpose of optimal solution. The details are as follows:

Step 1: Social hierarchy. The gray wolf population has an extremely strict social dominance hierarchy, according to which the gray wolves can be divided into four classes, from high to low, namely α, β, δ and μ. α, β, δ are the three wolves with the best adaptation in the pack, and the remaining gray wolves are μ. The pursuit is launched by α, β, δ to perform a prey tracking roundup, and the location of the prey corresponds to the optimal global solution of the SVM parameter optimization problem.

Step 2: Surrounding the prey. When searching for prey, the gray wolf will gradually approach and then encircle, and this behavior can be expressed as:

$$
\begin{cases}
D = \left| Z \cdot X_p(\tau) - X(\tau) \right| \\
X(\tau + 1) = X_p(\tau) - A \cdot D \\
A = 2a \cdot r_1 - a \\
Z = 2 \cdot r_2
\end{cases}
\tag{4}
$$

where τ is the number of iterations, A, Z is the coefficient vectors, X_p is the position vector of the prey, X is the position vector of a gray wolf, and r_1, r_2 are random vectors in [0,1]. The value of the convergence factor a is linearly decreased from 2 to 0 as follows:

0–20%	20–30%	30–40%	40–50%	50–60%
b1	b2	b3	b4	b5

Table 1.
Binary code for fault severity levels.

$$a = 2 - 2 \cdot \frac{\tau}{T} \tag{5}$$

where T is the maximum number of iterations.

Step 3: Hunting. After encircling the prey, wolves β and δ will hunt under the leadership of wolf α. In order to simulate hunting behavior, it is assumed that α, β, δ have a better understanding of the potential location of the prey. The formula is expressed as follows:

$$\begin{cases} D_\alpha(\tau) = |Z_1 \cdot X_\alpha(\tau) - X(\tau)| \\ D_\beta(\tau) = |Z_2 \cdot X_\beta(\tau) - X(\tau)| \\ D_\delta(\tau) = |Z_3 \cdot X_\delta(\tau) - X(\tau)| \end{cases} \tag{6}$$

$$\begin{cases} X_1(\tau) = X_\alpha(\tau) - A_1 \cdot (D_\alpha(\tau)) \\ X_2(\tau) = X_\beta(\tau) - A_2 \cdot (D_\beta(\tau)) \\ X_3(\tau) = X_\delta(\tau) - A_3 \cdot (D_\delta(\tau)) \end{cases} \tag{7}$$

$$X(\tau + 1) = \frac{X_1(\tau) + X_2(\tau) + X_3(\tau)}{3} \tag{8}$$

where $D_\alpha, D_\beta, D_\delta$ denotes the distance between α, β, δ and other individuals, respectively, Z_1, Z_2, Z_3 are random vectors, $X_\alpha, X_\beta, X_\delta$ denotes the current position of α, β, δ, $X(\tau + 1)$ is the optimal solution for the current iteration.

2.5 Improved gray wolf optimization algorithm

2.5.1 Initialization strategy based on chaotic tent mapping

The traditional gray wolf algorithm solves optimization problems often based on randomness to generate initial populations, which makes the initial populations unevenly distributed and leads to a reduced speed of finding the best. In contrast, chaotic motion has the properties of randomness, regularity and ergodicity, and using these advantages can generate a better diversity of initial populations and improve the global search ability of the algorithm. The Tent mapping is as follows:

$$x_t + 1 = \begin{cases} 2x_t, 0 \leq x_t \leq 0.5 \\ 2(1 - x_t), 0.5 < x_t \leq 1 \end{cases} \tag{9}$$

where x_t, x_{t+1} denotes the position of the tth and $(t + 1)^{th}$ gray wolves in the one-dimensional space individual.

2.5.2 Adaptive adjustment strategy for control parameters

The implementation of the gray wolf algorithm mainly lies in prey localization and wolf pack movement, and the position update of individual gray wolves is influenced by the parameters. When $|A| < 1$, the wolf pack narrows the search range and conducts local search, and when $|A| > 1$, the wolf pack expands the search range and conducts global search to find a better preferred solution. The value of A in turn varies with the convergence factor a, which can balance the global and local search ability for the gray wolf algorithm. In the traditional gray wolf

optimization algorithm. Meanwhile, the parameter *a* varies using a linear adjustment strategy, which ignores the diversity of optimization problems to be solved and makes it difficult to reach the global optimum. In this chapter, the new convergence factor *a* that varies nonlinearly with the number of iterations can be described as follows:

$$a(t) = (a_{\text{initial}} - a_{\text{final}}) \cdot \left(\frac{T - \tau}{T}\right)^{\ell} \tag{10}$$

where a_{initial} is 2, a_{final} is 0, τ is the current number of iterations, T is the maximum number of iterations, ℓ is the nonlinear adjustment coefficient. In this chapter, ℓ is chosen as 0.2. At the beginning of the iteration, the *a* value can be reduced more slowly to increase the search range, and at the end of the iteration, the *a* value can be reduced faster to increase the convergence speed of the algorithm.

2.5.3 Inertia weight position update

As can be seen from Eq. (7), the traditional gray wolf algorithm position update mechanism lacks weights related to the number of iterations and is prone to fall into local optimum. In this paper, a new gray wolf position updating formula based on inertia weights, which empowers the gray wolf to jump out of local extremes, as follows:

$$\kappa(\tau) = \kappa_{\max} - (\kappa_{\max} - \kappa_{\min}) \cdot \frac{\tau}{T} \tag{11}$$

where κ is the inertia weight; $\kappa_{\max}$ denotes the maximum value of inertia weight, generally taken as 0.9; $\kappa_{\min}$ denotes the minimum value of inertia weight, generally chosen as 0.4.

2.5.4 Agile fault classification with IGWO-SVM model

For the confidence evaluation, the training sample and the test sample are constructed in the same weight. In the stage of fault classification, the tent chaotic mapping, nonlinear convergence factor and dynamic inertia weight are applied to improve GWO performances. Then, the training set will be utilized to train the SVM model. Through agile parameter optimization by IGWO, the best SVM parameter for the optimal model can be achieved.

Different from the extensively used fitness evaluated with the training set, a novel SVM classification accuracy focusing on the test set is selected to satisfy the agile diagnosis, as depicted by

$$\Gamma = \frac{1}{m} \sum_{n=1}^{m} \left(\frac{l_m}{l_n} \times 100\%\right) \tag{12}$$

where *m* is the number of fault class in the test set, l_m is the number of correctly identified faults in the nth test set, and l_n is the total number of samples. The optimal parameters will be utilized to build the agile fault diagnosis model.

3. Application of the proposed method

In order to verify the effectiveness of the proposed agile fault diagnosis strategy, the comparative experiments conducted on a semiphysical platform of HST traction system in CRRC Zhuzhou Locomotive Company Ltd. (see [14, 15]), are presented in this section. The fault injection benchmark platform shown in **Figure 3** includes a traction control unit, a dSPACE real-time simulator, a signal conditioner, a power source, a host computer and an operation platform.

3.1 Multiple fault injections

To obtain the validation data sets, four kinds of faults with various severity levels are injected to the dSPACE Control Desk. For the unified modeling regarding to the
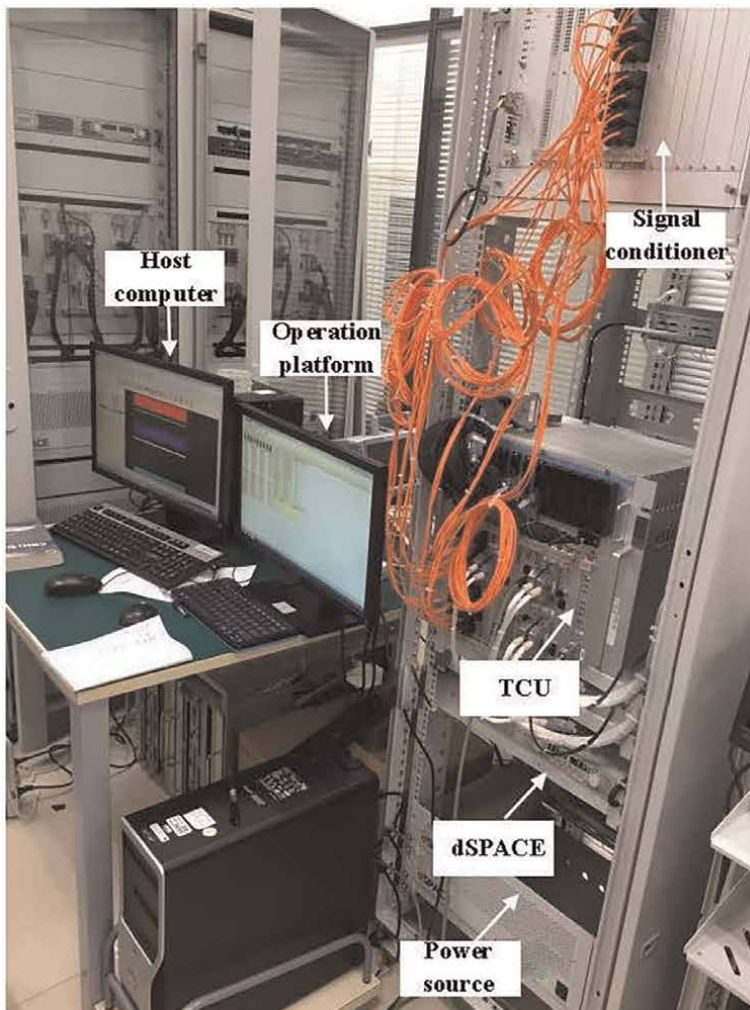
Figure 3.
HST traction system experimental setup for agile fault diagnosis.

normal and fault conditions, the experiments are executed under the steady-operation speed 110 km/h. Based on the motor model in [16], the electromagnetic torque signal sensitive to the faults can be easily reconstructed with the measurable weak current and speed signal. Considering the agile diagnosis requirements, the sampling frequency is 200 μs and the simulation time is 1 s. In order to explore the torque dynamics with various severity levels, **Figures 4–8** show the fault scenarios with a 50% ratio injecting at 0.6 s. From **Figures 4–8**, the incipient faults can be agilely detected after the fault injections, which means the torque signal is suitable for fault feature extraction and keeps consistent with the theoretical description in [17, 18].

3.2 Fault feature extraction

Based on the fault severity attribute knowledge in terms of (20–30%, 30–40%, 40–50%, and 50–60%), each group contains 5000 samples. To test the robustness of the proposed fault coding based attribute transfer method, 60 coding groups of train/test split have been collected. Then, EMD and IMF energy entropy are utilized to determine the fault feature set. By testing a large amount of the torque signal data, the
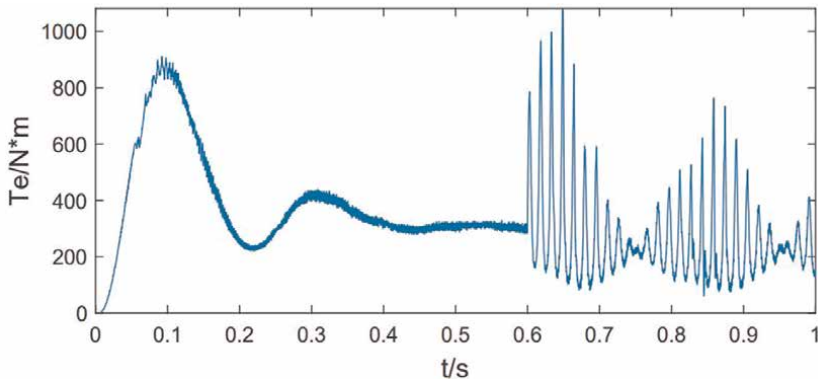
Figure 4.
Bearing fault dynamics with the electromagnetic torque signal.
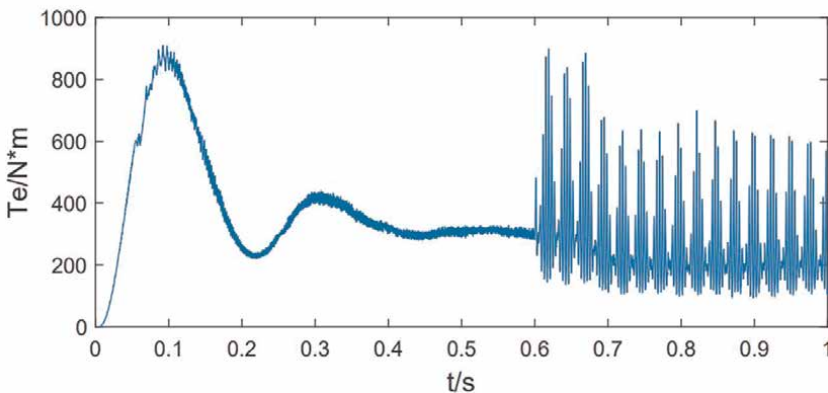
Figure 5.
Rotor fault dynamics with the electromagnetic torque signal.
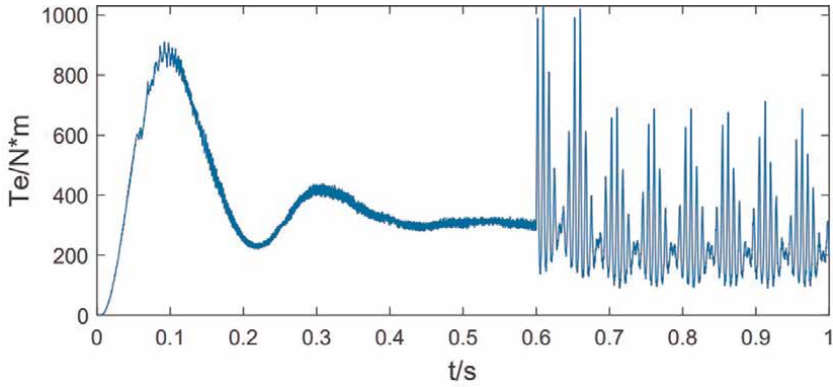
Figure 6.
Stator fault dynamics with the electromagnetic torque signal.
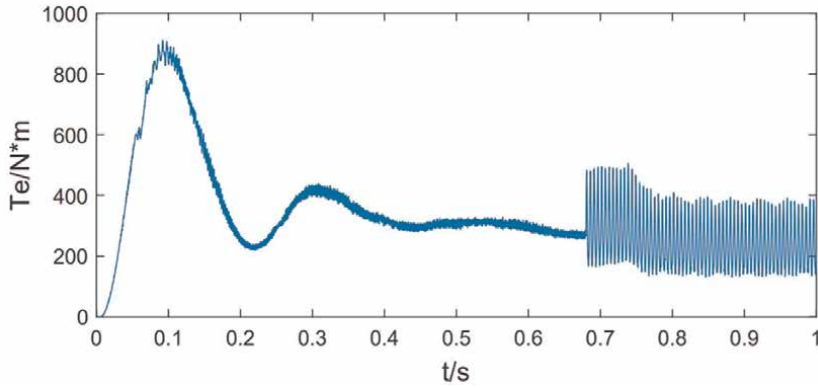
Figure 7.
Air-gap fault dynamics with the electromagnetic torque signal.
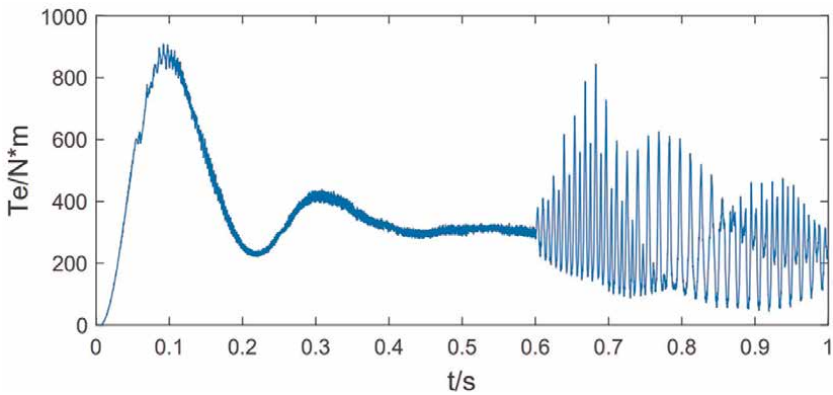
Figure 8.
Rotor and stator fault dynamics with the electromagnetic torque signal.
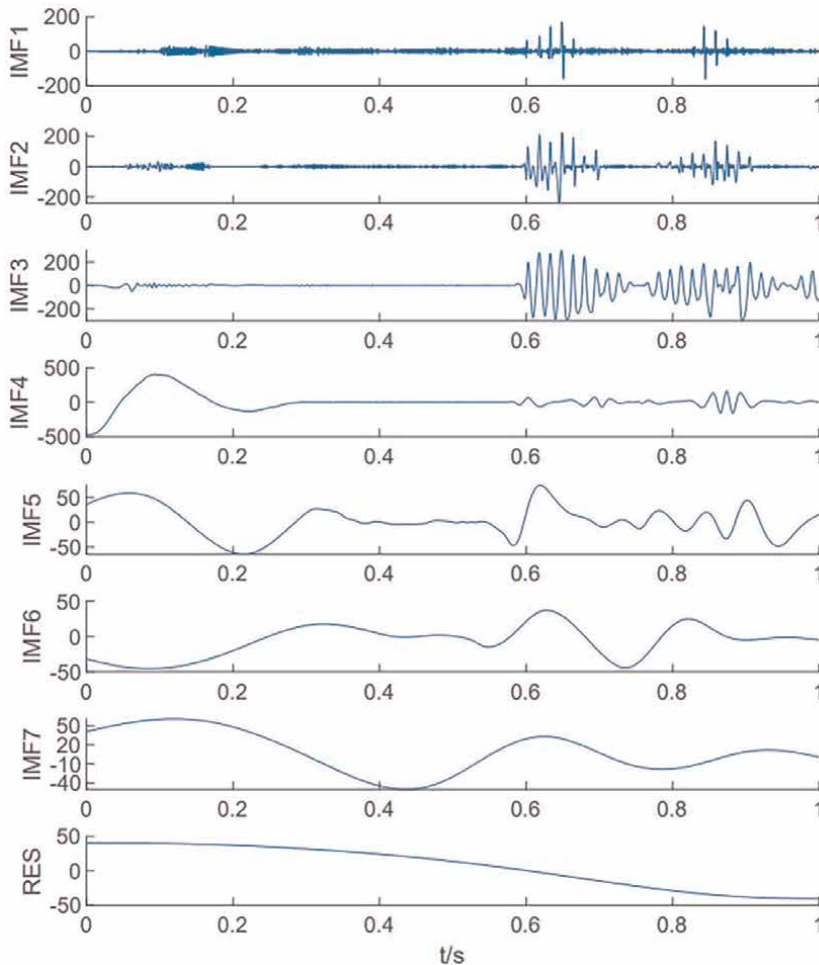
Figure 9.
The EMD of Air-gap fault signal.

default components are seven. As an example, the EMD for the electromagnetic torque signal corresponding to the air gap eccentricity fault is shown in **Figure 9**. Compared with the original signal in **Figure 4**, it can be observed that the signal part mostly lies in the first five IMFs and the dominant part of the noise exist in the sixth and seventh IMFs. Based on the coding scheme, the first five IMFs are provided in **Table 2**. **Table 2** shows that these encoded feature matrix dynamics are consistent with the fault attribute knowledge in **Table 1**. As a result, the fault attribute transfer can be achieved.

To explore the feasibility of the sharing of attribute learners, 30 coded groups in each fault mode are randomly selected to train the SVM model, and the remaining 30 groups for each fault category are treated as the test data. For the training and testing of the SVM model, fault type 1 represents the normal state while the 2, 3, 4, 5 and 6 indicate air gap eccentricity fault, stator interturn short circuit fault, broken rotor bars fault, bearing fault and compound fault, respectively. The test samples are stored in the following order: 1–30 for the normal state (label 1), 31–60 for the air gap

Motor health state	Sample Sequence	Energy entropy				
		IMF1	IMF2	IMF3	IMF4	IMF5
Normal state	1	0.00837	0.01004	0.00363	0.00277	0.36240
	2	0.00834	0.00970	0.00352	0.00260	0.36208
	...	...	...	...	...	...
	60	0.00773	0.00912	0.00313	0.00263	0.36198
Air gap eccentricity	1	0.00753	0.00878	0.02491	0.09594	0.36676
	2	0.01012	0.01168	0.03919	0.12453	0.36705
	...	...	...	...	...	...
	60	0.00333	0.32529	0.17302	0.17338	0.04985
Stator interturn short circuit fault	1	0.00991	0.11932	0.02042	0.00462	0.36679
	2	0.00836	0.12255	0.01845	0.00425	0.36672
	...	...	...	...	...	...
	60	0.00844	0.22382	0.02367	0.01362	0.36727
Broken rotor bars fault	1	0.00791	0.18749	0.34343	0.07127	0.23441
	2	0.00738	0.08977	0.28331	0.00895	0.35132
	...	...	...	...	...	...
	60	0.01037	0.21487	0.33645	0.09916	0.21056
Bearing fault	1	0.00692	0.14336	0.07425	0.00292	0.36780
	2	0.00916	0.01549	0.09111	0.00327	0.36510
	...	...	...	...	...	...
	60	0.00895	0.08748	0.12520	0.00325	0.36776
Compound faults	1	0.00723	0.01325	0.18894	0.14821	0.36479
	2	0.00908	0.02352	0.25020	0.14173	0.35896
	...	...	...	...	...	...
	60	0.00891	0.01269	0.17194	0.09948	0.36788

Table 2.
Energy entropy with various fault types.

eccentricity fault (label 2), 61–90 for the stator interturn short circuit fault (label 3), 91–120 for the broken rotor bars fault (label 4), 121–150 for the bearing fault (label 5) and 151–180 for the compound fault (label 6).

3.3 Agile fault classification

In order to achieve the agile fault classification, the comparative optimizers of GWO, particle swarm algorithm (PSO), enetic algorithm (GA) and IGWO have been employed for parameter optimization of the SVM prediction model. The four optimizer parameters are set to a population size of 20 and a number of iterations of 100. Then, the range of the SVM model parameters is set to [0.01, 100].

The four algorithms were trained with the SVM model under the training set while the test set classification accuracy (12) was used as the optimization target, and the optimal parameters obtained are shown in **Table 3**, and the adaptation curves are shown in **Figure 10**. As can be seen from **Table 3** and **Figure 10**, the fitness values corresponding to the IGWO optimized SVM parameters reach their maximum values earlier than those of GWO, PSO and GA, and the test set fault identification rate obtained by IGWO is higher than that of GWO, PSO and GA, indicating that IGWO can obtain the optimal SVM parameters quickly and accurately in the search domain than GWO, PSO and GA. In terms of convergence effect, the PSO and GA optimization algorithms obtain optimal results around 66 and 45 generations, respectively, and converge more slowly than the GWO and IGWO optimization algorithms. Comparing the GWO optimization algorithm, we can see that the IGWO and GWO algorithms have faster convergence speed, but the GWO algorithm is easy to fall into local

Diagnostic model	Best C parameter	Best σ parameter	Diagnostic accuracy
IGWO-SVM	36.78	0.227	98.89%
GWO-SVM	17.09	0.3804	98.33%
PSO-SVM	8.573	0.58	96.67%
GA-SVM	17.066	4.5231	95%

Table 3.
Parameter optimization results and fault identification rate.
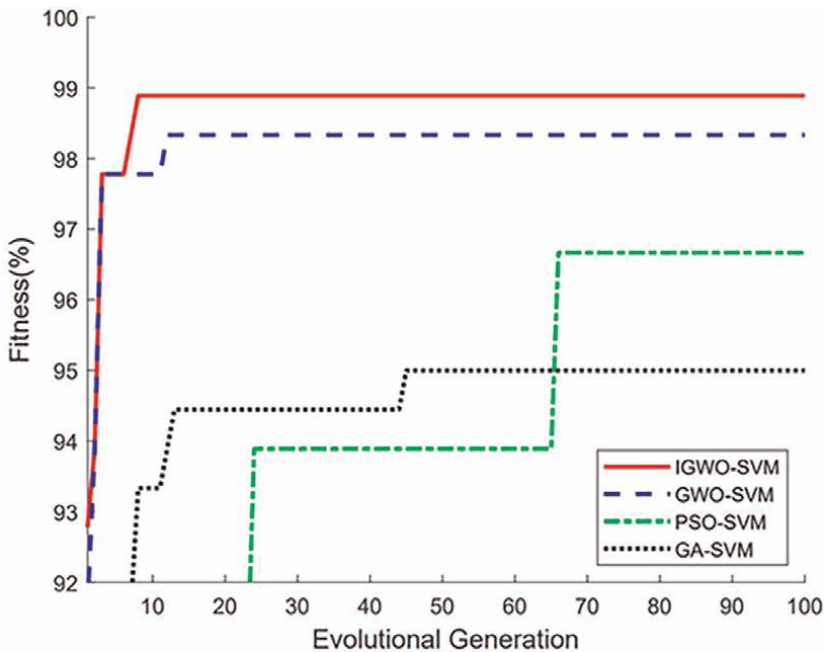
Figure 10.
Fitness curves of IGWO-SVM, GWO-SVM, PSO-SVM and GA-SVM parameter optimization process.

optimum. In summary, the IGWO-SVM classification model outperforms the other three classification models both in terms of fault recognition rate, adaptation and convergence speed.

The results of the IGWO-SVM classification model, GWO-SVM classification model, PSO-SVM classification model and GA-SVM classification model for the identification of five types of faults and normal states of the traction motor are shown in **Figures 11**–**14**. The hollow circle *o* indicates the actual fault category, + indicates the predicted fault category, and if the two overlap, the prediction is accurate; if not, the prediction is wrong. In the comparison experimental results, the GA-SVM classification model identified 171 groups out of 180 test samples, with an overall recognition rate of 95%, but 1 sample of category 3 (stator interturn short circuit fault) were incorrectly classified into category 2(air gap eccentricity fault), with a false alarm rate of 3.33%; 8 samples of category 6 (Coupled faults) was incorrectly classified into category 2 (air gap eccentricity fault), with a false alarm rate of 26.67%; From the above analysis, it can be seen that although GA-SVM has a high fault recognition rate, it is difficult to meet the requirement of less than 10% false alarm rate of high-speed train traction system in terms of local fault diagnosis.

The PSO-SVM classification model identified 176 groups in 180 test samples, with an overall recognition rate of 97.2%, but 1 sample of category 4 (broken rotor bars fault) was incorrectly classified into category 6(compound faults), with a false alarm rate of 3.33%; 1 sample of category 5 (bearing fault) was incorrectly classified into category 3 (stator interturn short circuit fault), with a false alarm rate of 3.33%; 4 samples of category 6 (coupled faults) was incorrectly classified into category 2 (air gap eccentricity fault), with a false alarm rate of 10%. From the comparative analysis results, it can be seen that PSO-SVM has a higher overall recognition rate compared to
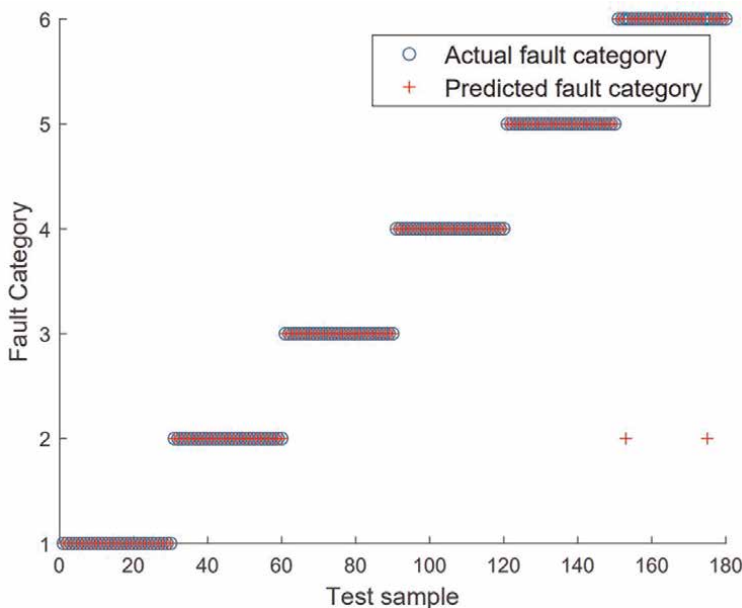
Figure 11.
Fault diagnosis result in IGWO-SVM.
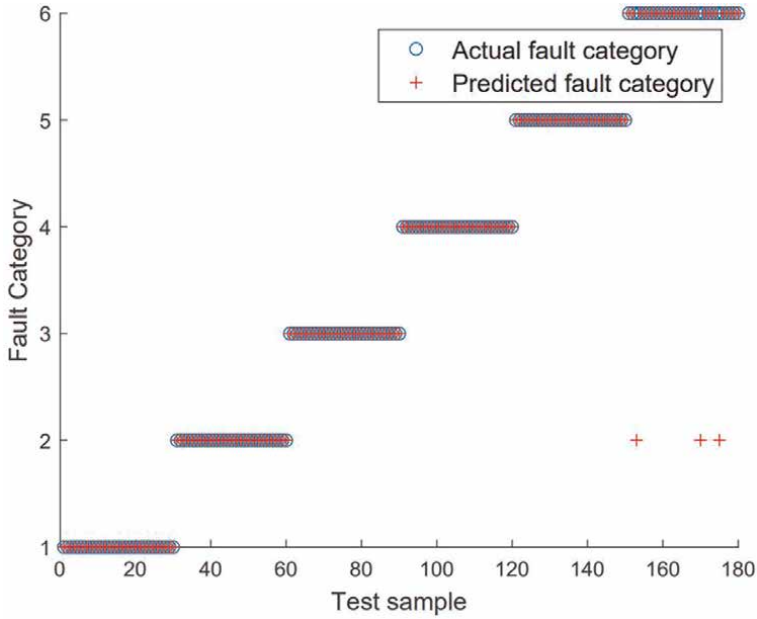
Figure 12.
Fault diagnosis result in GWO-SVM.
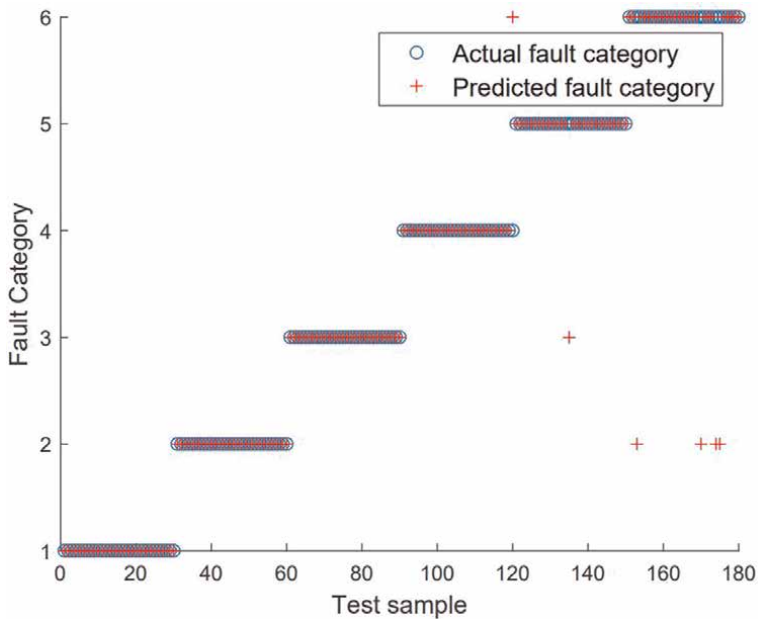
Figure 13.
Fault diagnosis result in PSO-SVM.

GA-SVM, but it is difficult to meet the requirement of less than 10% false alarm rate for high-speed train traction system faults in local fault diagnosis, especially compound faults.
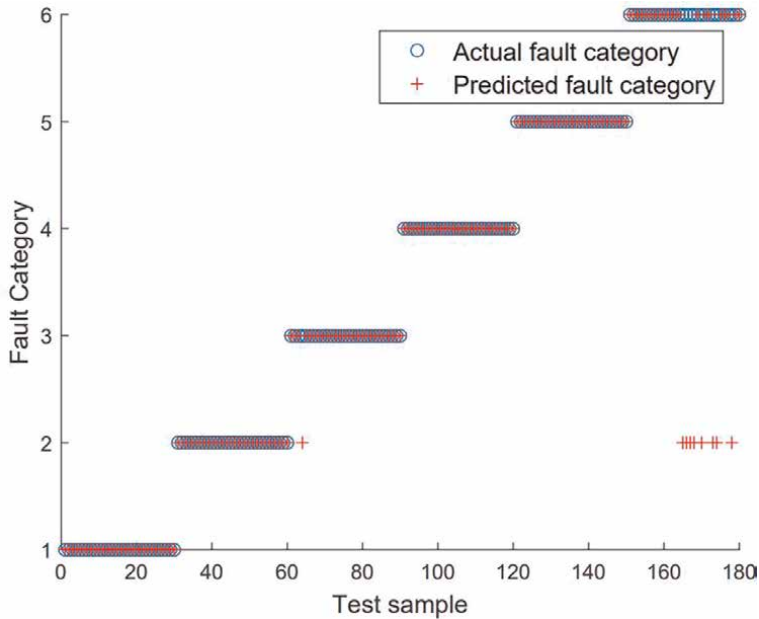
Figure 14.
Fault diagnosis result in GA-SVM.

The GWO-SVM classification model identified 177 groups out of 180 test samples, with an overall recognition rate of 98.33%. However, 1 sample of category 6 (Coupled faults) was incorrectly classified into category 2(air gap eccentricity fault), with a false alarm rate of 10%. Compared with GA-SVM and PSO-SVM, GWO-SVM has a higher overall recognition rate and also meets the requirement of less than 10% false alarm rate for high-speed train traction systems but increases the probability of misclassification of fault samples.

The SVM classification model optimized by IGWO identified 178 groups out of 180 test samples, with an overall recognition rate of 98.89%. The model only had two samples incorrectly classified into category 2 (air gap eccentricity fault) in category 6 (coupled faults), with a false alarm rate of 6.67%. The classification model proposed in this paper not only meets the requirement of less than 10% false alarm rate of high-speed train traction systems but also avoids increasing the probability of misclassification of fault samples.

4. Conclusion

1. This paper adopts a resilience enhancement strategies based on the fault severity modeling, entropy coding of electromagnetic torque energy, support vector machine classification model, and optimized fusion of improved gray wolf algorithm, which is more accurate in distinguishing small fault features and improving multi-fault diagnosis accuracy compared with other schemes.

2. Through the experiments on the data set of semiphysical simulation platform of high-speed train traction system, the results show that the proposed scheme has

certain guiding significance for traction motor fault feature extraction and accurate localization.

3. The proposed scheme can effectively diagnose the multiple fault modes of traction motors of high-speed trains and can also be applied to the identification of other equipment fault types of high-speed trains.

Author details

Kunpeng Zhang[1*], Bin Jiang[2], Fuyang Chen[2] and Hui Yang[1]

1 School of Electrical and Automation Engineering, East China Jiaotong University, Nanchang, China

2 College of Automation Engineering, Nanjing University of Aeronautics and Astronautics, Nanjing, China

*Address all correspondence to: ecjtu.zhangkunpeng@163.com

IntechOpen

References

[1] Chen HT, Jiang B, Li ZH. Edge computing-aided framework of fault detection for traction control systems in high-speed trains. IEEE Transactions on Vehicular Technology. 2020;**69**(2): 1309-1318. DOI: 10.1109/TVT. 2019.2957692

[2] Kim Y, Koo B, Nam K. Induction motor design strategy for wide constant power speed range. IEEE Transactions on Industrial Electronics. 2019;**66**(11): 8372-8381. DOI: 10.1109/ TIE.2018.2885691

[3] Yang CH, Yang C, Yang XY, Gui WH. A fault-injection strategy for traction drive control systems. IEEE Transactions on Industrial Electronics. 2017;**64**(7): 5719-5727. DOI: 10.1109/TIE.2017. 2674610

[4] Zhou DH, Ji HQ, He X, Shang J. Fault detection and isolation of the brake cylinder system for electric multiple units. IEEE Transactions on Control Systems Technology. 2018;**26**(5): 1744-1757. DOI: 10.1109/ TCST.2017.2718979

[5] Prakash O, Samantaray AK, Bhattacharyya R. Model-based diagnosis of multiple faults in hybrid dynamical systems with dynamically updated parameters. IEEE Transactions on Systems, Man, and Cybernetics:Systems. 2019;**49**(6):1053-1072. DOI: 10.1109/ TSMC.2017.2710143

[6] Singh A, Grant B, Defour R, Sharma C, Bahadoorsingh S. A review of induction motor fault modeling. Electric Power Systems Research. 2016;**133**: 191-197. DOI: 10.1016/j.epsr.2015.12.017

[7] Yu WK, Zhao CH. Online fault diagnosis in industrial processes using multimodel exponential discriminant

analysis algorithm. IEEE Transactions on Control Systems Technology. 2019; **27**(3):1317-1325. DOI: 10.1109/ TCST.2017.2789188

[8] Wang F, Xu TH, Tang T, Zhou MC, Wang HF. Bilevel feature extraction-based text mining for fault diagnosis of railway systems. IEEE Transactions on Intelligent Transportation Systems. 2017; **18**(1):49-58. DOI: 10.1109/TITS. 2016.2521866

[9] Wang S, Minku L, Yao X. A systematic study of online class imbalance learning with concept drift. IEEE Transactions on Neural Networks and Learning Systems. 2018;**29**(10): 4802-4821. DOI: 10.1109/ TNNLS.2017.2771290

[10] Zhang KP, Jiang B, Tao G, Chen FY. MIMO evolution model based coupled fault estimation and adaptive control with high speed train applications. IEEE Transactions on Control Systems Technology. 2018;**26**(5):1552-1566. DOI: 10.1109/TCST.2017.2735360

[11] Nguyen V, Wang DW, Seshadrinath J, Ukil K, Krishna MS, Nadarajan S, et al. A method for incipient interturn fault detection and severity estimation of induction motors under inherent asymmetry and voltage imbalance. IEEE Transactions on Transportation Electrification. 2017; **3**(3):703-715. DOI: 10.1109/TTE. 2017.2726351

[12] Pandey VK, Kar I, Mahanta C. Controller design for a class of nonlinear MIMO coupled system using multiple models and second level adaptation. IEEE Transactions on Transportation Electrification. 2017;**69**:256-272. DOI: 10.1016/j. jsatra2017.05.005

[13] Bethoux O, Laboure E, Remy G, Berthelot E. Real-time optimal control of a 3-phase PMSM in 2-phase degraded mode. IEEE Transactions on Vehicular Technology. 2017;**66**(3):2044-2052. DOI: 10.1109/TVT.2016.2583662

[14] Zhang KP, Jiang B, Chen FY. Multiple-model-based diagnosis of multiple faults with high-speed train applications using second-level adaptation. IEEE Transactions on Industrial Electronics. 2021;**68**(7): 6257-6266. DOI: 10.1109/TIE.2020. 2994867

[15] Gao ZW, Liu XX, Chen MZQ. Unknown input observer-based robust fault estimation for systems corrupted by partially decoupled disturbances. IEEE Transactions on Industrial Electronics. 2016;**63**(4):2537-2547. DOI: 10.1109/2015.2497201

[16] Yang ML, Deng C, Nie FP. Adaptive-weighting discriminative regression for multi-view classification. Pattern Recognition. 2019;**88**:236-245. DOI: 10.1016/j.patcog.2018.11.015

[17] Mustafa MO, Nikolakopoulous G, Gustafsson T, Kominiak D. A fault detection scheme based on minimum identified uncertainty bounds violation for broken rotor bars in induction motors. Control Engineering Practice. 2016;**48**:63-77. DOI: 10.1016/ j.conengprac.2015.12.008

[18] Davies DL, Bouldin DW. Cluster separation measure. IEEE Transactions on Pattern Analysis and Machine Intelligence. 1979;**1**(2):224-227

Section 4

Nuclear-Powered Propulsion

Nuclear Propulsion

Bahram Nassersharif and Dale Thomas

Abstract

Nuclear propulsion utilizes nuclear reactions to produce energy, which is then used to propel a vehicle. There are three main forms of nuclear propulsion: naval nuclear propulsion, aero-nuclear propulsion, and space nuclear propulsion. Naval nuclear propulsion involves the use of nuclear reactors to power ships. This propulsion type provides several advantages over traditional propulsion methods, including increased range, speed, and maneuverability. The first nuclear-powered submarine, the USS Nautilus, was commissioned in 1955, and since then, many countries have developed nuclear-powered submarines and ships. Aero-nuclear propulsion involves the use of nuclear reactors to power aircraft or missiles. This concept has been the subject of much research and development. Space nuclear propulsion involves the use of nuclear reactors to power spacecraft. This type of propulsion provides several advantages over traditional propulsion methods, including increased speed and efficiency. The main challenge with space nuclear propulsion is developing extremely high-temperature reactors.

1. Introduction

The history of nuclear propulsion can be traced back to the mid-twentieth century when the development of the atomic bomb and the dawn of the nuclear age sparked a new era of technological innovation and exploration. As the world rapidly discovered nuclear technology's tremendous power and potential, scientists and engineers began exploring new ways to harness this power for practical applications.

One of the earliest and most promising applications of nuclear technology was nuclear propulsion, which offered the potential to revolutionize space travel, naval operations, and air transportation. The first experimental reactors for nuclear propulsion were developed in the late 1940s and early 1950s. By the mid-1950s, the United States had launched the first nuclear-powered submarines, the USS Nautilus and the USS Seawolf [1].

The development of nuclear propulsion was driven by several critical factors, including the increasing demand for longer-range and more capable vessels, the growing interest in space exploration, and the need for a more efficient and reliable power source. Nuclear propulsion offers several key advantages over conventional propulsion systems, including higher energy density, greater operational efficiency, and reduced dependence on fuel resupply.

IntechOpen

Despite its many benefits, nuclear propulsion also posed significant challenges and risks, including the need for safe and reliable power sources, effective shielding to protect against radiation exposure, and rigorous regulatory and licensing processes. These challenges led to the development of new technologies and processes for designing and operating nuclear propulsion systems. By the end of the twentieth century, nuclear propulsion had become a critical component of many military and space programs.

Today, nuclear propulsion plays a critical role in naval operations. Nuclear propulsion will play an essential role in space travel in the near future. Aero-nuclear propulsion continues to evolve and improve as new technologies and processes are developed. While the use of nuclear propulsion is still subject to challenges and risks, it remains one of the most promising and innovative applications of nuclear technology. It will likely continue to play a critical role in the world's technological and scientific advancement for many years to come.

2. Naval nuclear propulsion

Naval nuclear propulsion refers to using nuclear reactors to power ships and submarines. Nuclear propulsion provides several advantages over conventional propulsion systems, including greater range, faster speeds, and reduced dependence on refueling.

Admiral Hyman G. Rickover played a crucial role in establishing the US nuclear navy. He was a naval engineer who saw the potential of nuclear power as a means of propulsion for ships. He pushed for and oversaw the development of the first nuclear-powered submarine, the USS Nautilus, which became operational in 1954. Rickover's tireless work and leadership led to the widespread adoption of nuclear power in the US Navy, making it the world's first nuclear navy and establishing the US as a leader in naval technology. He was known for his uncompromising standards and attention to detail, which helped ensure nuclear-powered vessels' safe and reliable operation [1].

Naval nuclear reactors are similar in design to land-based reactors, but they must be highly compact and rugged to withstand the harsh conditions of maritime operations. The reactors use enriched uranium fuel rods to generate heat, producing steam that drives turbines and propellers. Unlike conventional diesel-electric propulsion systems, nuclear reactors do not require air to generate power, making them ideal for use in submarines that can remain underwater for extended periods.

The use of nuclear propulsion in the military is highly regulated and subject to strict safety and security standards. In addition, nuclear propulsion systems must be designed to withstand the impact of an enemy attack and to prevent the release of radioactive material in the event of an accident.

Many navies, including the United States and several other countries, have widely adopted naval nuclear propulsion. Nuclear propulsion has enabled these navies to maintain a strong and flexible presence at sea and respond to a wide range of military and humanitarian missions.

3. Aero nuclear propulsion

Aero nuclear propulsion refers to using nuclear reactors or radioisotope thermo-electric generators (RTGs) to power aircraft. While the use of nuclear power for

aircraft propulsion has been researched for many years, it has never been widely adopted due to technical, regulatory, and public acceptance challenges.

In aero-nuclear propulsion, a nuclear reactor would be used to generate electricity, which could be used to electric power motors that drive the aircraft's propellers or turbines. Alternatively, an RTG or NTP could be used to provide a direct heat source, which could produce high-speed exhaust to provide thrust.

The main advantage of aero-nuclear propulsion is that it offers a much higher energy density than conventional fuel sources, allowing for longer flight times and greater range. However, the use of nuclear power in aircraft also presents several challenges, including the need for a highly reliable and safe power source, effective shielding to protect against radiation exposure, and rigorous regulatory and licensing processes.

Despite these challenges, the concept of aero-nuclear propulsion continues to attract interest from researchers and military organizations, who see it as a potential solution to meet the growing demand for longer-range, higher-performance aircraft or missiles.

Aero nuclear propulsion can be combined with ramjet or scramjet technologies to increase thrust and specific impulse [2]. Ramjet and scramjet are two types of air-breathing propulsion systems that have the potential to revolutionize space and high-speed flight. Unlike traditional rocket propulsion systems that carry both fuel and oxidizer, ramjets and scramjets rely on the atmospheric air for oxygen, allowing them to be much lighter and more efficient [3].

3.1 Ramjet propulsion

A ramjet is a type of air-breathing propulsion system that uses the vehicle's motion to compress incoming air, which is then mixed with fuel and burned to produce hot gases that are expelled through a nozzle to produce thrust. Ramjets are characterized by their simplicity and high performance at high speeds, making them well-suited for high-speed flight and space applications. The thrust of a ramjet is given by:

$$T = \dot{m}v_e, \qquad (1)$$

where T is the thrust, $\dot{m}$ is the mass flow rate of the propellant, and v_e is the exhaust velocity.

Ramjets are limited by their performance at low speeds, as they rely on the motion of the vehicle to compress the incoming air. To overcome this limitation, a ramjet can be combined with a conventional rocket propulsion system, allowing the vehicle to take off from a standstill and then transition to ramjet propulsion once it reaches high speeds [2].

3.2 Scramjet propulsion

A scramjet is a type of air-breathing propulsion system that is similar to a ramjet but operates at hypersonic speeds, typically above Mach 5. Unlike a ramjet, a scramjet uses shockwaves generated by the incoming air to compress and mix the air with fuel, allowing it to operate at much higher speeds than a ramjet. The thrust of a scramjet is given by the same formula as a ramjet.

Scramjets are well suited for high-speed flight and space applications, as they can provide high performance at hypersonic speeds with a relatively simple design.

However, the development of scramjet technology is challenging, as it requires a deep understanding of high-speed aerodynamics and the ability to control and stabilize supersonic combustion [3].

4. Space nuclear propulsion

Space nuclear propulsion refers to using nuclear fission reactors or radioisotope decay to provide power for spacecraft propulsion and other space missions. Unlike conventional chemical propulsion systems, nuclear propulsion systems provide a much higher energy density, allowing faster, more efficient travel through space. There are two main types of space nuclear propulsion: nuclear thermal propulsion (NTP) and nuclear electric propulsion (NEP).

In NTP, a nuclear reactor is used to heat a propellant, such as hydrogen, to high temperatures, creating a high-speed exhaust that provides thrust. NTP offers higher thrust levels and specific impulses (a measure of propulsion efficiency) than conventional chemical propulsion systems. Although operational lifetime requirements are typically low (a few hours), the need for very high temperature (>2500 K) fuel and very high power density (>1 MW/L) for operational systems add design complexity.

On the other hand, NEP uses the electricity generated by a nuclear reactor or RTG to power an electric thruster (e.g., ion, Hall, MPD, VASIMR), which uses charged particles to produce thrust. NEP systems produce much lower thrust than NTP systems but are very efficient and well-suited for certain missions. Early NEP systems in the 10 kWe range may be well suited for deep space science missions, and advanced NEP systems in the 10 MWe range may enable fast (< 1 year) round-trip human Mars missions. NEP is less complex than NTP and offers high specific impulses but lower thrust levels. A primary challenge for NEP systems is ensuring that the specific mass (mass of integrated power/propulsion system divided by power into the propellant) is sufficiently low, typically <50 kg/kW, to enable deep space science missions and < 6 kg/kW to enable very fast human Mars missions.

Space nuclear propulsion has been used in a limited number of missions, including the Mars rovers, which relied on RTGs for power to turn the drive wheels. However, nuclear propulsion systems in space are still primarily limited due to technical and regulatory challenges. As of 2023, a multi-agency program is in place to demonstrate a nuclear thermal propulsion system in space.

4.1 Differences between chemical and nuclear thermal rocket propulsion

Chemical rocket propulsion and nuclear thermal propulsion are two types of rocket propulsion systems that differ in how they generate the necessary energy to produce thrust.

Chemical rocket propulsion involves chemical reactions between fuels and oxidizers to generate hot gases that are expelled through a nozzle to produce thrust. Two commonly used propellants in chemical rocket propulsion are liquid hydrogen and liquid oxygen, which produce high-speed exhaust gases with a high specific impulse

(a measure of propellant efficiency). The mathematical formula for the rocket equation, which describes the change in velocity of a rocket, is given by:

$$\Delta v = v_e Ln\left(\frac{m_0}{m_f}\right), \tag{2}$$

where Δv is the change in velocity, v_e is the exhaust velocity, m_0 is the initial mass of the rocket, and m_f is the final mass of the rocket.

On the other hand, nuclear thermal propulsion involves using a nuclear reactor to heat a propellant, which is then expelled through a nozzle to produce thrust. The main advantage of nuclear thermal propulsion over chemical rocket propulsion is its much higher specific impulse (a measure of propellant efficiency), which allows for much higher exhaust velocities and, thus, a much greater Δv. The mathematical formula for the specific impulse of a nuclear thermal rocket is given by:

$$I_{sp} = \frac{v_e}{g}, \tag{3}$$

where I_{sp} is the specific impulse v_e is the exhaust velocity, and g is the acceleration due to gravity.

Nuclear thermal propulsion systems have the potential to be much more efficient than chemical rocket propulsion systems, but they also come with several challenges and limitations. For example, nuclear thermal propulsion systems require a reliable, safe, and efficient method of cooling the nuclear reactor and a means of containing and controlling the radioactive materials involved. Additionally, significant technical and regulatory challenges are associated with developing and operating nuclear thermal propulsion systems.

Chemical rocket propulsion and nuclear thermal propulsion are two different types of rocket propulsion systems that differ in how they generate the necessary energy to produce thrust. Chemical rocket propulsion relies on chemical reactions between fuels and oxidizers, while nuclear thermal propulsion relies on the heat generated by a nuclear reactor. While nuclear thermal propulsion has the potential to be much more efficient than chemical rocket propulsion, it also comes with several technical and regulatory challenges that must be overcome.

Typical values for the specific impulse of chemical propulsion rockets for Mars missions is ~400 s, whereas the tested nuclear thermal propulsion rockets are in the 850 s range. Solid-fuel nuclear thermal propulsion rockets may be able to achieve 900 s I_{sp} (with hydrogen), and liquid-fuel nuclear thermal propulsion rockets may be able to achieve 1800 s I_{sp} with hydrogen and 1000 s I_{sp} with methane [4].

5. Technology considerations for space and aero-nuclear propulsion

Nuclear reactors are an essential component of nuclear propulsion systems and play a crucial role in generating heat and power for spacecraft. Over the years, several nuclear reactor designs have been developed and tested, each with its own unique features and capabilities. Below, we will take a closer look at six of the most significant nuclear reactor designs: KIWI, N.R.X., Phoebus, PEEWEE, XE-PRIME, and NF.

KIWI (Kiwi Reactor) was a prototype nuclear reactor developed by the United States in the late 1950s. It was one of the first reactors developed specifically for use in spacecraft and was designed to be lightweight, compact, and highly efficient. KIWI used a solid core fuel design and employed a unique cooling system that used sodium as the coolant. The reactor was highly successful, and its design served as the basis for several other reactors developed later in the space program.

NRX (Nuclear Reactor Experiment) was a research reactor developed in the United States in the mid-1950s. It was used to test various reactor components and to study the behavior of materials in a nuclear environment. NRX was a small reactor that used a liquid core fuel design and was designed to be highly flexible, allowing for a wide range of experiments. The reactor was highly successful, and its design was later adapted for use in other reactors, including the KIWI and Phoebus reactors.

Phoebus (Phoebus Reactor) was a nuclear reactor developed in France in the mid-1960s. It was designed for use in space propulsion systems and was the first European reactor specifically developed for this purpose. PHOeBUS used a solid core fuel design and employed a unique cooling system that used helium as the coolant. The reactor was highly successful, and its design was later adapted for use in other reactors, including the XE-PRIME and NF reactors.

PEWEE was a small prototype reactor developed in the United States in the late 1950s. It was designed to be highly compact and lightweight and was used to test various components and materials for use in space reactors. PEEWEE used a solid core fuel design and was designed to be highly flexible, allowing for a wide range of experiments to be performed. The reactor was highly successful, and its design was later adapted for use in other reactors, including the KIWI and XE-PRIME reactors.

XE-PRIME (Experimental Prime Reactor) was a research reactor developed in the United States in the late 1960s. It was designed to test various components and materials for use in space reactors and to study materials' behavior in a nuclear environment. XE-PRIME used a liquid core fuel design and was designed to be highly flexible, allowing for a wide range of experiments to be performed. The reactor was highly successful, and its design was later adapted for use in other reactors, including the Phoebus and NF reactors.

NF (Nuclear Furnace) was a nuclear reactor developed in France in the late 1970s. It was designed for space propulsion systems and was one of the first reactors to employ a new type of fuel known as particle bed fuel. NF used a solid core fuel design and employed a unique cooling system that used helium as the coolant. The reactor was highly successful, and its design was later adapted for use in other reactors, including the PHOEBUS and XE-PRIME reactors.

These six nuclear reactor designs represent some of the most significant advancements in the field of nuclear propulsion. We describe each in further detail. **Table 1** shows the comparison of the different designs.

5.1 High-temperature materials

The core of a high-temperature nuclear reactor for nuclear thermal propulsion is where the fission reactions occur. It must be made of materials that can withstand the extremely high temperatures and radiation levels generated by these reactions. The melting point of the materials used in the reactor core is an essential factor in determining the safety and performance of the reactor. We will examine the melting points of several materials commonly used in high-temperature nuclear reactor cores. High-performance and temperature liquid-fueled systems are often proposed

Design parameter/ concept	I_{sp} (s)	Thrust (kN)	Core thermal power (MW)	Core average temperature (°C)
ENABLER	825	333	1586	2427
SMALL ENGINE	780	73	367	2361
SNRE	1000	44	210	2227
710	873	444	2010	2371
CERMET	930	445	2000	2234
PBR 1	971	334	1945	2927
PBR 2	780	33	150	2477
PeBR	1000	315	1500	2727
LPNTR 1	1075	111	525	2927
LPNTR 2	1050	48	260	2927
WIRE CORE	930	914	4400	2727

Table 1.
Key design parameters for post-NERVA conceptual NTP reactors.

that use propellant flow to keep all core structural and moderator materials at reasonable temperatures (<800 K) while still allowing molten fuel to heat the propellant to a very high temperature before expansion through a nozzle. One potential concept is the Centrifugal Nuclear Thermal Rocket (CNTR) described in [5, 6].

For traditional solid-fuel NTP engines and the structural and moderator components of liquid-fueled engines, the first material we will consider is graphite, which has been used as a moderator in some high-temperature reactors. Graphite has a high melting point of around 3600°C and is an excellent thermal conductor, making it an ideal material for high-temperature reactors. However, graphite is also highly flammable and can become highly reactive in the presence of oxygen and high temperatures, making it less attractive for air-breathing high-temperature reactors.

Another commonly used material in high-temperature reactor cores is beryllium, which has a melting point of around 1278°C. Beryllium is a good thermal conductor with a high thermal expansion coefficient, making it well-suited for high-temperature reactors.

Tungsten is another material that is sometimes used in high-temperature reactors. Tungsten has a melting point of around 3410°C, making it an ideal choice for high-temperature reactors. Tungsten is also a good thermal conductor and is highly resistant to thermal shock, making it a good choice for high-temperature reactors. However, tungsten is also a very dense material, which can make it challenging to handle and can increase the weight of the reactor. Tungsten is also a strong neutron absorber, making it difficult to use in moderated systems fueled by high assay low enriched uranium (HALEU).

Hafnium is another material that is sometimes used in high-temperature reactors. Hafnium has a high melting point of around 2227°C and is highly resistant to thermal shock, making it well-suited for high-temperature reactors. However, hafnium is a highly reactive material that can be difficult to work with and has a high neutron

absorption cross-section. Hafnium is also expensive, making it a less attractive choice for high-temperature reactors.

Molybdenum is another material that is sometimes used in high-temperature reactors. Molybdenum has a high melting point of around 2620°C and is a good thermal conductor, making it well-suited for use in high-temperature reactors. Molybdenum is also highly resistant to thermal shock, making it a good choice for use in high-temperature reactors. However, molybdenum is also a very dense material, which can make it difficult to handle and can increase the weight of the reactor.

The thermal properties of materials are critical in determining their suitability for use in high-temperature nuclear reactors. We will compare the thermal properties of five materials commonly used in high-temperature reactors: uranium dioxide (UO2), uranium carbide (UC), carbon, niobium carbide (NbC), and tungsten.

Uranium dioxide (UO2) is a commonly used fuel in nuclear reactors and has a melting point of around 2800°C. UO2 has a low thermal conductivity, meaning it does not conduct heat well and can lead to overheating in high-temperature reactors. Additionally, UO2 is highly reactive and can become unstable at high temperatures, which can pose a safety risk in high-temperature reactors [7].

Uranium carbide (UC) is a relatively new material that is being investigated for use in high-temperature reactors. UC has a high melting point of around 2900°C and higher thermal conductivity than UO2. However, UC is also highly reactive and can become unstable at high temperatures, which can pose a safety risk in high-temperature reactors [8].

Carbon is a common material used in high-temperature reactors as a moderator and reflector. Carbon has a high melting point of around 3600°C and is a good thermal conductor, making it well-suited for use in high-temperature reactors. However, carbon is also highly flammable and can become highly reactive in the presence of high temperatures, which can pose a safety risk in high-temperature reactors.

Niobium carbide (NbC) is a refractory material that is being investigated for use in high-temperature reactors. NbC has a high melting point of around 3300°C and is highly resistant to thermal shock, making it well-suited for use in high-temperature reactors. However, NbC is also a highly reactive material that can be difficult to work with, which can pose a challenge in high-temperature reactors [9].

Tungsten is another material that is commonly used in high-temperature reactors. Tungsten has a high melting point of around 3410°C and is a good thermal conductor, making it well-suited for use in high-temperature reactors. Tungsten is also highly resistant to thermal shock, making it a good choice for use in high-temperature reactors. However, tungsten is also a very dense material, which can make it difficult to handle and can increase the weight of the reactor.

In conclusion, the thermal properties of the materials used in high-temperature reactors are critical in determining their suitability for use in these reactors. Uranium dioxide, uranium carbide, carbon, niobium carbide, and tungsten all have unique thermal properties that make them suitable for different applications in high-temperature reactors. The choice of material for use in a high-temperature reactor will depend on the specific requirements of the reactor, including the desired thermal conductivity, resistance to thermal shock, and ease of handling.

The choice of material for use in a high-temperature reactor will depend on the specific requirements of the reactor, including the desired thermal conductivity, resistance to thermal shock, and ease of handling.

Table 2 shows the melting points of some high-temperature reactor materials of interest.

Application	Material	Melting temperature (°C)
Fuel	Uranium	1132
Fuel	Uranium dioxide	2865
Fuel	Uranium carbide	3900
Fuel	Uranium nitride	2000
Structures/refractory metal	Tungsten	3422
Structures/refractory metal	Molybdenum	2610
Structures/refractory metal	Rhenium	3180
Structures/refractory metal	Tantalum	2996
Structures/cladding refractory non-metal	Carbon	3600
Structures/cladding refractory non-metal	Niobium carbide	4500
Structures/cladding refractory non-metal	Zirconium carbide	3300
Structures/cladding refractory non-metal	Hafnium carbide	3900
Structures/cladding refractory non-metal	Tantalum carbide	4215

Table 2.
Melting points of some nuclear reactor materials of interest in nuclear thermal propulsion.

5.2 The ROVER program

The Rover Nuclear Rocket Engine Program was a research and development program aimed at developing a nuclear-powered rocket engine for space exploration and interplanetary missions. The program was run by the US Atomic Energy Commission (AEC) and the National Aeronautics and Space Administration (NASA) from 1955 to 1973. It was part of a larger effort to develop new technologies for space exploration [10].

The main objective of the Rover program was to develop a nuclear-powered rocket engine that could provide a high specific impulse (a measure of fuel efficiency) and high thrust, enabling spacecraft to reach high speeds and travel longer distances than was possible with chemical propulsion systems. The program was focused on developing a new type of engine, known as a nuclear thermal rocket engine, which used nuclear reactors to heat a propellant to provide thrust.

The Rover program consisted of several research and development phases, including laboratory experiments, component testing, and full-scale engine testing. During the laboratory phase, researchers conducted experiments to study the behavior of various materials and components in a nuclear environment, including the heat transfer and cooling systems, the fuel elements, and the reactor core [11].

During the component testing phase, individual components of the engine were tested to validate their performance and to identify any problems. This phase included testing the heat exchangers, the pumps, and the fuel elements.

The full-scale engine testing phase involved the development and testing of prototype engines to validate the performance of the engine and to demonstrate its feasibility. The tests were conducted at various facilities, including the Nevada Test Site and the Marshall Space Flight Center. The engines were operated at full power during these tests, and the performance was measured and analyzed.

The Rover program was highly successful and produced several important break-throughs in the field of nuclear propulsion. The program demonstrated the feasibility of nuclear thermal rocket engines and showed that they could significantly improve specific impulse and thrust over chemical propulsion systems. The program also produced a wealth of data and information on the behavior of materials and components in a nuclear environment, which has been invaluable for future research and development in this field.

However, despite its many successes, the Rover program was eventually terminated in 1973 due to a change in priorities and a shift in focus toward other areas of space exploration. The program was never fully operational, and no nuclear-powered spacecraft were ever built or flown as a result of the Rover program. **Table 3** shows the timetable of the nuclear thermal propulsion tests.

The Rover Nuclear Rocket Engine Program was a highly successful research and development program that made significant contributions to the field of nuclear propulsion. The program demonstrated the feasibility of nuclear thermal rocket engines and produced valuable data and information for future research and

Reactor	Date	Maximum power (MW$_{th}$)	Maximum runtime (s)	Net I_{sp} (s)	Exit T (°C)
KIWI-A	7/1/1959	70	300		
KIWI-A'	7/8/1960	88	307		
KIWI-A3	10/19/1960	112.5	259		
KIWI-B1A	12/7/1961	225	36		
KIWI-B1B	9/1/1962	880	Multiple		
KIWI-B4A	12/30/1962	450	Multiple		
KIWI-B4D	5/1/3/1964	990	40		
KIWI-B4E	8/28/1964	937	480		
KIWI-B4E	9/10/1964	882	150		
NRX-A2	9/24/1964	1096	40		
NRX-A3	4/23/19656	1093	210		
NRX-A3	5/20/1965	1072	792		
PHOEBUS-1A	6/25/1965	1090	630		
NRX-A4/EST	March 1966	1055	1740	820	2127
NRX-A5	June 1966	1120	1776		
PHOEBUS-1B	2/23/1967	1450	1800	835	2171
NRX-A6	10/15/1967	1125	3720	847	2282
PHOEBUS-2A	6/25/1968	4082	750	805	2037
PEEWEE-1	Fall 1968	514	2400	845	2266
XE-PRIME	7/1/1969	1140	210	710	2127
NF-1	July 1972	44	6528	830	2277

Table 3.
Timeline of nuclear thermal propulsion tests.

development. Although the program was eventually terminated, its legacy continues to influence the development of new technologies for space exploration.

Table 1 shows key design parameters for the tested nuclear thermal propulsion systems. These reactors were fueled with UC_2 particles with a diameter range of 50–150 μm. The fuel elements were hexagonal in shape, and the propellent was H_2. The matrix material in the fuel elements was graphite.

5.3 Conceptual designs of nuclear thermal propulsion reactors

Many conceptual designs were created during and after the NERVA program. A summary of some of those reactor concepts is provided here [12].

ENABLER (Economical Nuclear Auxiliary Booster Launch Engine for Reentry): this was a conceptual design for a smaller NTP that could be used as an auxiliary engine for space missions. The design was based on a liquid-core concept, which was more compact than the solid-core design used by NERVA-1.

SMALL ENGINE: this was a conceptual design for a compact NTP that would be suitable for use in small spacecraft. The design was based on a liquid-core concept and was intended to be smaller and lighter than NERVA-1 [13].

SNRE (Space Nuclear Rocket Engine): This was a conceptual design for a compact NTP that would be suitable for use in small spacecraft. Like SMALL ENGINE, it was based on a liquid-core design [14].

710: This was a conceptual design for a compact NTP that would be suitable for use in small spacecraft. The design was based on a liquid-core concept and was intended to be smaller and lighter than NERVA-1.

CERMET (Ceramic-Metal) Nuclear Rocket Engine: This was a conceptual design for an NTP that would use ceramic-Metal fuel instead of traditional nuclear fuel. The design was based on a liquid-core concept, and the fuel was intended to provide a higher power density than traditional nuclear fuel.

PBR #1 (Phoebus-1 Reactor): PBR #1 was a conceptual design for a compact NTP that would be suitable for use in small spacecraft. The design was based on a liquid-core concept and was intended to be smaller and lighter than previous NTPs [15].

PBR #2 (Phoebus-2 Reactor): PBR #2 was a conceptual design for an improved version of PBR #1, with a higher power density and improved efficiency.

PeBR (Phoebus-Electron Beam Reactor): PeBR was a conceptual design for an NTP that would use an electron beam instead of a traditional nuclear reactor. The design was based on a liquid-core concept and was intended to be more efficient than traditional NTPs.

LPNTR#1 (Low-Power Nuclear Thermal Rocket): LPNTR#1 was a conceptual design for a compact NTP that would be suitable for use in small spacecraft. The design was based on a liquid-core concept and was intended to be smaller and lighter than previous NTPs [16].

LPNTR#2 (Low-Power Nuclear Thermal Rocket 2): LPNTR#2 was a conceptual design for an improved version of LPNTR#1, with a higher power density and improved efficiency [16].

MARS WIRE CORE: MARS WIRE CORE was a conceptual design for an NTP that would use a wire-wrapped fuel element instead of traditional fuel rods. The design was based on a liquid-core concept and was intended to provide a higher power density than traditional NTPs.

Table 1 shows a comparison of the various conceptual designs for NTPs.

5.4 The particle bed reactor (PBR)

Dr. James Powell was an American scientist and engineer who made significant contributions to the development of nuclear thermal propulsion (NTP) technology. He is well known for his work on the Particle Bed Reactor (PBR), a conceptual design for a compact NTP that would be suitable for use in small spacecraft.

Dr. Powell began his work on NTP technology in the mid-1960s when he was part of a team at the Lewis Research Center (now the John H. Glenn Research Center) in Cleveland, Ohio. His work aimed to develop a compact NTP that would be suitable for use in small spacecraft. The Phoebus-1 Reactor was one of several NTP concepts developed during this period, and it was notable for its small size and high power density.

The PBR design was based on a radial inflow particle bed concept, in which the reactor would heat a working fluid, typically hydrogen, to extremely high temperatures. The hot propellant would then be expelled through a nozzle, producing high-speed exhaust that would generate thrust. The radial inflow geometry allowed the bulk of the system to remain relatively cool, with only the fuel particles and an inner "hot frit" required to operate at a very high temperature. The design was intended to be more compact and lightweight than other NTP concepts, making it well-suited for use in small spacecraft.

Although the PBR was never built or tested, Dr. Powell's work on NTP technology paved the way for further research and development in this field. Today, NTP remains a topic of ongoing research and development, with the goal of developing safe and effective propulsion systems for use in space.

In recognition of his contributions to NTP technology, Dr. Powell was awarded several patents for his work on the PBR and other NTP concepts. He remains an important figure in the history of space propulsion and continues to be remembered for his innovative work on nuclear thermal propulsion.

In 1982, Dr.Powell, while at Brookhaven National Laboratory, presented his work to Grumman representatives, and that got the attention of many people concerning the promise of the PBR and its potential capabilities. In 1987, with $200 million in funding from the strategic defense initiative (SDI) program, a three-phase program was initiated to develop a dramatically higher-performance propulsion engine based on the PBR concept. Phases I and II of the program were to further design and develop the concept and plan comprehensive testing, beginning in Phase III. Unfortunately, the program funding was not continued past 1992. Although zero-power critical experiments were performed, an environmental impact statement (EIS) was completed for a ground test facility, and in-pile fuel testing was completed, the effort did not result in the actual testing of a PBR engine [17, 18].

5.5 Comparison of space chemical and nuclear Propulsion

Space propulsion refers to the technology used to propel spacecraft and other space vehicles. There are two main space propulsion types: chemical and nuclear. Both of these technologies have their advantages and disadvantages, and the choice between them depends on the specific requirements of each mission.

Chemical propulsion is the most widely used technology for space propulsion and has been used for many years to launch and propel spacecraft into orbit. Chemical propulsion works by burning propellant to generate high-speed exhaust, which

provides thrust to the spacecraft. The propellant is stored in tanks onboard the spacecraft and is burned in a controlled manner to produce the required thrust.

One of the main advantages of chemical propulsion is its simplicity and low cost. Chemical propulsion systems are relatively easy to design, build, and operate and can be manufactured using existing technologies and materials. In addition, chemical propulsion systems are widely available and can be easily adapted for use in various spacecraft and missions.

However, chemical propulsion also has several disadvantages. The main disadvantage of chemical propulsion is its low specific impulse, which limits the maximum speed that can be achieved and the total mission time. This makes chemical propulsion less effective for missions requiring high speeds or long durations, such as interplanetary missions. In addition, chemical propulsion systems are limited by the amount of propellant that can be carried on board, which restricts the range and capabilities of the spacecraft.

On the other hand, nuclear propulsion is a more advanced technology that offers several advantages over chemical propulsion. Nuclear propulsion uses nuclear reactors or radioisotope thermoelectric generators (RTGs) to generate heat, producing high-speed exhaust to provide thrust. Nuclear propulsion systems offer a much higher specific impulse than chemical propulsion systems, allowing for higher speeds and longer mission times.

One of the main advantages of nuclear propulsion is its higher energy density, which enables spacecraft to carry more payload and reach higher speeds. This makes nuclear propulsion more suitable for missions requiring high speeds or long durations, such as interplanetary missions. In addition, nuclear propulsion systems are not limited by the amount of propellant that can be carried on board, which eliminates the range restrictions of chemical propulsion systems.

However, nuclear propulsion also has several disadvantages. The main disadvantage of nuclear propulsion is its complexity and high cost. Nuclear propulsion systems are much more challenging to design, build, and operate than chemical propulsion systems, requiring specialized materials and technologies. In addition, the use of nuclear power in spacecraft is subject to strict safety and security regulations, which can add significant cost and complexity to the development and operation of nuclear propulsion systems.

Both chemical propulsion and nuclear propulsion have their advantages and disadvantages, and the choice between them depends on the specific requirements of each mission. Chemical propulsion is a simpler and less expensive technology that is well-suited for missions requiring moderate speeds and short durations. Nuclear propulsion is a more advanced technology that offers higher performance but is more complex and expensive to develop and operate. However, space exploration to Mars and beyond is much more likely with nuclear thermal propulsion, including future fusion reactors [19].

6. Current and near-term nuclear thermal Propulsion programs

Several National Aeronautics and Space Administration (NASA) programs and the United States Department of Energy (DOE) focus on developing PBRs for near-term missions and technology demonstrations. The key technology used in the PBRs is the triso fuel. Triso (tri-structural isotropic) nuclear fuel particles are small, spherical fuel elements used in high-temperature gas-cooled reactors (HTGRs) and PBRs. The fuel

particles consist of a central kernel of fissile material, typically enriched uranium or plutonium, surrounded by several layers of materials that provide structural support and containment for the fissile material.

The outermost layer of the fuel particle is made of a ceramic material that provides containment for the fissile material and acts as a barrier to releasing radioactive gases. The ceramic layer is highly porous, which allows gas to flow through it, and is designed to retain its integrity even under extreme conditions, such as high temperatures and pressures.

The next layer is made of a layer of carbon, which acts as a moderator to slow down fast neutrons and increases the probability of a fission reaction. The carbon layer also provides structural support for the fuel particle and helps to prevent it from disintegrating during high-temperature operation.

The innermost layer of the fuel particle is the fuel coating, which consists of a mixture of fissile material and other materials, such as pyrolytic carbon and silicon carbide, that help to retain the fissile material and prevent it from spreading.

Triso fuel particles are used in PBRs because they provide a highly-efficient and safe means of containing and controlling the fissile material. The fuel particles are designed to withstand high temperatures and pressures and to provide a high degree of containment for the fissile material. Additionally, the fuel particles are small and can be easily packaged, making them well-suited for compact PBRs.

NASA, the US DOE, and the Defense Advanced Research Projects Agency (DARPA) are supporting research and development programs to develop, test, and demonstrate the feasibility of the triso fuel and the PBR concept. General Atomics, BWX Technologies, Inc. (BWXT), and Ultra Safe Nuclear are some companies currently developing the PBR concept, with technology demonstrations planned for the 2025–2027 timeframe.

BWXT's TRISO fuel is a type of fuel used in high-temperature gas-cooled nuclear reactors. TRISO stands for "Tri-Isotropic" and refers to the unique microstructure of the fuel particles. The fuel particles are coated with multiple layers of carbon and ceramic materials, which helps to retain the fissile material even in the event of a loss of coolant accident. This makes TRISO fuel ideal for use in advanced reactors, such as high-temperature gas-cooled reactors, requiring fuel that can withstand high temperatures and high radiation levels. TRISO fuel is manufactured through a complex process that involves forming, coating, and sintering the fuel particles. The result is a highly durable fuel that offers superior performance and improved safety compared to traditional nuclear fuel.

6.1 The centrifugal nuclear thermal rocket (CNTR)

Liquid-fuel nuclear rocket engines have been envisioned since at least 1954, and various liquid-fuel NTP design concepts were proposed in the 1960s. Liquid fuel nuclear rocket engine concepts described to date employ one of three basic design approaches: (1) the bubble-through reactor, (2) the radiation reactor, and (3) the particle or droplet reactor. These reactor concepts are illustrated in **Figures 1–3**, respectively. The bubble-through reactor design features a reactor fuel that is rotated at high speed to maintain a layer of liquid fuel annulus around the inner cylindrical surface of the fuel. As the hydrogen propellant is bubbled through this liquid fuel, it is heated to the temperature of the liquid fuel. The hot hydrogen then exits the engine through the nozzle to produce a thrust. The radiation reactor design features a rotating cylinder to maintain the liquid fuel but flows hydrogen axially down the center of
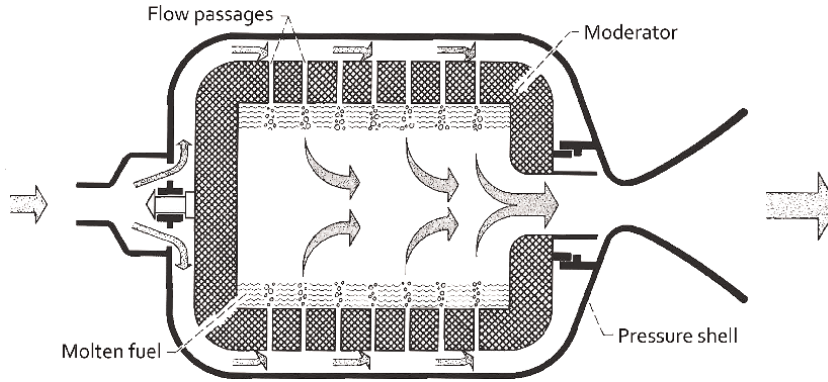
Figure 1.
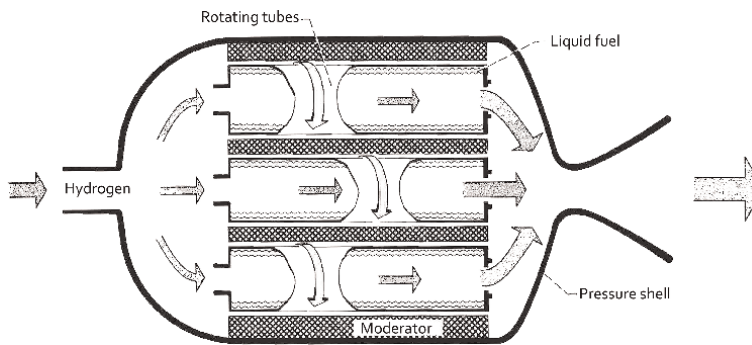*Bubble-through liquid fuel reactor [20].*

Figure 2.
Radiation liquid fuel reactor [20].

rotating tubes where it is heated by radiation and surface convection from the liquid. In the particle or droplet reactor design, fuel particles or liquid droplets are continuously recirculated through the propellant stream in the activity zone of the reactor [21].

Although the radiation reactor engine concept is the simplest, it suffers from the fact that the greatest heat generation occurs at the outer boundary of the liquid uranium, which is the inner wall of the rotating cylinder, and containment materials are not yet known which maintain needed structural characteristics when operating at these temperatures. For the droplet reactor, the neutronics modeling is intractable with the current neutronics modeling tools and techniques. Hence research efforts presently focus on the bubble-through concept due to more tractable thermodynamics and neutronics.

A liquid fuel reactor concept presently under study by a NASA-sponsored university team employs a bubble-through reactor design while utilizing multiple elongated Centrifugal Fuel Elements (CFEs). A nineteen CFE engine configuration is illustrated in **Figures 4** and **5**. Like solid fuel NTP systems, propellant from the propellant tank (not shown) passes through the neutron reflector, a regeneratively cooled section of the nozzle, neutron moderator, and structure before entering the fueled region. This propellant flow configuration assures that all moderators and structural materials
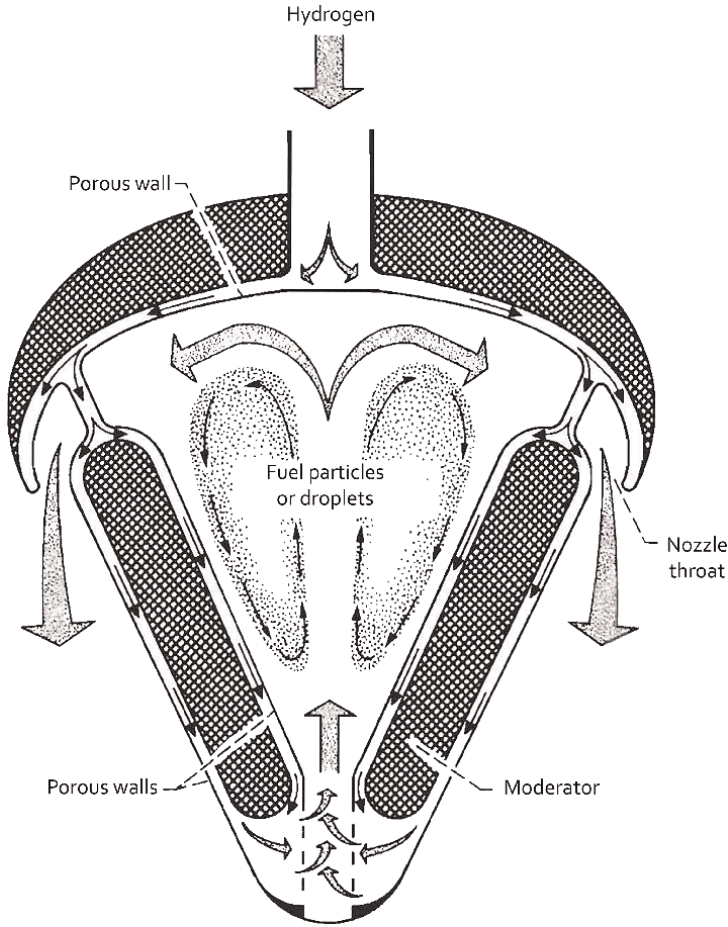
Figure 3.
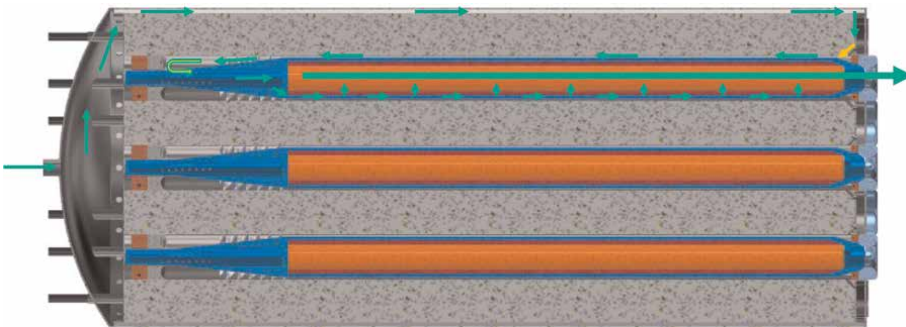*Particle or droplet liquid fuel reactor [20].*

Figure 4.
Propellant flow path in the CNTR (not to scale) [5, 6].

within the engine remain at a relatively low temperature (< 800 K). In **Figure 4**, the propellant enters through the porous rotating cylinder wall at $\sim$800 K, passes radially through the molten uranium fuel annulus, and exits axially through the bore into a
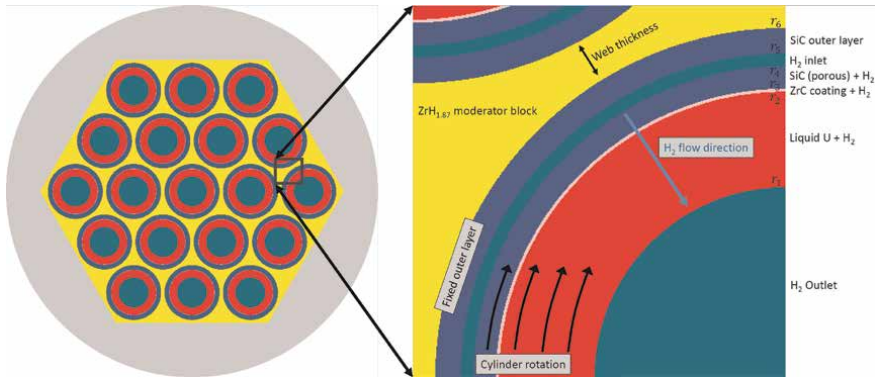
Figure 5.
*Full-core slice of the engine shown in **Figure 4** at the axial midplane (top) and a close-up of a single CFE (bottom) [5, 6].*

common plenum before being accelerated through a converging/diverging nozzle. Liquid uranium near the inner cylinder wall of each CFE is maintained at ∼1500 K by the inflowing propellant. The uranium temperature near the center of the rotating cylinder could reach 5500 K but only contacts the propellant and does not contact any structural material. The system operates at high pressure (>3.5 MPa) to avoid bulk boiling of the uranium metal.

While modeling and analysis efforts as of this writing continue to support the viability of this concept, several engineering challenges must be addressed before the engineering feasibility of this concept can be established. These challenges include:

1. Adequate heat transfer between the metallic liquid uranium and the propellant must be demonstrated.

2. A porous rotating cylinder wall must be developed that allows propellant to flow into the Centrifugal Fuel Element (CFE) while not allowing molten uranium to be forced out (by the centrifugal force) through the propellant flow passages. The porous wall needs to help ensure adequate mixing between the propellant and uranium by finely distributing the inflowing propellant and by distributing the propellant flow to match the axial power profile within the rotating cylinder.

3. A coating must be developed for the inside of the rotating cylinder wall that is compatible with liquid uranium and all potential propellants at ∼1500 K.

4. The rotating cylinder itself must be designed and fabricated, with transpiration and film cooling as needed to avoid potential hot spots.

5. Reliable methods for rotating the cylinders at several thousand RPM must be developed, and methods for accommodating the failure of individual cylinders must be devised.

6. Methods for accommodating transients, including startup and shutdown, must be devised to minimize the loss of uranium fuel and avoid vibrational instabilities.

7. The reactor and cylinder exit must be designed to ensure that the uranium loss rate from the system is acceptable, with a High Assay Low Enriched Uranium (HALEU) loss goal of <0.01% of the propellant mass.

8. Methods for controlling reactivity as needed for startup/shutdown and due to burnup or entrainment of Uranium in the propellant must be designed.

9. The neutronic design of the fuel must be optimized. Experience from previous (lower temperature) liquid reactor development programs should be used to ensure stable operation during startup, operation, and shutdown.

10. Methods for incorporating the CNTR reactor into an NTP engine must be devised. The CNTR uses a moderator block approach. Methods used for incorporating traditional NTP reactors into an NTP engine with a moderator block may be directly applicable.

This list of engineering challenges is daunting and reveals why a liquid-fuel nuclear thermal rocket engine has not yet been developed or prototyped. But the challenges all derive from the high temperatures, which yield the high-performance potential – 1800 s specific impulse with a thrust-to-weight ratio comparable to solid fuel NTP engines [22, 23].

Currently, scientific missions to the outer planets of the Solar System require planetary flyby trajectories so that velocity is gained from the respective planets along the way to the destination. Such trajectories result in infrequent and narrow launch windows and transit times from Earth to the destination planet that is typically double that of a direct trajectory. Unfortunately, chemical propulsion systems lack the performance needed to enable direct trajectories to the Solar System outer planets.

Mission analyses have shown that solid fuel NTP enables direct trajectory rendezvous missions to Jupiter and Saturn, with launch windows occurring approximately annually and using commercial heavy-lift rockets. Preliminary results of similar mission analyses have shown that liquid fuel NTP enables direct trajectories as far as selected Kuiper Belt objects, including Pluto and Quaoar. In addition to opening up the Solar System to scientific exploration, liquid fuel NTP can significantly reduce travel times for human exploration of the Solar System since using trajectories other than minimum energy trajectories becomes feasible for many planetary destinations. It is this potential that warrants research into liquid fuel NTP [24].

6.2 Nuclear fusion propulsion

Nuclear fusion is a promising technology for space propulsion that has been under investigation for several decades. The idea is to harness the energy released during the fusion of atomic nuclei to propel spacecraft through space. The fusion process involves merging two or more atomic nuclei to form a heavier nucleus and release a large amount of energy. This energy is produced as a result of the strong nuclear force that holds the protons and neutrons in the nucleus together. The energy released by fusion reactions is much greater than that of chemical reactions, making it a potential source of clean, safe, and sustainable energy for space exploration.

The key challenge in developing nuclear fusion for space propulsion is to achieve sustained, controlled fusion reactions. The high temperatures and pressures required

to initiate and maintain fusion reactions are difficult to achieve and maintain in a controlled manner. In addition, the fuel used in fusion reactions, typically hydrogen isotopes such as deuterium and tritium, must be heated to tens of millions of degrees Celsius to achieve the conditions required for fusion. Also, 80% of the energy released in a standard deuterium-tritium fusion reaction is in the neutron that is produced, and if that neutron is, in turn, used to produce tritium (replacing the tritium that is consumed), then the neutron's energy is essentially converted into heat which severely limits performance. A neutronic fusion (such as p-11B) appears to have much greater performance potential. Still, it is much more difficult to achieve high "Q" (energy out/energy in) values than D-T.

Several approaches are being explored to achieve controlled nuclear fusion for space propulsion, including magnetic confinement, inertial confinement, and laser-based fusion. Magnetic confinement fusion involves confining the plasma in a magnetic field, while inertial confinement fusion involves rapidly compressing the fuel to initiate fusion. Laser-based fusion involves using laser beams to heat and compresses the fuel.

Magnetic confinement fusion is the most mature of the fusion technologies. It has been the focus of several large-scale fusion experiments, including the International Thermonuclear Experimental Reactor (ITER) being built in France. ITER aims to demonstrate the feasibility of commercial fusion power and develop the technologies required for fusion-based space propulsion.

Inertial confinement fusion is a newer approach that has the potential to achieve fusion in a much smaller and simpler device than magnetic confinement fusion. However, it is still in the early stages of development and has yet to demonstrate sustained fusion reactions.

Laser-based fusion is another promising approach that has shown great promise in recent years. The technology involves high-powered laser beams to heat and compresses the fuel to achieve fusion conditions. Laser-based fusion has the potential to achieve fusion in a smaller and simpler device than either magnetic confinement or inertial confinement fusion. It has the added advantage of responding quickly to changes in power demand, making it well-suited for use in space propulsion systems.

Despite the promise of nuclear fusion for space propulsion, many technical challenges must be overcome. The tritium fuel used in fusion reactions must be carefully managed to ensure that it does not pose a threat to the environment or human health. In addition, the high temperatures and pressures required for fusion reactions must be carefully controlled to ensure the safety of the spacecraft and its crew.

Despite these challenges, the potential benefits of nuclear fusion for space propulsion make it an area of intense research and development. The technology has the potential to revolutionize space exploration by providing a clean, safe, and sustainable source of energy for spacecraft propulsion. This could enable missions to be conducted more efficiently and with greater payloads, opening up new frontiers in space exploration and enabling humanity to expand its presence in the universe.

Nuclear fusion has the potential to be a game-changer for space propulsion. The technology offers the promise of clean, safe, and sustainable energy for spacecraft propulsion, which could enable a new era of space exploration. With continued investment and innovation, nuclear fusion may become the power source of the future.

6.3 Matter-antimatter nuclear propulsion

Antimatter propulsion using positron-electron or proton-antiproton annihilation is a theoretical form of propulsion that has the potential to revolutionize the way we explore the universe. In this form of propulsion, energy is produced by the annihilation of matter and antimatter, specifically positrons and electrons or protons and antiprotons. This energy can then be harnessed to propel a spacecraft to extremely high speeds, making it possible to explore the universe much faster than with current propulsion methods.

The concept of antimatter propulsion is based on the principle of matter-antimatter annihilation. When a particle of matter and its corresponding antiparticle collide, they annihilate each other, releasing a large amount of energy in the form of gamma rays. The idea is to somehow harness that energy in a way that produces a powerful, highly efficient propulsion system for space applications.

One of the key advantages of antimatter propulsion using positron-electron or proton-antiproton annihilation is its potential for extremely high energy output. If the reaction products can be efficiently directed, then that energy could propel a spacecraft to extremely high speeds, approaching 10% of the speed of light, making it possible to reach the nearest star in just a few decades. This is a significant improvement over current propulsion methods, which would take thousands of years to reach the same destination.

In addition to its high energy output, antimatter propulsion using positron-electron or proton-antiproton annihilation is also highly efficient. Unlike traditional propulsion methods that rely on chemical reactions to produce energy, this form of propulsion uses the energy produced by matter-antimatter annihilation to propel the spacecraft. This means that a much smaller amount of fuel is required to achieve the same level of performance as traditional propulsion methods, assuming the reaction products can be directly used as a propellant without creating significant waste heat.

However, despite its many advantages, several challenges are associated with developing antimatter propulsion using positron-electron or proton-antiproton annihilation. One of the biggest challenges is the production of large quantities of antimatter. Currently, scientists can only produce tiny amounts of antimatter in particle accelerators, making it difficult to develop a practical and scalable propulsion system.

Another challenge is the containment of the antimatter. Antimatter is highly reactive and dangerous and must be kept away from normal matter to prevent accidental annihilation. This requires the development of highly specialized and advanced electromagnetic containment systems, which must withstand the intense energy produced by annihilating matter and antimatter.

Another challenge is directing the matter/antimatter reaction products in a way that efficiently produces thrust without producing a significant amount of waste heat.

Finally, there is also the issue of cost. Antimatter production is extremely expensive, and the cost of developing an antimatter propulsion system using matter-antimatter annihilation would likely be prohibitively high. The cost is a significant barrier to developing this technology for space applications.

7. Conclusions

Nuclear thermal propulsion is a promising technology that has the potential to revolutionize space travel and make interplanetary missions more feasible and

efficient. Unlike conventional chemical rocket propulsion systems, nuclear thermal propulsion systems use the heat generated by a nuclear reactor to heat a propellant, allowing for much higher specific impulses and faster interplanetary travel times.

The benefits of nuclear thermal propulsion for space travel are numerous and far-reaching. One of the most significant advantages is its much higher specific impulse, which allows for much higher exhaust velocities and, thus, a much greater change in velocity (Δv). This means that spacecraft equipped with nuclear thermal propulsion systems can reach their destinations much faster than those equipped with conventional chemical rocket propulsion systems.

Another advantage of nuclear thermal propulsion for space travel is its increased payload capacity. Since nuclear thermal propulsion systems have a much higher specific impulse, they require less propellant to achieve the same Δv, allowing for increased payload capacities and more extensive missions.

Nuclear thermal propulsion also offers better reliability and safety than conventional chemical rocket propulsion systems. Nuclear thermal propulsion systems are less susceptible to the problems associated with chemical reactions, such as explosions or leaks, and they can operate for extended periods without refueling.

In conclusion, nuclear thermal propulsion is a game changer for space travel, offering improved performance, increased payload capacities, and improved reliability and safety compared to conventional chemical rocket propulsion systems. While significant technical and regulatory challenges must be overcome, the potential benefits of nuclear thermal propulsion make it a promising technology for the future of space travel.

Acknowledgements

Author details

Bahram Nassersharif[1*] and Dale Thomas[2]

1 University of Rhode Island, Kingston, Rhode Island, USA

2 University of Alabama at Huntsville, Huntsville, Alabama, USA

*Address all correspondence to: nassersharif@uri.edu

IntechOpen

References

[1] Duncan F. Rickover and the Nuclear Navy: The Discipline of Technology. Annapolis, MD: Naval Institute Press; 1990. 374 p

[2] Rom FE. Analysis of a Nuclear-Powered Ram-Jet Missile (PDF) (Report). National Advisory Committee for Aeronautics. NACA-RM-E54E07. 1954

[3] Ragheb M. Nuclear RAMJET and SCRAMJET propulsion. [Internet] Available from: https://mragheb.com/NPRE%20402%20ME%20405%20Nuclear%20Power%20Engineering/Nuclear%20Ramjet%20and%20Scramjet%20Propulsion.pdf

[4] Trakimavičius ML. The Future Role of Nuclear Propulsion in the Military. NATO Energy Security Report, 2021

[5] Thomas D, Houts M, Walters W, Hollingsworth K, Frederick R, Cassibry J. Toward the engineering feasibility of the centrifugal nuclear thermal rocket. Journal of the British Interplanetary Society. 2022;**75**(5):181-188

[6] Thomas D, Houts M, Walters W, Hollingsworth K, Frederick R, Cassibry J. Early progress toward the feasibility of the centrifugal nuclear thermal rocket. In: 73rd International Astronautical Congress. Paris; 2022

[7] Bhattacharyya SK. An assessment of fuels for nuclear thermal propulsion. [Internet]. 2002. ANL/TD/TM01-22, 822135. Report No.: ANL/TD/TM01-22, 822135. Available from: http://www.osti.gov/servlets/purl/822135/

[8] Lyon LL. Performance of (U,Zr)C-graphite (composite) and of (U,Zr)C (carbide) fuel elements in the Nuclear Furnace 1 test reactor [Internet]. 1973. LA–5398-MS, 4419566. Report No.: LA–5398-MS, 4419566. Available from: http://www.osti.gov/servlets/purl/4419566-nTBR5S/

[9] Cuppari MGDV, Santos SF. Physical properties of the NbC carbide. Metals. 2016;**6**(10):250

[10] Finseth JL. Rover Nuclear Rocket Engine Program: Overview of Rover Engine Tests. Huntsville, AL (United States): Sverdrup Technology, Inc; 1991 Available from: https://www.osti.gov/biblio/5857913

[11] Burns D, Johnson S. Nuclear thermal propulsion reactor materials. In: Tsvetkov P, editor. Nuclear Materials. London, UK: IntechOpen; 2021. Available from: https://www.intechopen.com/books/nuclear-materials/nuclear-thermal-propulsion-reactor-materials

[12] Nuclear Rockets [Internet]. Glenn Research Center | NASA. 2023. Available from: https://www1.grc.nasa.gov/historic-facilities/rockets-systems-area/7911-2/

[13] Schnitzler B, Borowski S, Fittje J. A 25,000-lbf thrust engine options based on the small nuclear rocket engine design. In: 45th AIAA/ASME/SAE/ASEE Joint Propulsion Conference & Exhibit. Denver, Colorado: American Institute of Aeronautics and Astronautics; 2009. Available from: http://arc.aiaa.org/doi/abs/10.2514/6.2009-5239

[14] Borowski SK, DR MC, Burke LM. The Nuclear Thermal Propulsion Stage (NTPS): A Key Space Asset for Human Exploration and Commercial Missions to the Moon. In: AIAA SPACE 2013 Conference and Exposition. San Diego, CA: American Institute of Aeronautics

and Astronautics; 2013. Available from: https://arc.aiaa.org/doi/10.2514/6.2013-5465

[15] Ludewig H, Powell JR, Todosow M, Maise G, Barletta R, Schweitzer DG. Design of particle bed reactors for the space nuclear thermal propulsion program. Progress in Nuclear Energy. 1996;**30**(1):1-65

[16] Madsen W, Neuman J, Ramsthaler J, Schnitzler B. A preliminary stage configuration for a low pressure nuclear thermalrocket (LPNTR). In: Space Programs and Technologies Conference. Huntsville, AL, USA: American Institute of Aeronautics and Astronautics; 1990. Available from: https://arc.aiaa.org/doi/10.2514/6.1990-3791

[17] Space Nuclear Thermal Propulsion Program. 2023. Available from: https://apps.dtic.mil/sti/citations/ADA305996

[18] Space Nuclear Propulsion Technologies Committee, Aeronautics and Space Engineering Board, Division on Engineering and Physical Sciences, National Academies of Sciences, Engineering, and Medicine. Space Nuclear Propulsion for Human Mars Exploration. Washington, DC: National Academies Press; 2021. Available from: https://www.nap.edu/catalog/25977

[19] Cooper RS. Nuclear Propulsion for space vehicles. Annual Review of Nuclear Science. 1968;**18**(1):203-228

[20] Rom FE. Nuclear-Rocket Propulsion. Cleveland, Ohio: Lewis Research Center; 1968. p. 41

[21] Kumar S, Thomas D, Cassibry J. Nuclear thermal propulsion for Jupiter and Saturn Rendezvous Missions. AIAA Journal of Spacecraft and Rockets. 2022; **2022**

[22] McCarthy JJ. Nuclear Reactors for Rockets. AIAA; 1954

[23] Nelson ST, Grey J, Williams PM. Conceptual study of a liquid-Core nuclear rocket. AIAA Journal of Spacecraft and Rockets. 1965;**2**(3):384-391

[24] Ziehm W, Thomas D. Mission Design Analysis with Centrifugal Nuclear Thermal PROPULSION. National Harbor, Maryland: AIAA SciTech; 2023

Edited by Longbiao Li

Propulsion systems play an important role in civil and military applications. New designs, new materials, and new technologies have already been applied to propulsion systems to improve power and decrease energy consumption. This book focuses on the recent progress in propulsion system development for different applications in fields such as aerospace and marine industries, as well as for high-speed trains and other vehicles.

IntechOpen